Università degli Studi di Genova
Sedi Consorziate di Torino e Modena

DOTTORATO DI RICERCA IN GEOFISICA
XIV Ciclo

Tesi di Dottorato

Vortex Dynamics and Particle Transport in Barotropic Turbulence

Relatore:
Prof. Arnaldo Longhetto
Dipartimento di Fisica Generale
Università degli Studi di Torino

Co-Relatore:
Dott. Antonello Provenzale
Istituto di Cosmo-geofisica del CNR
Torino

Candidato:
Luca Montabone

Contents

Abstract - Sommario

This Ph.D. thesis discusses vortex dynamics and particle transport by coherent vortices in homogeneous, rapidly rotating, turbulent fluids. The approach is both experimental and numerical. Applications to geophysical fluid dynamics are related to the study of large-scale motions in the atmosphere and the oceans, where coherent vortices are an important component of the dynamics. After a brief discussion of the properties of barotropic turbulence and its relevance to geophysics, I consider vortex dynamics in large-scale laboratory experiments. These are aimed at studying the emergence and development of coherent vortices in a shallow layer of homogeneous fluid in free decay, initially forced in order to create unstructured turbulence. The Lagrangian aspects of these experiments are also pointed out, and the transport of passive tracers in such a turbulent field with fully developed coherent vortices is described. Tracer dynamics is studied by using both experimental evidence and a mixed, experimental-numerical technique which allows to obtain trajectories of individual tracers. The problem of the dynamics of real particles embedded in a fluid (*impurities*) is finally considered; ideal fluid particles are point-like and massless, but real particles have finite size and their density may differ from the density of the surrounding fluid. The dynamics of impurities is then discussed by means of numerical simulations, both in simple stationary flows characterized by the presence of vortex structures, and in barotropic turbulence with fully-developed coherent vortices. Special attention is given to neutrally-buoyant tracers, whose finite size may change the dynamical behaviour with respect to fluid particles, in flows where vortices are an important component.

Questa tesi di dottorato tratta della dinamica di vortici e del trasporto di particelle da parte di vortici coerenti in fluidi turbolenti, omogenei e rapidamente rotanti. L'approccio è sia di tipo sperimentale che di tipo numerico, e le applicazioni alla fluidodinamica geofisica sono in relazione allo studio dei moti a grande scala nell'atmosfera e negli oceani, dove i vortici coerenti costituiscono un'importante componente della dinamica. Dopo una breve discussione sulle proprietà della turbolenza barotropica e sulla sua rilevanza in geofisica, mi occupo della dinamica di vortici in esperimenti di laboratorio a grande scala, finalizzati allo studio della nascita e sviluppo di vortici coerenti in uno strato sottile di fluido omogeneo in decadimento libero, inizialmente forzato in maniera tale da creare una turbolenza

non strutturata. Vengono anche illustrati gli aspetti Lagrangiani di tali esperimenti e viene descritto il trasporto di traccianti passivi in un tale campo turbolento caratterizzato da vortici coerenti pienamente sviluppati, sia mediante risultati derivati dagli esperimenti, sia mediante l'utilizzo di una tecnica mista sperimentale-numerica, che permette di ottenere le traiettorie di traccianti individuali. Viene infine preso in considerazione il problema della dinamica di particelle reali immerse in un fluido (*impurità*); le particelle di fluido ideali sono puntiformi e non hanno massa, ma le particelle reali hanno una dimensione finita e la loro densità può essere diversa da quella del fluido che le circonda. Viene dunque discussa la dinamica delle impurità per mezzo di simulazioni numeriche effettuate sia in semplici flussi stazionari caratterizzati dalla presenza di strutture vorticose, sia in turbolenza barotropica con vortici coerenti pienamente sviluppati. Speciale attenzione viene posta al caso dei traccianti con la stessa densità del fluido, le cui dimensioni finite possono modificare il comportamento dinamico rispetto alle particelle di fluido, in flussi in cui i vortici sono una componente importante.

Introduction

September 5th, 1996: hurricane ”Fran” slams into North Carolina’s southern coast in USA, with sustained winds of approximately 190 *km/h* and gusts as high as 200 *km/h*. Flooding is a severe problem in the whole area hit by the hurricane (see figure 1), which produces rainfall amounts of over 250 millimiters in parts of eastern North Carolina and western Virginia. This hurricane, as the ones that almost every year hit United States and Caribbean area, originated as a tropical cyclone over the Atlantic Ocean and moved towards the mainland, where it finally released all its large amount of energy and destructive power.

Such a phenomenon is an example of a coherent vortex structure in nature, where the attribute ”coherent” points at the long lifetime and the well-definite shape

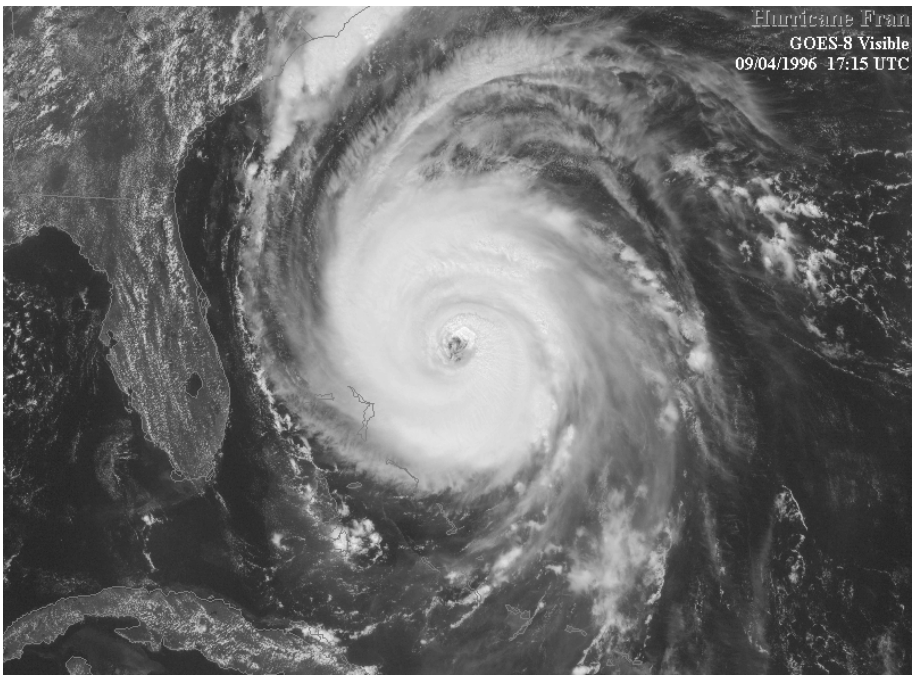

Figure 1: Hurrican ”Fran” viewed by a satellite image. It is possible to recognize the coast of Florida (USA). Photo downloaded from the web site of the *National Climatic Data Center* (NCDC).

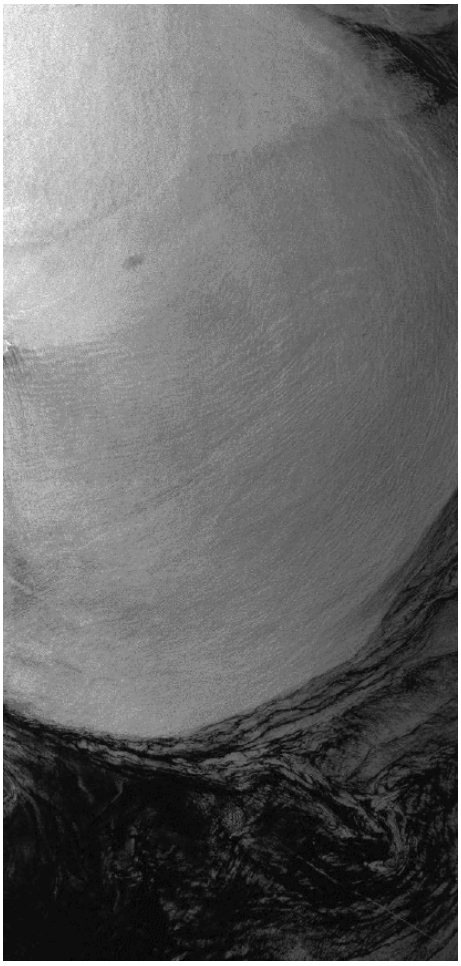

Figure 2: The bright area in the image (taken by the satellite ERS by means of SAR technique) is caused by an anticyclonic warm eddy in the Gulf of Tehuantepec, which is located at the Pacific coast of Mexico. Photograph downloaded from the web site of the *Institute of Oceanography* in Hamburg.

of the vortex. Geophysical flows are characterized by the presence of strong vortical structures, which have fundamental importance for the overall transport of heat, salt, moisture and particles both in oceans (see figure 2) and in atmospheres (not only in Earth's atmosphere, but also in the atmospheres of outer planets of Solar System: figure 3 shows the well-known Jupiter's Great Red Spot).

For these reasons, Geophysical Fluid Dynamics includes the study of vortex dynamics and the associated transport properties as key issues for the understanding of the dynamics of the oceans and the atmosphere, with the final purpose of predicting, for instance, extreme events such as the one described above.

The last two decades have seen a large production of papers devoted to the study of some approximations of the Navier-Stokes equations for Fluid Dynamics, such as the barotropic quasi-geostrophic or the two-dimensional approximations;

Figure 3: This Voyager 2 image shows the region of Jupiter extending from the equator to the southern polar latitudes in the neighborhood of the Great Red Spot. Photo downloaded from the web site of NASA.

this strong interest has been motivated by the fact that such approximations show much of the phenomenology of the nonlinear dynamics that can be observed in large-scale geophysical flows when rotation dominates.

One of these phenomena that are captured, for instance, by the two-dimensional approximation of the Navier-Stokes equations is the development of coherent vortices emerging from a turbulent, unstructured background. These flow structures are shown to carry most of the energy of the turbulent system and to dominate the dynamics of the flow at late times.

Coherent vortices show also peculiar characteristics with respect to the transport of passive tracers in a turbulent field: numerical simulations show that vortices are able to trap tracers for long times, much longer than the typical rotation time scale inside the vortex (*eddy turnover time*), and are generally impermeable to inward fluxes of particles. They are also areas of the flow where fluid particle motion is regular, rather than chaotic as in unstructured turbulence.

These properties are strictly valid when considering point-like and massless

fluid elements, more than particles with finite size and/or finite inertia with respect to the fluid. In this latter case, the dynamical behaviour can be significantly changed.

This Ph.D thesis adds a further piece to the puzzle of understanding vortex dynamics and transport of particles by coherent vortices in turbulent flows relevant for Geophysical Fluid Dynamics. The approaches I have followed to this purpose are both experimental and numerical: laboratory experiments on quasi two-dimensional, large-scale turbulent flows and numerical simulations on the dynamics of finite-size particles with inertia ("impurities") are the main topics included in this thesis, whose organization is the following:

- **Chapter 1**: in this chapter, the theory of barotropic turbulence is briefly summarized. The governing equations of some approximations of the Navier-Stokes equations are discussed, and the process of emergence and development of coherent vortices is described.

- **Chapter 2**: large-scale laboratory experiments on the dynamics of long-lived coherent vortices in rapidly rotating, barotropic flows in free decay are presented and discussed.

- **Chapter 3**: A laboratory view on transport of passive tracers by coherent vortices is the topic of this chapter: trapping of tracers and regular motions inside vortex cores, impermeability of vortices to inward fluxes of particles and merging of two vortices from the Lagrangian point of view are the phenomena considered.

- **Chapter 4**: this chapter is devoted to introduce the equation of motion for finite-size particles with inertia ("impurities"), whose dynamics can be very different from the dynamics of fluid elements ("Lagrangian particles").

- **Chapter 5**: the dynamics of impurities in simple, stationary, analytical vortical flow models is the subject of this chapter.

- **Chapter 6**: the dynamics of impurities in barotropic two-dimensional turbulence will be discussed, by using the results obtained in the analytical vortical flow models.

- **Chapter 7**: the special case of the dynamics of tracers with finite-size and the same density as the surrounding fluid is considered and bias ses with respect to Lagrangian particles statistics are pointed out.

Chapter 1

Barotropic turbulence

In this chapter, the theory of barotropic turbulence is briefly summarized, for the case of an homogeneous and incompressible Newtonian fluid. This fundamental hypothesis is assumed throughout this thesis. The governing equations of barotropic quasi-geostrophic turbulence and two-dimensional turbulence are discussed and the process of emergence and development of coherent vortices is described, from both a numerical and an experimental viewpoint. Applications to geophysical fluid dynamics are also mentioned.

1.1 Basic concepts of fluid dynamics

The starting point in the study of fluid dynamics is provided by the *continuum assumption*, which allows to use continuity and derivability for the variables by which a fluid is described: density, pressure, velocity, temperature, etc. Two approaches are possible to describe such a fluid; in the *Eulerian* approach, a generic variable F depends on time and on the position vector $\mathbf{r} = (x, y, z)$, thus in every point of space, a value $F = F(\mathbf{r}, t)$ may be associated at a certain time t. In the *Lagrangian* description of the fluid, the generic variable F is associated with the motion of every fluid element, thus it depends on time and on the position of the fluid element at the initial time: $F = F(\mathbf{r}_0, t)$; in particular, the vector $\mathbf{r} = \mathbf{r}(\mathbf{r}_0, t)$ describes the trajectory of a fluid element. The link between the two approaches can be found in the definition of the total time derivative of a generic Eulerian variable F of the fluid, given by the *material derivative* following the motion of a fluid element:

$$\frac{DF}{Dt} = \frac{\partial F}{\partial t} + (\mathbf{u} \cdot \nabla) F, \tag{1.1}$$

where $\mathbf{u}(\mathbf{r}, t) = (u, v, w)$ is the velocity vector and ∇ is the gradient operator. The material derivative performs the task of representing an essentially Lagrangian concept, in an Eulerian language.

By using such an Eulerian approach, the dynamics of an homogeneous, incompressible, Newtonian fluid moving in a steadily rotating reference frame can be described. Such a flow is governed by the Navier-Stokes equation, describing the balance of momentum, and by the continuity equation, which represents the conservation of mass:

$$\frac{D\mathbf{u}}{Dt} + 2\boldsymbol{\Omega} \times \mathbf{u} + \boldsymbol{\Omega} \times (\boldsymbol{\Omega} \times \mathbf{r}) = -\frac{1}{\rho}\nabla p + \nabla \phi_g + \nu \nabla^2 \mathbf{u}, \tag{1.2}$$

$$\nabla \cdot \mathbf{u} = 0, \tag{1.3}$$

where D/Dt is the material derivative, $\mathbf{u}(\mathbf{r}, t)$ is the velocity vector relative to the rotating system, $\mathbf{r}$ is the position vector, $\boldsymbol{\Omega}$ is the angular velocity of the rotating reference frame, p is the pressure, ϕ_g is the gravitational potential, ρ is the constant fluid density, ν is the constant kinematic viscosity and ∇^2 is the laplacian operator. See, for example, Kundu (1990) for a derivation of these equations.

In the l.h.s. of equation (1.2), the first term represents the fluid acceleration in the rotating system, the second term is the Coriolis acceleration and the third term is the centripetal acceleration, which can be written as the gradient of a centrifugal potential, $-\nabla\phi_c = -\nabla\left(|\boldsymbol{\Omega} \times \mathbf{r}|^2/2\right)$, and combined with the term $\nabla\phi$ in the r.h.s., by defining a total potential $\Phi = \phi_g + \phi_c$. The first term in the r.h.s. of the Navier-Stokes equation represents the pressure gradient-force (per unit mass), the second term is the conservative gravitational force and the last term is the non-conservative viscous force for Newtonian, incompressible fluids (for which the continuity equation (1.3) is valid).

The *relative vorticity* vector is defined as $\boldsymbol{\omega} = \nabla \times \mathbf{u}$. By taking the curl of equation (1.2) and using adequate vector identities, the relative vorticity equation reads (see Pedlosky 1987 for a complete derivation):

$$\frac{D\boldsymbol{\omega}}{Dt} = \left[(2\boldsymbol{\Omega} + \boldsymbol{\omega}) \cdot \nabla\right] \mathbf{u} + \nu \nabla^2 \boldsymbol{\omega}, \tag{1.4}$$

where $(2\boldsymbol{\Omega} + \boldsymbol{\omega})$ is usually defined as the *absolute vorticity* vector and the baroclinic vector, *i.e.* $\dfrac{\nabla\rho \times \nabla\left(p - \rho\Phi\right)}{\rho^2}$, vanishes for constant ρ; the fluid in this case is referred to as *barotropic*.

By using a length scale L and a velocity scale U which characterize the flow, nondimensional variables can be introduced, denoted by primes:

$$\begin{aligned} \mathbf{r}' &= \mathbf{r}/L, \\ \mathbf{u}' &= \mathbf{u}/U, \\ t' &= t\left(U/L\right). \end{aligned} \tag{1.5}$$

Equations (1.2) and (1.4) can then be adimentionalized, by setting $\boldsymbol{\Omega} = \Omega\mathbf{k}$ where $\mathbf{k}$ is the unit vector along the axis of rotation. The relative acceleration term in equation (1.2) can be estimated as $D\mathbf{u}/Dt = O\left(U^2/L\right)$, the Coriolis acceleration as $2\Omega\mathbf{k} \times \mathbf{u} = O\left(2\Omega U\right)$ and the frictional force (per unit mass) as $\nu\nabla^2\mathbf{u} = O\left(\nu U/L^2\right)$. The ratio of the relative to the Coriolis acceleration in equation (1.2) is referred to as the *Rossby number*:

$$Ro = \frac{U}{2\Omega L}. \tag{1.6}$$

In the same way, the ratio of the relative acceleration to the frictional force per unit mass is the *Reynolds number*, and the ratio of the frictional force per unit mass to the Coriolis acceleration is referred to as the *Ekman number*:

$$Re = \frac{UL}{\nu}, \tag{1.7}$$

$$Ek = \frac{\nu}{2\Omega L^2}. \tag{1.8}$$

Strong rotating flows or large scale flows have small Rossby and Ekman numbers ($\ll 1$); turbulent flows have, in general, large Reynolds numbers ($Re \gg 1000$).

In geophysical fluid dynamics, particular importance is given to the concept of *potential vorticity*, which satisfies a conservation law, under certain constraints. If one considers a scalar fluid property λ, which satisfies an equation of the form $D\lambda/Dt = \Psi$, where Ψ is a source term of λ, from equation (1.4) one can derive that the potential vorticity

$$\Pi = \frac{2\boldsymbol{\Omega} + \boldsymbol{\omega}}{\rho} \cdot \nabla\lambda \tag{1.9}$$

is a material invariant, *i.e.*

$$\frac{D\Pi}{Dt} = 0, \tag{1.10}$$

if the following constraints are valid:

- $\Psi = 0$, namely λ is a material invariant;
- the viscous force is negligible, namely $\nu \cong 0$ or $Re \gg 1$;
- either the fluid is barotropic or λ depends only on p and ρ.

This is the *Ertel theorem*, whose demonstration can be found in Pedlosky (1987).

Another important theorem of basic fluid dynamics, which I will use widely in the following, is the *Taylor-Proudman theorem*, which is valid for barotropic, inviscid and fast rotating flows, namely for homogeneous flows with small Ekman and Rossby numbers. Under these hypothesis, scale analysis performed in the relative vorticity equation (1.4) leads to neglect both the viscous term and the term $D\boldsymbol{\omega}/Dt$ with respect to the term $[(2\boldsymbol{\Omega} + \boldsymbol{\omega}) \cdot \nabla]\mathbf{u}$. Furthermore, if the Rossby number is small, $\boldsymbol{\omega} \ll 2\boldsymbol{\Omega}$ since $\boldsymbol{\omega} = O(U/L)$, thus equation (1.4) reduces to the constraint:

$$(2\boldsymbol{\Omega} \cdot \nabla)\mathbf{u} = 0, \tag{1.11}$$

which, in the case the rotation axis is parallel to the *z* axis, means:

$$\frac{\partial u}{\partial z} = \frac{\partial v}{\partial z} = \frac{\partial w}{\partial z} = 0. \tag{1.12}$$

It follows from (1.12) and from the continuity equation (1.3) that the velocity in planes perpendicular to $\boldsymbol{\Omega}$ must be independent of the coordinate parallel to $\boldsymbol{\Omega}$ and that in planes perpendicular to the rotation axis, the velocity is nondivergent. Furthermore, if the vertical component *w* of the velocity is zero at some level, for example at a rigid, horizontal surface, it rns zero for all *z*. The motion is then completely two-dimensional and can be described as moving in columns of fluid, the so-called *Taylor columns*, each column oriented parallel to the rotation axis and moving so as to maintain this orientation (Taylor 1923).

1.2 The governing equations of barotropic turbulence

The Navier-Stokes equations, in the form (1.2), describe the dynamics of the most general, incompressible, rotating Newtonian flow. If the fluid has an homogeneous density, or more generally the isopycnal surfaces are parallel to the isobars, it is referred to as *barotropic* fluid. If the flow has a low Reynolds number, it is referred to as *laminar* flow. Barotropic turbulent flows, with high Reynolds number (typically $Re \gg 1000$), may be described, under suitable hypotheses, by different approximations of the Navier-Stokes equations, such as the *shallow-water*, the *quasi-geostrophic* and the *two-dimensional* approximations, which show much of the phenomenology of the nonlinear dynamics that can be observed in large-scale, turbulent geophysical flows, when rotation dominates.

In the following, these three approximations are examined, and the governing equations are derived.

1.2.1 Shallow-water approximation

Consider an homogeneous, incompressible, rotating fluid layer with a free surface whose height above a flat bottom is given by $h\,(x, y, t)$, as in figure 1.1. The reference frame is chosen in such a way that the gravity vector, $\mathbf{g} = -g\mathbf{k}$, is antiparallel to the vertical axis *z*, and the rotation axis coincides with the *z*-axis, i.e., $\Omega = \Omega\mathbf{k}$, where $\mathbf{k}$ is the unit vector of the *z*-axis. The velocity vector has components *u*, *v* and *w* parallel to the *x*-, *y*-, *z*-axis respectively.

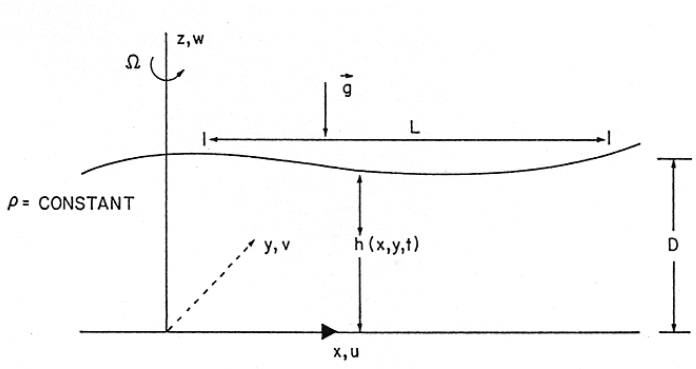

Figure 1.1: Sketch of the shallow-water model for a rotating fluid layer.

The complete Navier-Stokes equations and the continuity equation for such a fluid model read:

$$\frac{\partial u}{\partial t} + u\frac{\partial u}{\partial x} + v\frac{\partial u}{\partial y} + w\frac{\partial u}{\partial z} - fv = -\frac{1}{\rho}\frac{\partial P}{\partial x} + \nu\nabla^2 u$$

$$\frac{\partial v}{\partial t} + u\frac{\partial v}{\partial x} + v\frac{\partial v}{\partial y} + w\frac{\partial v}{\partial z} + fu = -\frac{1}{\rho}\frac{\partial P}{\partial y} + \nu\nabla^2 v \qquad (1.13)$$

$$\frac{\partial w}{\partial t} + u\frac{\partial w}{\partial x} + v\frac{\partial w}{\partial y} + w\frac{\partial w}{\partial z} = -\frac{1}{\rho}\frac{\partial P}{\partial z} + \nu\nabla^2 w,$$

$$\frac{\partial u}{\partial x} + \frac{\partial v}{\partial y} + \frac{\partial w}{\partial z} = 0 \qquad (1.14)$$

where $f = 2\Omega$ is the so-called *Coriolis parameter*, $P = p - \rho\Phi$ is the reduced pressure and ρ and ν are the density and the kinematic viscosity coefficient respectively.

The fundamental hypothesis of the shallow-water model is that the scale depth of the fluid layer, *D*, is much smaller than the horizontal length scale *L*, i.e., that

$$\frac{D}{L} \ll 1. \qquad (1.15)$$

If this hypothesis is satisfied, and if we consider the interior of the fluid layer (far enough from the bottom, in order to be outside the *boundary layer*), it follows from the scale analysis of the Navier-Stokes equations for the x- and y-component of the velocity that the pressure scale must be given by the largest of the following entries (Pedlosky 1987):

$$\rho L \left[\frac{U^2}{L}, fU, \frac{\nu U}{D^2} \right]_{max}, \tag{1.16}$$

where U is the horizontal velocity scale, and the advective time scale is supposed to be of the same order as the local time scale and that the vertical velocity scale, W, is $O\left(DU/L\right)$, as indicated by the scale analysis of the continuity equation. This implies that the ratio between the material derivative and the vertical pressure gradient in the equation for the w-component of the velocity is:

$$\rho \frac{|Dw/Dt|}{|\partial P/\partial z|} = O\left(\frac{D^2}{L^2} \frac{Ro}{[1, Ro, Ek_V]_{max}} \right), \tag{1.17}$$

and the ratio of the viscous term to the vertical pressure gradient is: :

$$\rho \frac{|\nu \nabla^2 w|}{|\partial P/\partial z|} = O\left(\frac{D^2}{L^2} \frac{Ek_V}{[1, Ro, Ek_V]_{max}} \right), \tag{1.18}$$

where $Ek_V = \nu / fD^2$ is referred to as the vertical Ekman number. It turns out that the quantities in the round brackets are smaller than or equal to $\left(D/L\right)^2$ for every Rossby and Ekman number; thus, given the hypothesis (1.15), the most important term in the equation for the vertical component of the velocity is the vertical pressure gradient (see Pedlosky 1987, p. 60, for details). The fluid is then in hydrostatic approximation, since:

$$\frac{\partial p}{\partial z} = -\rho g + O\left[\left(\frac{D}{L} \right)^2 \right], \tag{1.19}$$

where I used the fact that $-g = \partial \Phi / \partial z$. By integrating equation (1.19) and using the fact that the pressure at the surface level is given by a constant value p_0, it comes out that the pressure at any point is simply given by:

$$p = \rho g (h - z) + p_0, \tag{1.20}$$

which implies that the horizontal pressure gradient is independent of z, i.e,

$$\begin{aligned} \frac{\partial p}{\partial x} &= \rho g \frac{\partial h}{\partial x} \\ \frac{\partial p}{\partial y} &= \rho g \frac{\partial h}{\partial y}, \end{aligned} \tag{1.21}$$

so that the horizontal accelerations must also be independent of z (note that for the horizontal pressure, $\partial P/\partial x = \partial p/\partial x$ and $\partial P/\partial y = \partial p/\partial y$). It follows that

the horizontal velocity does not depend on the vertical coordinate if the horizontal components are initially independent of *z*, namely the horizontal motion is decoupled from the vertical one, and it may be described by the following equations:

$$\begin{aligned}
&\frac{\partial u}{\partial t} + u\frac{\partial u}{\partial x} + v\frac{\partial u}{\partial y} - fv = -g\frac{\partial h}{\partial x} + \nu\left(\frac{\partial^2 u}{\partial x^2} + \frac{\partial^2 u}{\partial y^2}\right), \\
&\frac{\partial v}{\partial t} + u\frac{\partial v}{\partial x} + v\frac{\partial v}{\partial y} + fu = -g\frac{\partial h}{\partial y} + \nu\left(\frac{\partial^2 v}{\partial x^2} + \frac{\partial^2 v}{\partial y^2}\right).
\end{aligned} \tag{1.22}$$

The vertical velocity can immediately be derived by integrating the continuity equation (1.14) along z and using the fact that the vertical velocity vanishes at the rigid bottom, which yields:

$$w\left(x, y, z, t\right) = -z\left(\frac{\partial u}{\partial x} + \frac{\partial v}{\partial y}\right). \tag{1.23}$$

By using the value of *w* at the surface level *h*, and knowing that

$$w = \frac{Dz}{Dt}\left(z = h\right) = \frac{\partial h}{\partial t} + u\frac{\partial h}{\partial x} + v\frac{\partial h}{\partial y}, \tag{1.24}$$

it is possible to write the shallow-water equation for the conservation of mass:

$$\frac{\partial h}{\partial t} + \frac{\partial\left(hu\right)}{\partial x} + \frac{\partial\left(hv\right)}{\partial y} = 0. \tag{1.25}$$

Equations (1.22), together with the equation (1.25), constitute the shallow-water approximation. The flow motion occurs by columns of fluid, whose depth is governed by equation (1.25).

In the same way as it has been done for the Navier-Stokes equations, it is possible to derive a shallow-water equation for the relative vorticity by taking the *y*-derivative of the first of (1.22) and subtracting it from the *x*-derivative of the second of (1.22); this yields the equation for the *z*-component of the relative vorticity:,

$$\omega_z = \zeta = \frac{\partial v}{\partial x} - \frac{\partial u}{\partial y} \tag{1.26}$$

$$\frac{D\zeta}{Dt} + \left(\frac{\partial u}{\partial x} + \frac{\partial v}{\partial y}\right)\left(\zeta + f\right) = \nu\left(\frac{\partial^2 \zeta}{\partial x^2} + \frac{\partial^2 \zeta}{\partial y^2}\right). \tag{1.27}$$

The viscous terms represented in this vorticity equation, as well as in equations (1.22), are referred to as *lateral viscosity*, which is different from the viscous effects associated with the bottom friction or the surface wind-stress. Equations (1.22) and (1.27) are valid in the interior of the fluid layer, while near the bottom an appropriate *boundary layer* theory has to be applied. Some consideration on this subject will be done in chapter 2, when dealing with experiments in a rotating tank.

In the inviscid case, the constraints for the validity of the Ertel's theorem are satisfied for the scalar $\lambda = z/h$, and the potential vorticity $\Pi_{SW} = (\zeta + f)/h$ is a material invariant, namely:

$$\frac{D\Pi_{SW}}{Dt} = \frac{D}{Dt}\left(\frac{\zeta + f}{h}\right) = 0. \tag{1.28}$$

This equation states that the relative vorticity of a fluid column varies accordingly to the depth variations of the fluid layer, since the Coriolis parameter is constant in this model; a stretching of the fluid columns forces relative vorticity to decrease, while the contrary occurs for a contraction of the fluid columns.

1.2.2 Quasi-geostrophic approximation

Starting from the shallow-water approximation, I introduce now an additional hypothesis, namely that the fluid is in fast rotation. In term of nondimensional parameters, this is equivalent to suppose that the Rossby number is very small:

$$Ro = \frac{U}{2\Omega L} = \frac{U}{fL} \ll 1. \tag{1.29}$$

For rapidly rotating flows, such as the ones this thesis deals with, it is possible to nondimentionalize the shallow-water equations (1.22) and (1.25), and to expand the velocities in an asymptotic series in the Rossby number (Pedlosky 1987). The zeroth-order approximation leads to the so-called *geostrophic balance* between the Coriolis force and the gradient of the fluid depth (which is related to the pressure gradient); the *quasi-geostrophic* approximation is given by the expansion at the first order.

By introducing the notation:

$$h(x, y, t) = D + \eta(x, y, t), \tag{1.30}$$

where η is the elevation of the free-surface above the level at rest, nondimentionalization of equations (1.22) and (1.25) yields (disregarding the primes):

$$\begin{aligned} Ro\left(\frac{\partial u}{\partial t} + u\frac{\partial u}{\partial x} + v\frac{\partial u}{\partial y}\right) - v &= -\frac{gH}{fLU}\frac{\partial \eta}{\partial x} + \frac{Ro}{Re}\left(\frac{\partial^2 u}{\partial x^2} + \frac{\partial^2 u}{\partial y^2}\right), \\ Ro\left(\frac{\partial v}{\partial t} + u\frac{\partial v}{\partial x} + v\frac{\partial v}{\partial y}\right) + u &= -\frac{gH}{fLU}\frac{\partial \eta}{\partial y} + \frac{Ro}{Re}\left(\frac{\partial^2 v}{\partial x^2} + \frac{\partial^2 v}{\partial y^2}\right), \end{aligned} \tag{1.31}$$

$$\frac{H}{D}\left(\frac{\partial \eta}{\partial t} + u\frac{\partial \eta}{\partial x} + v\frac{\partial \eta}{\partial y}\right) + \left(1 + \frac{H}{D}\eta\right)\left(\frac{\partial u}{\partial x} + \frac{\partial v}{\partial y}\right) = 0, \tag{1.32}$$

where H is used as a scale for the free-surface elevation. In order to have forcing in the fluid, H is choosen in such a way that the coefficient gH/fLU is $O(1)$, i.e., $H = Ro \cdot (f^2 L^2)/g$.

We define the (barotropic) *Rossby deformation radius, R*, as:

$$R = \frac{\sqrt{gD}}{f}, \tag{1.33}$$

and the expression of H/D is given by:

$$\frac{H}{D} = Ro \cdot \frac{L^2}{R^2} = Ro \cdot F, \tag{1.34}$$

where $1/F = R^2/L^2$ is the nondimensional, square Rossby deformation radius. By inserting in equations (1.31) and (1.32) the expansions for the velocity components and the free-surface elevation in series of the Rossby number:

$$\begin{aligned} u\left(x, y, t, Ro, Re\right) &= u_0 + Ro \cdot u_1 + \ldots, \\ v\left(x, y, t, Ro, Re\right) &= v_0 + Ro \cdot v_1 + \ldots, \\ \eta\left(x, y, t, Ro, Re\right) &= \eta_0 + Ro \cdot \eta_1 + \ldots, \end{aligned} \tag{1.35}$$

the $O\left(Ro\right)$ terms in the equations of motion yield (considering that the lowest-order velocity field (u_0, v_0) is nondivergent):

$$\begin{aligned} \left(\frac{\partial u_0}{\partial t} + u_0\frac{\partial u_0}{\partial x} + v_0\frac{\partial u_0}{\partial y}\right) - v_1 &= -\frac{\partial \eta_1}{\partial x} + \frac{1}{Re}\left(\frac{\partial^2 u_0}{\partial x^2} + \frac{\partial^2 u_0}{\partial y^2}\right), \\ \left(\frac{\partial v_0}{\partial t} + u_0\frac{\partial v_0}{\partial x} + v_0\frac{\partial v_0}{\partial y}\right) + u_1 &= -\frac{\partial \eta_1}{\partial y} + \frac{1}{Re}\left(\frac{\partial^2 v_0}{\partial x^2} + \frac{\partial^2 v_0}{\partial y^2}\right), \end{aligned} \tag{1.36}$$

$$F\left(\frac{\partial \eta_0}{\partial t} + u_0\frac{\partial \eta_0}{\partial x} + v_0\frac{\partial \eta_0}{\partial y}\right) + \left(\frac{\partial u_1}{\partial x} + \frac{\partial v_1}{\partial y}\right) = 0. \tag{1.37}$$

If the gradient of the free-surface elevation is eliminated by cross differentiation of equations (1.36) with respect to *x* and *y*, and if the (1.37) is used in order to eliminate the divergence of $\mathbf{u}_1$, it is possible to obtain the *quasi-geostrophic potential vorticity equation*:

$$\frac{\partial}{\partial t}\left(\zeta_0 - F\eta_0\right) + \left(\mathbf{u}_0 \cdot \nabla\right)\left(\zeta_0 - F\eta_0\right) = \frac{1}{Re}\nabla^2\zeta_0, \tag{1.38}$$

where the relative vorticity is given by the expression:

$$\zeta_0 = \frac{\partial v_0}{\partial x} - \frac{\partial u_0}{\partial y} = \nabla^2\eta_0, \tag{1.39}$$

since $u_0 = -\partial\eta_0/\partial y$ and $v_0 = \partial\eta_0/\partial x$ (lowest-order geostrophic balance), and the potential vorticity is:

$$\Pi_0 = \zeta_0 - F\eta_0. \tag{1.40}$$

The problem for quasi-geostrophic motion is then given entirely in terms of the free-surface elevation, related to the pressure. Once η_0 is determined as a solution of (1.38), the horizontal velocity is determined by the geostrophic balance equations.

Since the motion is two-dimensional, in the sense that the horizontal components of the velocity vector do not depend on the vertical coordinate, it is possible to consider the free-surface elevation as a *stream function* $\eta_0 = \psi(x, y, t)$, which satisfy the continuity equation and has the property that the velocity vector is tangent to it in every point of space. In term of stream function, velocity components and relative vorticity are given by (disregarding the subscripts):

$$u = -\frac{\partial \psi}{\partial y}, \quad v = \frac{\partial \psi}{\partial x}, \tag{1.41}$$

$$\zeta = \nabla^2 \psi, \tag{1.42}$$

and the (nondimensional) quasi-geostrophic potential vorticity equation reads:

$$\frac{D\Pi_{QG}}{Dt} = \frac{\partial}{\partial t}\left(\nabla^2 \psi - F\psi\right) + J\left[\psi, \left(\nabla^2 \psi - F\psi\right)\right] = \frac{1}{Re}\nabla^2 \zeta_0, \tag{1.43}$$

where J is the Jacobian operator

$$J = [a, b] = \frac{\partial a}{\partial x}\frac{\partial b}{\partial y} - \frac{\partial a}{\partial y}\frac{\partial b}{\partial x}. \tag{1.44}$$

In the inviscid case ($\nu = 0$), it is possible to verify that two quadratic quantities are conserved in the QG approximation, namely the *total energy* and the *total potential enstrophy*:

$$E = \int_A e \, dA = \frac{1}{2}\int_A \left[(\nabla\psi)^2 + F\psi^2\right] \, dA, \tag{1.45}$$

$$Z = \int_A z \, dA = \frac{1}{2}\int_A \left(\nabla^2 \psi - F\psi\right)^2 \, dA, \tag{1.46}$$

where the integral is calculated over a region *A* where the fluid is contained and on whose boundary the normal velocity vanishes; *e* is the total energy density (sum of the kinetic and the available potential energy) and *z* is the potential enstrophy density. See Pedlosky 1987, p. 164, for a complete demonstration.

1.2.3 The two-dimensional approximation

Both in the shallow-water model and in the quasi-geostrophic model, the motion is two-dimensional, in the sense that the horizontal velocities do not depend on the vertical coordinate, and occurs by columns of fluid of varying depth. The two-dimensional motion is a consequence of the approximations introduced in the complete 3D Navier-Stokes equations, and it is a valid description of the real motion of the modelled fluid as long as the introduced hypotheses are valid.

It is anyhow possible to introduce an *a priori* two-dimensional approximation of the Navier-Stokes equations, by assuming that the motion is completely described by two components of the velocity, which depend only on two coordinates;

if we consider horizontal motions, it means that $\mathbf{u} = (u(x, y, t), v(x, y, t))$. Such a model may be derived from the Navier-Stokes equations in a manner independent of the shallow-water model or the QG model, but it may also be deduced from these models by adding further hypotheses. Consider, as an example, the quasi-geostrophic potential vorticity equation (1.43); if we suppose that the fluid layer has no free surface (the motion is confined between two rigid lids, for instance), $F = 0$ and the QG potential vorticity equation reduces to the (nondimensional) two-dimensional relative vorticity equation:

$$\frac{\partial \zeta}{\partial t} + J[\psi, \zeta] = \frac{1}{Re}\nabla^2 \zeta. \tag{1.47}$$

Note that equation (1.47) can be directly derived from the relative vorticity equation (1.4) by using the fact that the velocity vector has only two components depending on two coordinates. This makes equation (1.47) to be valid also when the QG approximation does not apply, for instance when considering a rapidly rotating fluid layer which is infinitely high.

In the inviscid case, the total energy and the total enstrophy are conserved; their expressions are given by (1.45) and (1.46) with $F = 0$:

$$E = \frac{1}{2}\int_A (\nabla\psi)^2 \, dA, \tag{1.48}$$

$$Z = \frac{1}{2}\int_A \left(\nabla^2\psi\right)^2 dA. \tag{1.49}$$

Note that in the 2D case, the total energy reduces to the total kinetic energy and the total enstrophy reduces to the area integral of the square relative vorticity (apart from the factor 1/2). In the two-dimensional case, all integrals of the form

$$C_n = \int_A \left(\nabla^2\psi\right)^n dA \tag{1.50}$$

are conserved, the conservation of enstrophy being the case with $n = 2$.

The simultaneous conservation of energy and enstrophy is the key property which distinguishes two-dimensional turbulence from three-dimensional turbulence, as pointed out in the next section.

1.3 The inverse energy cascade of 2D turbulence

1.3.1 Spectral representation of variables in the 2D approximation

A useful representation for the variables of the fluid is obtained in the Fourier space, by introducing the 2D spatial Fourier transform:

$$\widehat{f}(\mathbf{k}, t) = \frac{1}{4\pi^2}\iint e^{i\mathbf{k}\cdot\mathbf{r}} f(\mathbf{r}, t)\, d\mathbf{r}, \tag{1.51}$$

as function of the wave vector $\mathbf{k} = (k, l)$ having modulus $|\mathbf{k}| = K$; the Fourier integral representation of the velocity vector, of the relative vorticity and of the stream function are given by:

$$\mathbf{u}(\mathbf{r}, t) = \frac{1}{4\pi^2} \iint e^{-i\mathbf{k}\cdot\mathbf{r}} \widehat{\mathbf{u}}(\mathbf{k}, t)\, d\mathbf{r}, \tag{1.52}$$

$$\zeta(\mathbf{r}, t) = \frac{1}{4\pi^2} \iint e^{-i\mathbf{k}\cdot\mathbf{r}} \widehat{\zeta}(\mathbf{k}, t)\, d\mathbf{r}, \tag{1.53}$$

$$\psi(\mathbf{r}, t) = \frac{1}{4\pi^2} \iint e^{-i\mathbf{k}\cdot\mathbf{r}} \widehat{\psi}(\mathbf{k}, t)\, d\mathbf{r}. \tag{1.54}$$

Inserting the Fourier representation of the stream function in the expressions (1.48) and (1.49) for the total energy and the total enstrophy one obtains

$$E = \frac{1}{2} \iint K^2 \left|\widehat{\psi}(\mathbf{k}, t)\right|^2 d\mathbf{k}, \tag{1.55}$$

$$Z = \frac{1}{2} \iint K^4 \left|\widehat{\psi}(\mathbf{k}, t)\right|^2 d\mathbf{k}. \tag{1.56}$$

In Fourier space, energy density and enstrophy density are linked by the equation:

$$\widehat{e}(\mathbf{k}, t) = \frac{\widehat{z}(\mathbf{k}, t)}{K^2}. \tag{1.57}$$

If we consider polar coordinates (K, θ) in wave vector space, we define the energy density spectrum as

$$\mathcal{E}(K, t) = K \int \widehat{e}(K, \theta, t)\, d\theta, \tag{1.58}$$

and we have:

$$E = \int \mathcal{E}(K, t)\, dK, \tag{1.59}$$

$$Z = \int K^2 \mathcal{E}(K, t)\, dK. \tag{1.60}$$

In the Fourier representation, the instantaneous flow field is often described by a spectral distribution of (kinetic) energy density $\mathcal{E}$ over a certain range of the wave vector modulus K. Mathematically, the integrals in (1.59) and (1.60) run from zero to infinity, but physically, the inverse of the domain size corresponds to the smallest wavenumber ($L \sim K_{min}^{-1}$), and the smallest scale of the flow at which dissipation takes place corresponds to the largest significant wavenumber ($l_d \sim K_d^{-1}$). At scales much larger than l_d and much smaller than L (that is, in the *inertial range* $K_{min} \ll K \ll K_d$), dissipative effects are negligible: at these scales, the nonlinear term in the 2D vorticity equation (1.47) accounts for a redistribution of energy between different scales, which corresponds to turbulent eddies of different sizes.

1.3.2 The inverse energy cascade and the direct enstrophy cascade

In 1941, the Russian mathematician Kolmogorov published his famous work on 3D turbulence in which he showed that the density energy spectrum of the three-dimensional turbulence is proportional to $K^{-5/3}$ (Kolmogorov 1941a, 1941b). He supposed that in a forced 3D turbulent flow the redistribution of kinetic energy in the inertial range results in a net transport of energy from the large scales (small K) of the flow, where energy is injected, towards the small scales (large K), where dissipation occurs. This transfer is well known as the *energy cascade* of 3D turbulence, and has obtained later numerical and experimental verifications (see, e.g., Frisch 1995).

The physical picture of (forced) two-dimensional turbulence is completely different, and this difference with respect to 3D motions comes from the fact that in 2D turbulence, both energy and enstrophy have to be conserved (Kraichnan 1967). Kraichnan argued that, due to this constraint, all interactions in 2D turbulence, viewed in Fourier space, necessarily involve three values of the wave vector modulus: when a transfer of energy occurs from a middle K to either an higher or a lower K, a transfer of enstrophy in the opposite direction must follow, in order to conserve both energy and enstrophy.

By using dimensional arguments, as Kolmogorov had done previously for the 3D case, Kraichnan showed that in 2D turbulence the energy spectrum should satisfy the power law

$$\mathcal{E}(K) \sim \epsilon^{2/3} K^{-5/3}, \tag{1.61}$$

for $K < K_f$, where K_f is the forcing scale and ϵ is the energy flux, and the law

$$\mathcal{E}(K) \sim \eta^{2/3} K^{-3}, \tag{1.62}$$

for $K > K_f$, where η is the enstrophy flux. He proved, moreover, that the validity of (1.61) implies a zero flux of enstrophy between different wavenumbers, together with a constant energy flux, and that the validity of (1.62) yields a zero energy flux and a constant enstrophy flux. For $K_{min} < K < K_f$, where the energy spectrum is proportional to $K^{-5/3}$, an *inverse cascade of energy* occurs (constant ϵ) from higher to lower wavenumbers (largest scales permitted by the boundary conditions), whereas for $K_f < K < K_d$, where the energy spectrum is proportional to K^{-3}, a *direct cascade of enstrophy* occurs (constant η) from lower to higher wavenumbers, where enstrophy is dissipated (at smallest scale); see figure 1.2 for a sketch of the energy spectrum. Both Batchelor (1969) and Kraichnan (1971) later proposed a logarithmic correction to the K^{-3} spectrum of the direct enstrophy cascade.

Kraichnan's argument can be easily verified in this way: consider an initial energy spectrum peaked about a certain wavenumber K_0; the nonlinear interactions will transfer the energy to different wavenumbers, for instance to K_1 and K_2, with $K_1 < K_0 < K_2$. Conservation of spectral energy and enstrophy requires that

$$\mathcal{E}_0 = \mathcal{E}_1 + \mathcal{E}_2, \qquad K_0^2 \mathcal{E}_0 = K_1^2 \mathcal{E}_1 + K_2^2 \mathcal{E}_2, \tag{1.63}$$

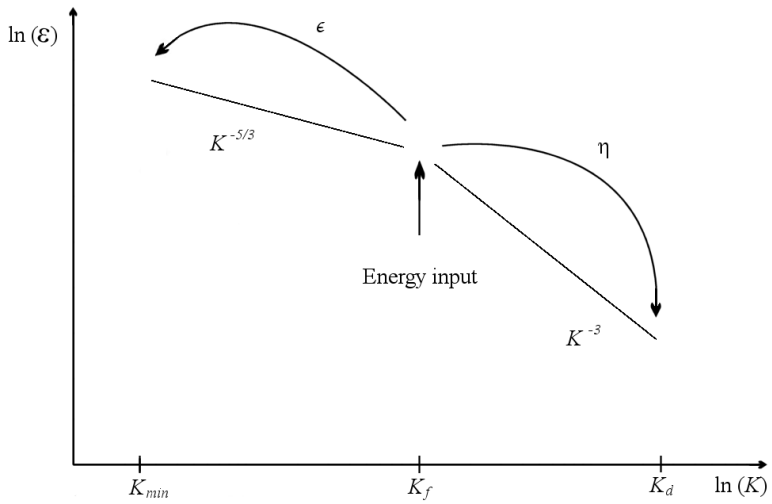

Figure 1.2: Sketch of the energy spectrum in (forced) 2D turbulence. Energy is introduced at wavenumber K_f. An inverse energy cascade occurs, which transfers energy to wavenumbers $K < K_f$, leading to a $K^{-5/3}$ spectrum, whereas a direct enstrophy cascade towards $K > K_f$ leads to a K^{-3} energy spectrum.

from which it follows that the ratios between the energies and enstrophies at the wavenumbers K_1 and K_2 are given by:

$$\frac{\mathcal{E}_1}{\mathcal{E}_2} = \frac{K_2 - K_0}{K_0 - K_1} \cdot \frac{K_2 + K_0}{K_1 + K_0}, \tag{1.64}$$

$$\frac{K_1^2 \mathcal{E}_1}{K_2^2 \mathcal{E}_2} = \frac{K_1^2}{K_2^2} \cdot \frac{K_2^2 - K_0^2}{K_0^2 - K_1^2} \tag{1.65}$$

If we suppose, as an example, that $K_1 = K_0/2$ and $K_2 = 2K_0$, the (1.64) and (1.65) give the ratios $\mathcal{E}_1/\mathcal{E}_2 = 4$ and $(K_1^2\mathcal{E}_1)/(K_2^2\mathcal{E}_2) = 1/4$, which means that energy moves preferentially towards small wavenumbers, while enstrophy moves towards large wavenumbers. This simple example shows also the meaning of the expressions: ”inverse cascade of energy” and ”direct cascade of enstrophy”.

Strictly speaking, Kraichnan’s theory applies only to the case of homogeneous and steadily forced 2D flow, but a direct enstrophy cascade has also been observed in numerical simulations of decaying 2D turbulence, for instance by McWilliams (1984), Brachet et al. (1986 and 1988), Santangelo et al. (1989), starting from an initial random state .

1.3.3 Numerical and experimental evidence

The inverse energy cascade and the direct enstrophy cascade have been object of intense research aimed at observing them both in numerical simulations and in laboratory experiments. The problem is that, in order to obtain a reliable spectrum

for the whole inertial range, a fairly high resolution of numerical and experimental data is required.

Frisch & Sulem (1984) presented the first clear evidence of an inverse energy cascade with a $K^{-5/3}$-spectrum in a numerical simulation of forced 2D turbulence. From the laboratory viewpoint, experiments carried out by Paret & Tabeling (1997 and 1998) and by Paret (1999) in a quasi two-dimensional, magnetically forced electrolyte, showed the existence of an inverse energy cascade and a direct enstropy cascade in the measured energy spectra. The numerical simulations of decaying 2D turbulence indeed showed a K^{-3}-spectrum during the initial stages of the flow evolution (Brachet et al., 1986 and 1988), but a gradual steepening of the spectrum was found at longer times (McWilliams 1984). These late-time energy spectra, moreover, appeared to depend strongly on the type of initial condition (Santangelo et al., 1989).

Numerical simulations have shown, moreover, that Kraichnan's theory might have overlooked one important aspect of the 2D flow evolution:associated with the fact that the energy is transfered from the smallest to the largest eddies, the disordered flow gradually organizes into large and coherent structures, the so-called *coherent vortices*. These vortices are usually long-lived, and carry most of the energy of the flow. Because of the presence of such structures, Kraichnan's assumptions of homogeneity and self-similarity are invalidated, and the observed spectra are usually much steeper than expected. Barotropic coherent vortices are the subject of the next section.

1.4 Barotropic coherent vortices

McWilliams (1984) was the first who realized that freely decaying 2D turbulence *self-organizes* from an initially disordered vorticity field, leading to the emergence of coherent vortices which are stable and long-lived. The presence of coherent vortices has a great impact on the dynamics of the turbulent flow. He suggested that coherent vortices completely dominate the late-time evolution of decaying 2D turbulence and may also arrest the turbulent processes such as the spectral transfer and the selective decay. Starting from these ideas, numerical simulations and laboratory experiments have been carried out in the last two decades, aimed at investigating the emergence, the development and the interactions of coherent vortices, not only in (barotropic) freely-decaying 2D turbulence, but also in forced 2D turbulence, in quasi-geostrophic turbulent flows, and in baroclinic conditions (stratified fluids).

1.4.1 The emergence and development of barotropic vortices in 2D turbulence

By using numerical simulations, it is possible to show that an initially random, two-dimensional, freely decaying vorticity field having a narrow-band kinetic energy spectrum, peaked about a wavenumber K_0 far from the dissipative wavenumbers,

self-organizes into different topological areas, locally breaking down the hypothesis of homogeneous turbulence. Vorticity centers emerge from the random field and start to coalesce, leading to the formation of *coherent vortices*, where the adjective "coherent" identifies a flow structure which is long-lived and has a well-definite shape (see figure 1.3).

Vortices that emerge in 2D turbulent fields tend to concentrate energy and vorticity inside their cores and to assume an axisymmetric shape. These coherent islands of high energy and vorticity move around in a turbulent background of small-scale structures, which on the contrary have generally low energy and vorticity, no coherent shape and short life-time, comparable with the *eddy turnover time* (which can be defined as the inverse square root of the enstrophy).

Coherent vortices may be *monopoles*, i.e., isolated cores of either positive (cyclones) or negative vorticity (anticyclones). Interactions between monopoles lead to the formation of more complex structures or to the *merging* of two vortices, depending on their relative signs. When two oppositely signed monopoles come close together, they usually form a *dipole*, which contains a net linear momentum and may therefore move rapidly through the fluid with a self-sustained propulsion mechanism. On the other hand, the close interaction of two like-signed vortices may lead to their merging and the subsequent formation of one new monopolar vortex, generally larger than the original ones. Merging process occurs when the two vortex centres approach within a sufficiently small distance (Melander et al. 1988); they start to perform a circling motion around each other in which they are deformed and eventually the weaker vortex is absorbed by the stronger one.

Due to all these processes, the number of vortices in a decaying turbulent flow decreases gradually, and their average size increases. In addition, coherent vortices may also be strained by the shear flow produced by all the other vortices, which leads to the formation of thin elongated filaments with strong vorticity gradients, that become part of the turbulent background. This process represent the physical manifestation of the enstrophy cascade towards smallest scales, where it is finally dissipated by viscosity. The formation of vortices, on the contrary, has been associated with the presence of an inverse cascade of energy from small to large scales, but this mechanism alone is not sufficient to explain the emergence of vortices from random initial conditions. Actually, the question 'why do coherent vortices form' has not yet a complete answer, and the issue is still open.

Numerical simulations are generally performed for a flow with a very high Reynolds number, by using *hyperviscosity*[1] as a dissipative term, more than a Newtonian viscous term like in equation (1.47). The modelled flow has a small but finite viscosity. However, the energy cascades towards large scales where dissipation does not occur, and this allows the energy to be practically conserved. By contrast,

[1] In order to confine the effects of damping to the smallest scales and to reach higher effective Reynolds numbers, the ordinary Newtonian dissipation term in the 2D vorticity equation is often replaced by an artificial term of the form $(-1)^{p+1}\nu_p\nabla^{2p}\zeta$; the case $p = 2$ corresponds to *biharmonic viscosity*. The physical interpretation of such numerical dissipation mechanism is still under discussion. See also section 4.

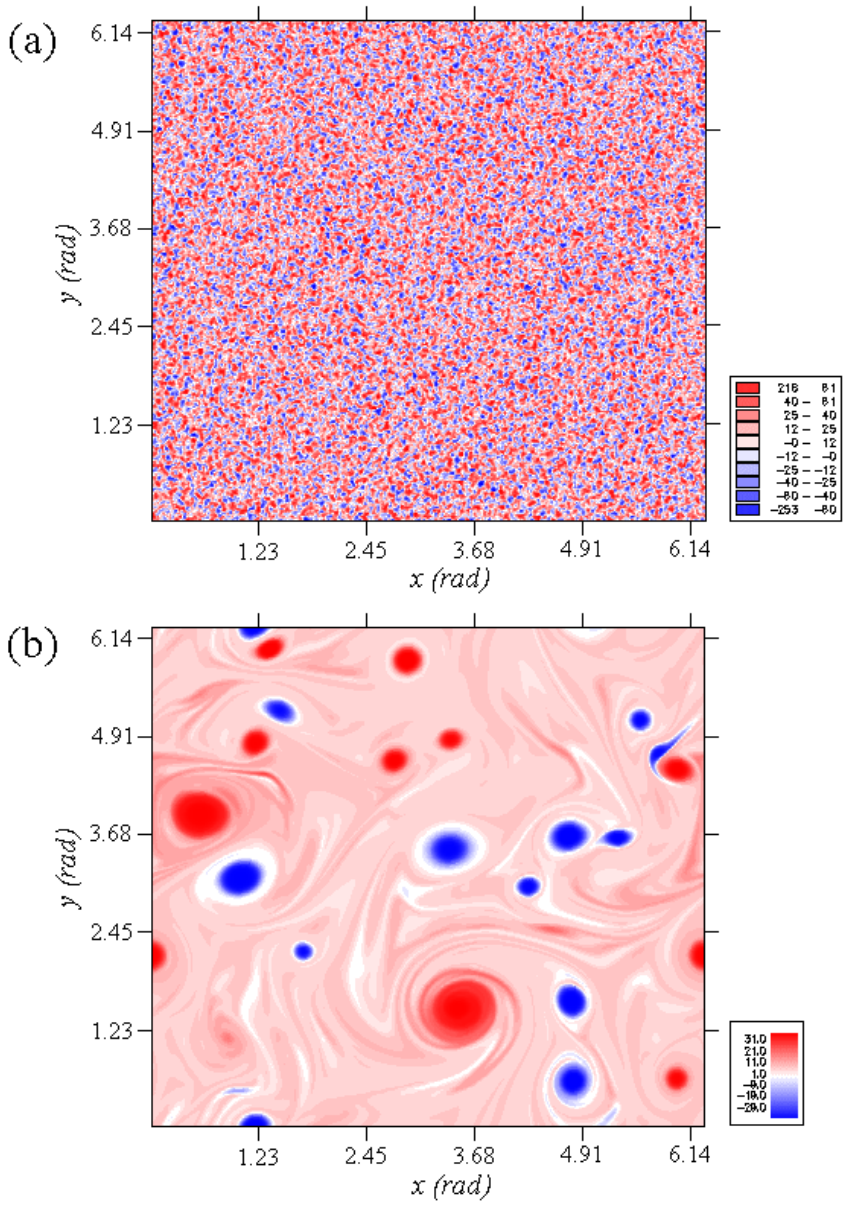

Figure 1.3: Vorticity fields obtained in a numerical simulation of two-dimensional, freely decaying turbulence. In panel (a), the initial conditions for the vorticity are shown, obtained by using a Gaussian random realization for the phases of each Fourier component of the field and a fixed energy spectrum peaked at a certain wavenumber (McWilliams 1990). Panel (b) shows the vorticity field at (nondimensional) time $t = 33$, where fully-developed coherent vortices are clearly distinct from the turbulent background. Cyclones are red, while anticyclones are blue. The simulation is performed in a doubly periodic square domain with size 2π, by using a resolution 512×512 and a time step $dt = 10^{-3}$.

enstrophy decays substantially due to an efficient dissipation at small scale, where it is transfered by the direct cascade. As time goes on, concentrates into coherent vortices and also the enstrophy decay becomes slower.

When the turbulent flow is characterized by fully-developed coherent vortices embedded in a turbulent background, the vortex population appears to be *self-similar* (Weiss 1993, Bracco et al. 2000). Long-time numerical simulations have shown that, if the Reynolds number is sufficiently high, interactions among vortices continue (although with smaller probability) until only one large coherent structure, or a dipole (if the initial circulation is zero) remains, with a size comparable to the dimension of the domain. This quasi-stationary final state is characterized by a linear relationship between the vorticity and the stream function (Matthaeus et al. 1991).

Emergence and development of coherent vortices in (quasi) 2D turbulent flows have been actively studied also in laboratory experiments. Tabeling et al. (1991) have used a thin layer of an electrolyte confined in a small container and forced by an electrical current which is driven by an arrangement of magnets with alternating poles, placed below the bottom of the container. After the forcing is stopped, merging of like-sign vortices results in a fast self-organization of the flow. Although the effects of bottom friction induce strong dissipation, this experimental set-up has been extensively used to verify several aspects of purely 2D freely-decaying turbulence with high Reynolds number. Reasonably good agreement was found between the evolution of statistical vortex properties, such as vortex numerical density and average vortex radius (Cardoso et al. 1994, Hansen et al. 1998) and the scaling theory developed by Carnevale et al. for 2D flows in free decay (1991 and 1992). Another class of experiments was initiated by Couder (1984), who observed the formation of quasi 2D coherent vortices in a thin liquid soap film, initially forced by means of a grid or vertical needles. The dynamics of isolated vortices and vortex interactions have been object of experimental interest in rotating flows. A review on quasi 2D vortices in rotating fluids can be found in a paper by Hopfinger and van Heijst (1993). Alternatively, self-organization in rotating fluids was observed in *spin-up* experiments (van Heijst 1989, van Heijst et al. 1990, van de Konijnenberg 1995), where a fluid, initially in solid body rotation, is accelerated by increasing suddenly the angular velocity of the container; many small-scale structures are created due to the separation of viscous boundary layers, and organize themselves into an array of counter-rotating vortices before the fluid has reached again a state of solid body rotation.

Although this thesis deals only with freely-decaying turbulent flows, barotropic vortices in forced 2D flows have been discussed numerically by Babiano et al. ((1987a, 1987b, 1990, 1994, 1995), Legras et al. (1988), Ohkitani (1991), Maltrud & Vallis (1991, 1993), Provenzale et al. (1995, 1999), and experimentally by Paret & Tabeling (1997, 1998), Paret et al. (1999), Rutgers (1998), Elhmaidi et al. (1993).

1.4.2 Scaling laws

In 1990, McWilliams presented a quantitative analysis of vortex dynamics in 2D flows, introducing a *vortex census* based on vortex properties such as amplitude, size, radial profile and deformation from the axisymmetric shape, for a large number of vortices in a long-time numerical simulation of 2D turbulence. He showed that, for a broad class of initial conditions, the numerical density of vortices (i.e., the number of vortices per unit area) decreases according to $\varrho(t) \sim t^{-\xi}$, with $\xi \approx 0.75$, and that the average extreme of vorticity inside the vortex cores, $\langle\zeta\rangle_{ext}$, is conserved during the self-organization.

Carnevale et al. (1991, 1992) have proposed a new scaling theory for the statistical vortex properties of decaying two-dimensional turbulence. If one assumes that in a inviscid, dilute "gas" of vortices, the vortex density $\varrho(t)$ depends on both the constant energy density e and the constant average peak vorticity $\langle\zeta\rangle_{ext}$, which are related by the expression

$$e \sim \varrho(t) \langle\zeta\rangle_{ext}^2 a(t), \tag{1.66}$$

where $a(t)$ is the average vortex radius, a characteristic length scale $l = \sqrt{e}/\langle\zeta\rangle_{ext}$ and a characteristic time scale $\tau = 1/\langle\zeta\rangle_{ext}$ are determined. Assuming that the evolution of the vortex properties can be expressed as algebraic power laws, dimensional reasoning shows that the exponents of these power laws are all related to one single, "universal" parameter ξ:

$$\begin{aligned} \varrho(t) &\sim l^{-2} (t/\tau)^{-\xi}, \\ a(t) &\sim l (t/\tau)^{\xi/4}, \\ \langle Z(t)\rangle &\sim \tau^{-2} (t/\tau)^{-\xi/2}, \\ \langle r(t)\rangle &\sim l (t/\tau)^{\xi/2}. \end{aligned} \tag{1.67}$$

The value of the parameter ξ is not determined by the theory itself, but has been computed in several numerical studies (Weiss & McWilliams 1993, Dritschel 1993), as well as in experimental studies (Cardoso et al. 1994, Hansen et al 1998). Verification of the scaling laws at very high Reynold number has been discussed by Bracco et al. (2000). The application of the inviscid theory by Carnevale et al. to bounded flows is still under discussion.

1.4.3 Topology of two-dimensional turbulence

As evident in figure 1.2, a two-dimensional vorticity field at late times may be partitioned in two very different spatial regimes: a turbulent background with low energy and vorticity, more or less unstructured, and the coherent vortices, which have high energy and vorticity and strongly coherent shape.

A simple quantitative criterion to distinguish these two areas has been proposed by Okubo (1970), Weiss (1981) and used by Elhmaidi et al. (1993), Provenzale et

al. (1995) and many others. It is based on the difference between the squares of strain and vorticity:

$$Q \equiv \left(S_n^2 + S_s^2\right) - \zeta^2. \tag{1.68}$$

where the normal and shear components of the strain are defined as $S_n = \partial u/\partial x - \partial v/\partial y$ and $S_s = \partial v/\partial x + \partial u/\partial y$. This criterion creates an elementary partition of the vorticity field in two distinct domains, called *elliptic* (where $Q < 0$ and the rotation dominates over the deformation) and *hyperbolic* (where $Q > 0$ and the strain dominates). In a "frozen" field, elliptic regions are characterized by an approximate constancy of the distance between nearby particles, whereas hyperbolic regions are characterized by local exponential divergence of nearby particles. Note, however, that this criterion does not bear any direct information on the chaotic or regular behaviour of particle trajectories in the evolving turbulent field.

Using this criterion, vortices are distinguished from the turbulent background according to the following partition:

1. the *vortex cores* are strongly elliptic domains where $Q \ll 0$ and rotation dominates over deformation;

2. the *circulation cells* at the periphery of coherent structures are strongly hyperbolic domains where $Q \gg 0$ and strain dominates over rotation. They are also regions of high kinetic energy;

3. the *turbulent background* is the region where $Q \approx 0$ and both kinetic energy and vorticity are low; it may be further divided into hyperbolic background patches where $Q > 0$ and elliptic patches where $Q < 0$.

The edge of coherent structures may be identified by the value $Q = 0$, in combination with a high value of kinetic energy (Elhmaidi et al. 1993, Paparella et al. 1997). In figure 1.4, the *Q*-value field which corresponds to the vorticity field in figure 1.3b is shown, and the three topological components are clearly distinct.

Okubo-Weiss' criterion has been discussed by various authors; in particular, Basdevant & Philipovitch (1994) have shown that is strictly justified only in a small portion of the turbulent field, and Hua & Klein (1998) have proposed an extension of this approach that explicitly takes into account time evolution. Recently, Boffetta et al. (2001) have reviewed some different techniques for describing the topology of a turbulent field, and have proposed a new Lagrangian diagnostics, based on the Finite Size Lyapunov Exponent.

Despite all the criticisms, Okubo-Weiss' criterion has been extensively used in the study of absolute dispersion of passively advected fluid particles in 2D turbulence, and it has proven to be of value in the identification of the trapping properties of barotropic coherent vortices and in the observation of different transport regimes associated with different regions of the turbulent flow (Elhmaidi et al. 1993, Provenzale 1999).

Because of its simplicity, in this thesis I shall extensively use this topological diagnostic, when there will be the need of distinguishing the coherent vortices from

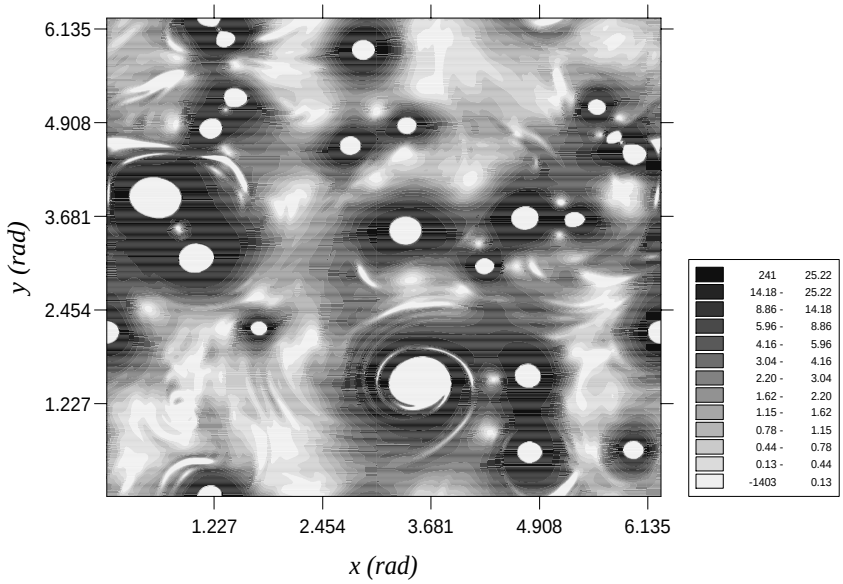

Figure 1.4: The field of the Okubo-Weiss parameter, Q, corresponding to the vorticity field at (nondimensional) time $t = 33$ shown in figure 1.3b. Vortex cores ($Q \ll 0$) are bright and quasi-circular, circulation cells ($Q \gg 0$) are the dark rings that surround vortex cores.

the turbulent background and, from the Lagrangian point of view, of knowing the position of the particles with respect to the vortex cores.

1.4.4 Vortices in the quasi-geostrophic and shallow-water approximations

When free surface effects (QG model, with small Rossby number) or slow rotation effects (SW model) are present, coherent vortices show a different dynamics with respect to the simple case of two-dimensional turbulence. Numerical vortex dynamics in the barotropic quasi-geostrophic approximation, with a finite Rossby deformation radius, has been discussed by Polvani et al. (1989), Larichev & McWilliams (1991), Waugh (1992), Kukharkin et al. (1995). Vortex dynamics in the shallow-water model has been addressed by Ripa (1987), Farge & Sadourny (1990), Polvani et al. (1994), Arai & Yamagata (1994), Stegner & Dritschel (2000).

In the QG model, the presence of a free surface slows down the inverse cascade at scales larger than the Rossby deformation radius, R. Vortices form and grow by merging as in 2D turbulence, until they reach a scale of order R; after this stage, the finite Rossby deformation radius introduces a shield effect and strongly diminishes the interactions among vortices at distances larger than $d_R \approx 2\pi/\sqrt{F}$, where $1/F = R/L$ is the nondimensional Rossby deformatium radius. This in turn leads to a very slow evolution because the vortices interact only weakly with each

other, which slows down the energy transfer to larger scales. The typical length scale of a QG flow with free surface is therefore the Rossby deformation radius.

In decaying shallow-water turbulence with Rossby number of order one, it has been shown that the departure from quasi-geostrophy leads to a significant cyclone-anticyclone asymmetry for which anticyclonic vortices are generally more stable. However, in turbulence many mechanisms may be responsible for this dynamical asymmetry: merging processes, stability mechanisms, wave-vortex interactions, three-dimensional effects. The role played by ageostrophic effects in vortex dynamics is still not well understood.

1.5 Geophysical applications of barotropic turbulence

Barotropic turbulence is often used to describe the large-scale dynamics of the ocean and the atmosphere by means of a simple model. The reason is that the barotropic approximation can be widely applied, as a first approximation, when considering the dynamics of the ocean under the *pycnocline*[2], where the density becomes fairly constant with depth, and the dynamics of the *stratosphere*[3], where density decreases slowly with height. Necessarily, the motions described by barotropic models can only be expected to apply to geophysical phenomena which do not depend in a crucial way on stratification.

1.5.1 Governing equations for large-scale geophysical flows

The fact that both the ocean and the atmosphere have very large horizontal extent and thin vertical thickness[4], makes it possible to describe their large-scale dynamics, in a first approximation, and only for conditions of stable starification, by using a shallow-water model, or a quasi-geostrophic model at latitudes where the local component of the Earth's rotation is important.

The Earth is a non-flat rotating system, thus the complete Navier-Stokes equations must contain the effects due to the curvature of the Earth's surface. In order to describe the flow in the Earth's atmosphere and oceans, the planet is modelled as a sphere of radius R, disregarding the small eccentricity. Spherical coordinates (r, θ, ϕ) are used, where r is the sum of the Earth's radius and the vertical height above the sea level (or the negative depth below the sea level), θ is the longitude and ϕ is the latitude (see figure 1.5a). The complete set of equations of motion on a rotating sphere can be derived by using the hypothesis that the mean thickness

[2]The *pycnocline* is the layer of the ocean, under the surface layer, where a sharp change in density with depth occurs. It lyes between 0.1-1 *km* depth at low latitudes, less at mid-latitudes.

[3]The *stratosphere* is the layer of the atmosphere lying between 10-50 *km* altitude.

[4]The depth of the ocean rarely exceeds six kilometers, and the vertical extent of major current system is usually much less than that. On the contrary, the horizontal scales is hundreds or even thousands of kilometers. Similarly, large-scale atmospheric phenomena have a characteristic vertical scale of ten kilometers, while the horizontal scale is about one thousand of kilometers (*sinoptic scale*)

of the atmosphere and the oceans is much smaller than the Earth's radius (see e.g. Holton 1979).

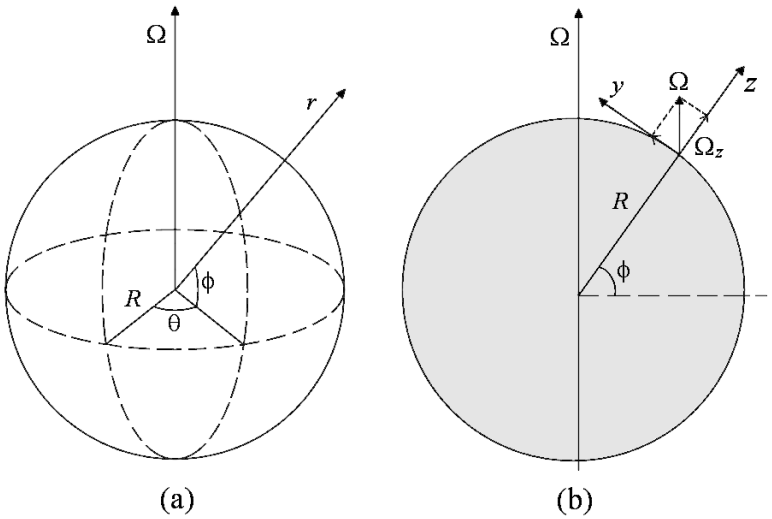

Figure 1.5: Schematic views of the spherical coordinate system used for the Earth (a) and of the local reference frame on a plane tangent to the Earth's surface (b).

In the same way, it is possible to obtain the equations on a rotating sphere in the shallow-water approximation (see e.g. Muller 1995), in which geometrical terms associated with the curved surface of the planet are still present.

However, if the horizontal scales of motion are much smaller than the Earth's radius, the curvature of the Earth's surface can be neglected and a local coordinate system on a plane tangent to the surface of the planet can be used, as depicted in figure 1.5b. In this new reference frame, z is the local vertical height, x and y are the horizontal coordinates tangent to the surface and the rotation vector has components $\mathbf{\Omega} = (0, \Omega\cos(\phi), \Omega\sin(\phi))$. From this it follows that the Coriolis acceleration is given by:

$$2\mathbf{\Omega}\times\mathbf{u} = 2\Omega\left(-v\sin(\phi), u\sin(\phi), -u\cos(\phi)\right) \quad (1.69)$$

$$= \left(-fv, fu, -2\Omega u\cos(\phi)\right), \quad (1.70)$$

where now the Coriolis parameter is $f = 2\Omega\sin(\phi)$ that, in general, depends on latitude.

As a simplification, f is often assumed to be a constant,i.e.

$$f = f_0 = 2\Omega\sin(\phi_0), \quad (1.71)$$

where ϕ_0 is the central reference latitude of the domain considered. This approximation is usually referred to as the *f-plane* approximation. In this approximation, provided that the vertical component of the Coriolis acceleration is negligible with

respect to the pressure gradients (as it is indeed), the flow dynamics can be described by the shallow-water equations (1.22) and (1.25) where the Coriolis parameter is replaced by the expression (1.71). Furthermore, if the Rossby number is small enough, a quasi-geostrophic approximation on the f-plane can be used, and the dynamics can be described by using equation (1.43).

An improved representation of the latitudinal variation of the Coriolis parameter can be obtained by expanding it in aTaylor series around the reference latitude ϕ_0; at first order, the approximation is usually referred to as the *β-plane* approximation. In this case, the equations of motion have an additional term, proportional to the value $\beta = 2\Omega \cos(\phi_0)/R$, which changes the dynamics of turbulence. Throughout this thesis, β-effects are disregarded, and only the f-plane approximation is taken into account when referring to geophysical applications of barotropic turbulence.

Some final remarks have to be made about the role of viscosity in geophysical flows. In the shallow-water and the quasi-geostrophic models described in the previous sections, viscous effects are due to the molecular viscosity. For geophysical flows, the Ekman number is extremely small, if evaluated by using the molecular viscosity coefficient, thus molecular viscous effects can be neglected. Nevertheless, the interaction between the large-scale motions, nearly inviscid, and the small-scale turbulent motions, may leads to exchange of momentum and energy, which eventually affects the large-scale flow. The viscous interaction between different scales of motion can be parameterized by introducing a *turbulent eddy viscosity* both in the horizontal and in the vertical direction, whose coefficients are usually denoted as A_H and A_V, respectively. Equations (1.22), and (1.43) are still valid, by replacing ν by A_H and A_V[5]

1.5.2 Vortices in geophysical flows

Long-lived, large-scale vortices are common features in the Earth's atmosphere and oceans, as well as in the atmospheres of the outer planets. Such vortices are known to greatly influence the transport properties of the global circulation, whose study is a key issue of geophysical fluid dynamics.

Starting from the outer planets, Jupiter's Great Red Spot is a long-lived coherent vortex in the upper atmosphere of this planet, which exist since more than 300 years (Smith et al.1979, Ingersoll 1990, Dowling 1995). Another example is Neptune's Great Dark Spot.

Quasi two-dimensional coherent vortices play an important role in the Earth's atmosphere: examples include the antartic polar vortex (see e.g. McIntyre 1989, 1995), and tropical cyclones (Rossby 1949, Adem 1956, Chan & Williams 1987).

In the oceans, quasi-2D vortices have been detected in the Gulf Stream, in the form of rings that detach from the current (Ring Group 1981, McWilliams 1985).

[5]These coefficients are difficult to estimate in the oceans and in the atmosphere. Typical values for the ocean are $A_H \approx 10^5 \div 10^8$ $cm^2 s^{-1}$ and $A_V \approx 1 \div 10^3$ $cm^2 s^{-1}$; for the atmosphere, $A_H \approx 10^9$ $cm^2 s^{-1}$ and $A_V \approx 10^5$ $cm^2 s^{-1}$ (see Pedlosky 1987).

Other examples include the salty Mediterranean eddies (the so-called *meddies*) in the Atlantic Ocean, which detach off-shore of Portugal's coast (Flierl 1987, Armi et al. 1989, Richardson et al. 1989, 1991), or the large-scale vortices that detach from the Agulhas current near South-Africa (Goni et al. 1997). Such vortices have a diameter of a few hundreds kilometers and may persist for months or even years. Due to their relatively long life-times, some of these vortices may travel for long distances, transporting salt and heat from one region of the ocean to another. This mechanism, in turn, may affect the world-wide ocean circulation, with possible climatic effects. Thus, ortex dynamics and transport by coherent vortices are then key issues in geophysical fluid dynamics; the goal of this thesis is to add a further piece to the puzzle by means of laboratory and numerical simulations in the framework of barotropic turbulence.

Chapter 2

Laboratory experiments on vortex dynamics

This chapter deals with laboratory experiments on the dynamics of long-lived coherent vortices in rapidly rotating, barotropic flows in free decay. The experiments have been carried out in a large rotating tank (diameter of 14 meters) by using different flow visualization techniques: *Particle Image Velocimetry* and *Laser Induced Fluorescence*. First, the experimental set-up is discussed, with a brief description of the flow visualization techniques that have been used. The evolution of the turbulent field, starting from quasi-random initial conditions, and the interactions among the coherent vortices are then described. Time sequences of Eulerian characteristics of the flow and of the vortices are discussed, for different values of the Rossby number, the Reynolds number and the Rossby deformation radius.

2.1 Laboratory modelling of rotating flows

In order to model a geophysical flow for which rotation is important (large-scale flows), laboratory experiments have to be performed in a rotating reference frame. One of the most common techniques consists in carrying out experiments by using water in rotating tanks, which allow to simulate the effects of the Coriolis force. The diameter of these experimental facilities is important in order to reach small values of the Rossby number without rotating too fast, since fast rotation implies nonnegligible free-surface effects (surface paraboloid) that alter the dynamics of the problem. Large-scale rotating tanks also allow to obtain large-scale flows, which may be important for the study of those phenomena that are not scale-invariant or when one would like to disregard boundary effects.

The size of rotating tanks that are available in fluid dynamical laboratories throughout the world may vary between a diameter of one meter up to a diameter of about ten meters; at the moment, the largest rotating tank in the world is the "Coriolis" tank of the "Laboratoire des Ecoulements Géophysiques et Industriels" (LEGI) in Grenoble (France), which has a diameter of 13 meters. This chapter is devoted to the description and discussion of the experiments on vortex dynamics that we have carried out in this large-scale tank.

2.1.1 Fluid dynamics of barotropic flows in rotating tanks

A shallow layer of an homogeneous fluid in a rotating tank can be mathematically modelled, to a first approximation, by means of the shallow-water model or the quasi-geostrophic model (if the Rossby number is small enough), as discussed in chapter 1. These models describe the fluid dynamics in the interior of the flow, but do not consider the predominant viscous effects at the bottom and at the surface, where appropriate e boundary layer models have to be used.

Fast rotating homogeneous flows are dominated by quasi two-dimensional columnar motions, as the Taylor-Proudman's theorem argues. This theorem is strictly valid for inviscid flows, thus it fails in a thin layer near the tank bottom and near the water surface, where boundary conditions make viscous effects to be nonnegligible (in the interior of the fluid, molecular viscosity does not take the flow much away from the columnar motion). No-slip conditions at the bottom and the wind-stress at the surface essentially break down the two-dimensional character of the motion and introduce three-dimensional effects that, although limited in a thin boundary layer, can influence also the interior flow on a long time scale.

Wind-stress effects are due to the rotation of the tank inside the laboratory air, that is at rest; they are negligible if the rotation is not fast, and limited to a very thin layer. Usually, experiments on barotropic flows do not deal with surface phenomena, thus wind-stress is not taken into account. It is also possible to reduce it by covering water with a buoyant curtain, except for the measurement area.

The boundary layer next to the solid bottom is produced by the fact that the velocity vector must vanish at $z = 0$; inside a thin *Ekman layer*, a balance between

pressure gradients, Coriolis and viscous effects is established, while temporal and nonlinear terms are negligibly small. The thickness of the bottom Ekman layer is given by (see e.g. Pedlosky, 1987, p.177):

$$\delta_E = \left(\frac{2\nu}{f}\right)^{1/2}, \tag{2.1}$$

where I have now defined the (vertical) Ekman number as two times the definition given in (1.8):

$$Ek = \frac{2\nu}{fD^2}, \tag{2.2}$$

with $f = 2\Omega$ and D the vertical length scale, as in the shallow-water model discussed in section 1.2.

In laboratory experiments, the Ekman number is usually very small ($Ek \approx O(10^{-4})$, implying that the Ekman layer thickness is also very small compared with the total fluid depth, since $\delta_E = D\sqrt{Ek}$. Anyway, this thin layer influences the interior flow on a characteristic *Ekman time scale*, whose expression is given by:

$$T_E = \frac{2}{f\sqrt{Ek}} \equiv \frac{D}{\sqrt{\nu\Omega}}. \tag{2.3}$$

This is due to the fact that, when the interior flow is not spatially uniform, the flow within the Ekman layer induces a non-zero vertical velocity on top of the Ekman layer, which is proportional to the relative vorticity in the interior (*Ekman pumping*, see e.g. Pedlosky 1987, section 4.5):

$$w|_{z=\delta_E} = \frac{1}{2}\delta_E\zeta. \tag{2.4}$$

This in turn implies that fluid is exchanged between the Ekman layer and the interior, giving rise to what is called *Ekman blowing/suction* of fluid, namely the entrainment or detrainment of fluid from the Ekman layer to the interior or the contrary, according to the sign of relative vorticity. When the vorticity is positive, there is pumping of fluid from the boundary layer, thus squeezing the fluid columns; on the other hand, when the interior flow has negative relative vorticity, there is suction of fluid towards the boundary layer, thus stretching the flow. In both cases, the interior relative vorticity decays exponentially, with a characteristic time scale given by (2.3).

To verify this, it is sufficient to integrate the continuity equation for the shallow-water model by using (2.4) as bottom boundary condition. One can then obtain that the horizontal divergence is related to the entrainment or detrainment of fluid:

$$\frac{\partial u}{\partial x} + \frac{\partial v}{\partial y} = \frac{1}{2}\zeta\sqrt{Ek}. \tag{2.5}$$

By inserting equation (2.5) in the vorticity equation (1.28), and neglecting all nonlinear terms and lateral friction (in order to isolate the bottom friction effects), the

vorticity equation reduces to:

$$\frac{\partial \zeta}{\partial t} = -\frac{1}{2} f \zeta \sqrt{Ek}, \tag{2.6}$$

which implies:

$$\zeta = \zeta_0 e^{-t/T_E}, \tag{2.7}$$

with the Ekman time scale given by (2.3).

From (2.6) one sees that the effects of the bottom friction can be taken into account by adding a linear term to the vorticity equation in the shallow-water model or in the quasi-geostrophic approximation. However, weak nonlinear Ekman friction terms may induce differences with respect to the linear approximation which is commonly used.

2.2 Experimental set-up for the study of vortex dynamics

The experiments discussed here are devised to explore the dynamics of an incompressible, homogeneous and rapidly-rotating shallow fluid, by using the large "Coriolis" facility. The fluid layer has a free surface and a flat bottom. Only an initial forcing is introduced, then the initial energy decays by dissipation.

2.2.1 The "Coriolis" rotating hydraulic tank of LEGI.

The large rotating "Coriolis" platform (diameter of 14 meters) of LEGI in Grenoble supports a circular tank with a diameter of 13 meters and a depth of 1.2 meters (see a picture of the facility in figure 2.1).

The tank rotation period can be adjusted continuously from about 20 to 1000 seconds and the rotation is counterclockwise. The tank can be filled, up to about 180 *tons*, either with homogeneous fluid (fresh or salt water) or with stratified fluid, by using different concentrations of salt. The maximum total weight of the facility is of the order of 300 *tons*. The platform is supported in its center by a spherical thrust bearing, and in its periphery by 23 rollers equally spaced around the circumference. The platform and the circular tank rotate around a central "pivot", used for the electrical and digital networks, as well as to fix a co-rotating structure from whom flow visualization devices can be hung; a "bridge" is also fixed to the central pivot and it is used for people to manage the experiments. The discrepancy from the vertical is about $3 \cdot 10^{-6}$ *rad*.

Water temperature and salinity of water are stabilized and controlled with high precision, due to the thermal inertia of such a large amount of fluid. Water is introduced from the bottom while the table is rotating. In stratified experiments fresh water is introduced first, followed by salt water. In order to avoid excessive mixing, the tank is filled in approximately 4-5 hours. Additional 2-3 hours are allowed for the fluid to spin up to approximate solid body rotation; residual motions in the tank, due to convection and wind stress effects, are estimated to be of the order of 0.5 *cm*/*s*.

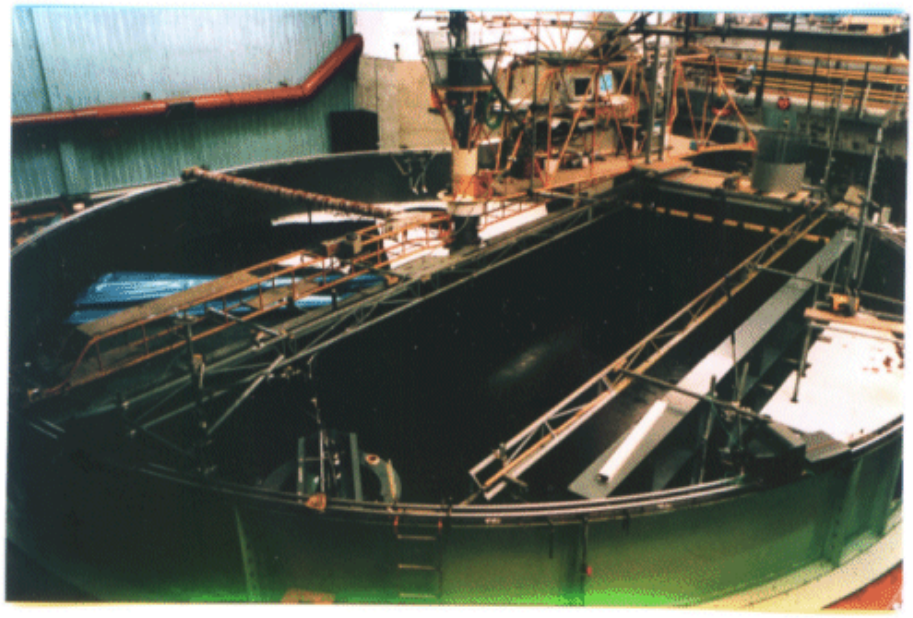

Figure 2.1: The ”Coriolis” rotating tank of the *Laboratoire des Ecoulements Géophysique et Industriels* in Grenoble (France).

2.2.2 The study domain

For the present experiments, we did not use the whole tank: simple boundary conditions for the study domain are obtained by using a closed rectangular channel, 8.4 *m* long and 4 *m* wide, placed in a off-diameter position in the “Coriolis” tank. In this way we reduce the length scale of the flow, but this choice allows to compare the experiments with numerical simulations, which are usually performed in simple square or rectangular domains. Furthermore, the presence of the central pivot in the tank would have constituted an obstacle in the study domain, leading to the possible creation of wakes in the flow, if the whole circular tank had been used. Sketch in figure 2.2a provides a top view of the tank, of the channel and of the study domain, while picture 2.3 shows the rectangular channel and the ”rake” used to generate the initial forcing.

2.2.3 Generation of the initial conditions

We generate quasi-random initial condition by moving forward and backward a rigid frame of equally spaced, vertical flat teeth, that we call the ”rake.” Each tooth has a height of 1 *m*. The reason for the double passage is to create initial conditions as random and homogeneous as possible. The first passage of the rake, in fact, creates some so-called *von Karman's streets* of small-scale wake vortices; the second passage destroys the vortices already formed and creates new ones, adding random turbulent components to the flow.

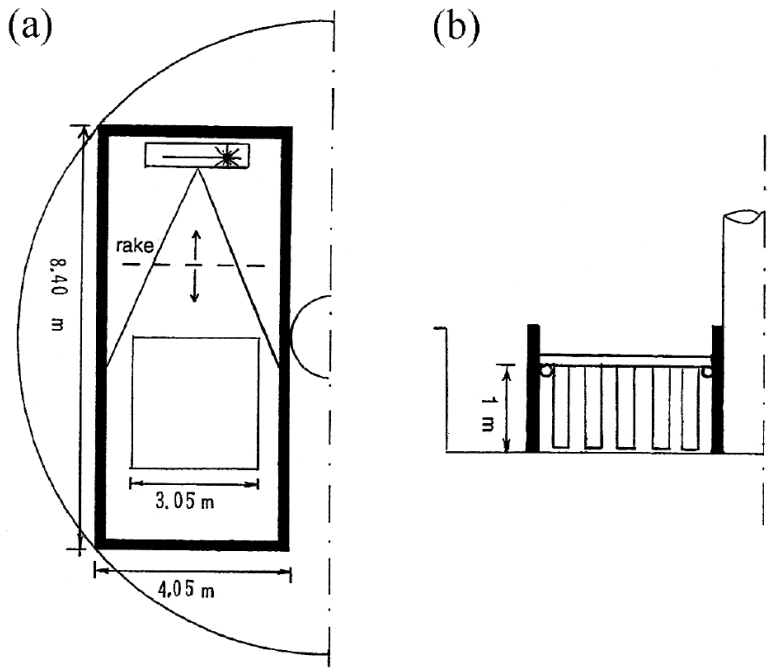

Figure 2.2: Top view (a) and cross section (b) of the rotating tank with the experimental setup. In the top view, the channel and the study domain are shown. The square area depicted in figure is the camera view field, and the two oblique lines indicate the edges of the laser sheet. In the cross section, I also show a sketch of the "rake".

The initial input of energy occurs at a length scale which depends on the spacing between the rake teeth and the individual tooth width. The horizontal spacing between two neighboring teeth is chosen to be either 17.5 or 35 *cm* and the tooth width is respectively 5 or 10 *cm*. Since the rake has a total length equal to the smaller side of the rectangular tank, a total of 18 or 9 vertical teeth are used. Figures 2.2b and 2.3 provide images of the system. The teeth spacing and width determine also the initial size of small-scale vortices.

The initial quasi-random turbulent field is then generated by a computer-controlled movement of the rake along the tank, obtaining what we call "rake turbulence", i.e., a quasi-two-dimensional analog of "grid turbulence." Of course, the initial turbulence has a three-dimensional structure anyway, and it is only the rotation of the system that eventually generates an almost two- dimensional motion at later times (after some minutes).

Together with the above mentioned method for creating initial, quasi-random turbulence, we use also a method specifically designed for generating a vortex in a specified position in the study domain. This method uses a cylinder with diameter of 1 *m*, that is hanged from a small rotating hand-crane, allowing to lower it in the water at pre-determined positions in the channel. The cylinder is equipped with four rotating flat blades that allow for spinning up the water inside the cylinder,

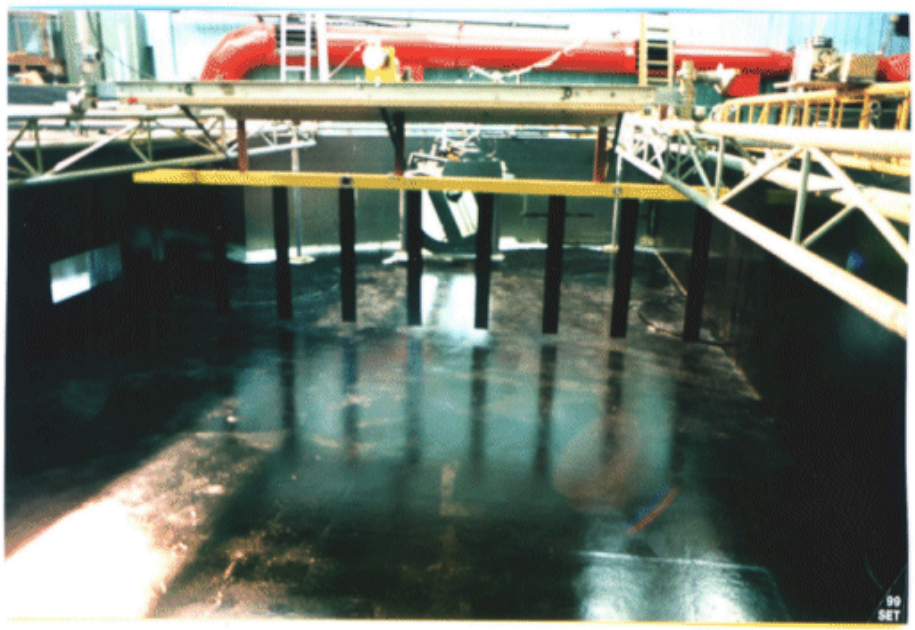

Figure 2.3: Picture of the rectangular channel and of the "rake" used to generate the initial quasi-random forcing of the fluid.

with a period corresponding to the desired turnover time of the vortex. The cylinder is then lifted up slowly, and a vortex is created into the turbulent flow. With this method, it is impossible to obtain a pure cyclonic or anticyclonic vortex, due to zero mean circulation in the flow, and for cyclonic rotation inside the cylinder a tripole is generally formed.

2.2.4 Parameters of the experiments

Different values for the control parameters of the flow are obtained by varying the speed of the rake, the teeth spacing and the rotating period. This leads to different values for the initial Rossby and Reynolds numbers, which are summarized in Table 2.1. Here, the Rossby number is defined as $Ro = U/2\Omega L$ and the Reynolds number is $Re = UL/\nu$, where U is the velocity scale of the flow, L is the horizontal length scale, Ω is the angular velocity of the tank, ν is the kinematic viscosity of water ($\nu = 10^{-6}\ m^2/s$). In order to estimate the initial value of these numbers, we use the speed of the rake as the velocity scale and the mean of the spacing between two rake teeth and their width as the length scale. Later on, the dominant length scale becomes the vortex radius (that is larger than the rake spacing and the tooth width), the velocity becomes smaller due to dissipation, and the Rossby number decreases, down to an order of $O(10^{-1})$.

The water depth in the experiments is $D = 90\ cm$; the Ekman number defined in (2.2) is then $O(10^{-5})$, leading to a thickness of the bottom Ekman layer of a few

Rotation period T (s)	Rake speed U (cm/s)	Rake spacing (cm)	$Ro_{in} = U/2\Omega L$	$\mathrm{Re}_{in} = UL/\nu$ ($\times 10^4$)
50	13	35	2.3	2.9
	6.5	35-17.5	1.1-2.3	1.5-0.7
	3.25	35-17.5	0.6-1.1	0.7-0.4
	1.62	35	0.3	0.4
100	6.5	35-17.5	2.3-4.6	1.5-0.7
	3.25	35-17.5	1.1-2.3	0.7-0.4
	1.62	35	0.6	0.4

Table 2.1: Parameters of the experiments.

millimeters, and to an Ekman time scale of about one hour. The influence of the bottom friction is then negligible in these experiments, which are performed for 40 minutes each (corresponding to more than 50 rotations of the tank). We have also performed some experiments by using a water depth of 35 *cm*, in order to see the effects of a smaller Rossby deformation radius ($R = \sqrt{gD}/2\Omega$); in this case, the Ekman time scale reduces to about 20 minutes, leading to a rapid decay of vorticity which slows down or even blocks the self-organization of turbulence. Therefore, it is difficult to see the effects of the Rossby deformation radius, which reaches the minimum value of 7 *m* in our experiments.

2.2.5 Observation and measurement techniques

In order to obtain qualitative and quantitative measurements of the Eulerian characteristics of the flow, two techniques have been adopted: *Particle Image Velocimetry* (PIV) and *Laser Induced Fluorescence* (LIF).

Particle Image Velocimetry

Particle Image Velocimetry (also called *Digital Particle Image Velocimetry* to point out the fact that it uses digital images of the flow) is used to measure the instantaneous velocity field in a planar section of the flow. The technique consists essentially in determining the local displacements of patches of small passive tracers over a sufficiently small time interval in such a way that the measured mean velocities of the patches provide a close estimate of the global instantaneous velocity field. See Raffel et al. (1998) for a review on PIV technique, and Jambunathan et al. (1997), Westeerweel et al. (1997), Scarano & Riethmuller (1998, 1999a, 1999b) for recent improvements on the processing algorithms.

For the use of the PIV, we adopted the following experimental configuration:

- a continuous $8W$ Argon laser source with a wavelength of 488 *nm* (green light),
- a deflecting mirror (with an oscillation frequency of 120 *Hz*) in order to expand the laser beam into a laser sheet either in the horizontal or in the vertical plane. The sheet thickness is between 5 and 10 *mm*,
- a dual channel cross-correlation Kodak Megaplus camera (model ES 1.0) with a CCD sensor having a pixel array of 1008(H)$\times$1018(V) and a minimum pulse separation of 5 μs,
- a personal computer equipped with a frame grabber and a very fast hard disk in order to collect and store the images at the maximum available frame rate (30 *Hz*).

The experimental set-up of this visualization apparatus is shown in figure 2.4, and the position of the (3.05$\times$3.05) m^2 camera view field is shown in figure 2.3a.

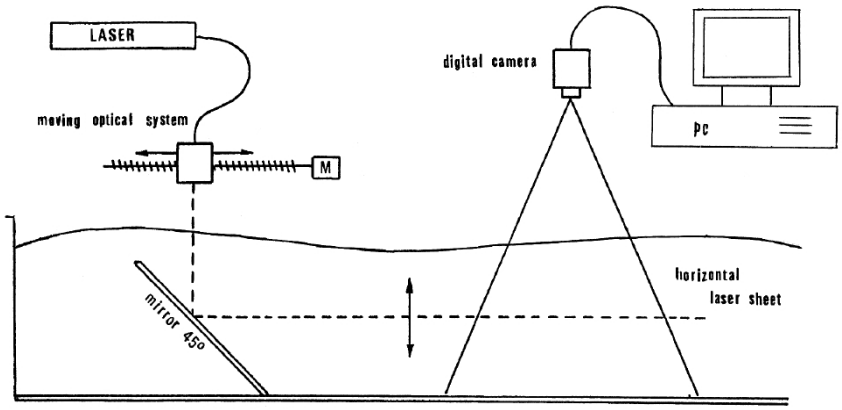

Figure 2.4: Experimental set-up for the use of PIV and LIF visualization techniques. A laser produces a coherent beam which is expanded in a sheet by using a deflecting mirror. Another mirror, set at 45 degrees with respect to the ground, is used to expand the sheet horizontally. The horizontal laser sheet may be positioned at different vertical levels by acting on the moving optical system. During the experiments, we have positioned the sheet about fifteen centimeters below the water surface, in order to avoid wind-stress effects. A CCD camera captures images of a portion of the flow illuminated by the laser sheet, and the binary data are sent to a Personal Computer where they are stored, and processed afterwards.

In order to take images of tracers by the CCD camera, the flow is seeded uniformly with a mixture of 60 μ Orgasol and 150 μ Optimage particles (with a nominal density of about 1.02 g/cm^3). Special attention is paid to determine the numerical density of seeding particles ('seeding density') in the channel, in order to obtain images of the flow with an optimum number of particles per pixel (ppp). Fincham & Spedding (1997) produce a plot of the optimum seeding density versus particle diameter in the images for strong and weak shear. The diameter of the

image of the particles we use is $d \cong 3$ pixels and shear can be strong in the circulation cells around vortex cores. Based on the above estimate, we select a density of $N \cong 0.1$ *ppp*.

In the experiments described here, we use the cross-correlation technique to obtain particle displacements from images of the seeded flow. To this end, on preselected times we record a burst of images, i.e. a series of frames containing the particle positions at different but closely-spaced times. The total recording time for each experiment is 40 minutes. During this period, a total of 80 bursts are recorded, at intervals of 30 seconds. Each burst is composed by 4 image frames taken with different time delays, aimed at having several possible combinations of particle displacements. This is designed to allow for choosing the best pair of frames during the processing phase. At the beginning of the evolution, when the velocities are high, we prefer to use frames that have a small time separation, while on later times we prefer to use frames with a larger time separation. In addition, time delays are linearly increased during each experiment, to approximately compensate for the turbulence decay and the consequent velocity decrease.

The *Correlation Image Velocimetry* (CIV) algorithm by Fincham and others is then used to obtain the Eulerian velocity on a grid by processing the raw PIV images of the particles in the fluid. This algorithm incorporates advanced features that improve the performance and allow for obtaining accurate values for the velocities: the decoupling of the interrogation window from its fixed location in the first image to any arbitrary location in the cross-correlated second image, inside a search box; the possibility of performing a hierarchical scheme of multi-passes with increasing spatial resolution; the on-line correlation peak averaging of Hart (1998) for reducing the wrong vectors. See Fincham et al. (1991), Fincham & Spedding (1997) and Fincham & Delerce (2000) for details. Derived quantities, such as vorticity or horizontal divergence, can then be calculated from the velocity field using local splines.

The experiments carried out in the "Coriolis" rotating tank involve a large camera view area, larger than that usually adopted in PIV experiments; due to this characteristic, the available resolution of velocity fields is determined not only by intrinsic fluid dynamical limits (i.e., the minimum length scale of the flow for which the hypothesis of a uniform motion of tracer patches is still valid, or the numerical density of seeding), but also by strong technical limits: the camera optics, the light sensibility and the pixel resolution of CCD, the tracer size compared to the distance of the camera from the visual plane. The difficulties of optimizing large scale PIV experiments influence the final resolution of the data. Nevertheless, the possibility of performing a hierarchical scheme of multi-passes, offered by the CIV algorithm, and the use of 50% overlapping of the interrogation windows, allows to attain a maximum resolution of 3.6 *cm*, which means that the velocity fields over the physical area of 3.05×3.05 *m* have a maximum resolution of 80×80 grid points (a narrow band at the edges of the PIV images is, in fact, not available for the cross-correlation analysis, due to the possible entrance or exit of tracers through the edges of one of the two cross-correlated images). Higher resolution are no more

reliable.

Outlier detection and filtering in PIV

An important point is the possible residual presence of wrong vectors (also called "outliers") in the velocity field at the end of each correlation step, also after use of Hart's detection and correction in the first pass. These outliers have to be detected and filtered by the use of automatic numerical procedures before each subsequent pass and before calculating of the derivatives. I have addressed the problem of outlier detection and filtering by developing an algorithm, additional to the main CIV algorithm, that improves their detection. The most used algorithms for the detection of an outlier need to evaluate the mean (or median) of its neighbours, together with the standard deviation, and use the latter as a threshold value for the difference between the interrogated vector and the mean (or median) (see, e.g., Raffel et al. 1998 and Westeerweel 1994). However, the standard deviation itself can be affected by errors due to the possible presence of outliers in the nearby vectors, or it can be so small that very slight differences with respect to the mean or median of nearby vectors are rejected. To obviate this problem, I have tried different solutions; one of them is to use an appropriate, local, adaptive threshold which is not simply given by the standard deviation multiplied by a constant, but it is a more realistic function of the standard deviation itself, satisfying two requests: first, when the standard deviation is small, the threshold should be larger; second, when the standard deviation is large (indicating a possible prsence of outliers in the nearby vectors), the threshold should be smaller, apart some corrections due to the presence of strong gradients in the flow.

The simplest proposed expression for the threshold is:

$$Thr = (A\exp(-B\sigma) + C)\sigma, \tag{2.8}$$

where σ is the standard deviation, calculated by using the eight nearby vectors of the interrogated one, and *A, B, C* are constants to be determined in an adaptive way, by considering the statistical and/or the fluid dynamical properties of the flow.

A simple way is, for each velocity field, to evaluate the value which corresponds to the maximum of the *Probability Density Function* (PDF) of the standard deviation, and to use it for determining the maximum of the threshold function; this leads to an expression for the constant *B*. The constant *C* may be locally determined by evaluation of gradients nearby an interrogated vector. Lastly, the constant *A* may be fixed in such a way that the threshold has a certain maximum value, e.g. $3\sigma_{max}$, where σ_{max} is the value of the standard deviation at the threshold maximum.

The application of this algorithm to the PIV velocity fields recorded in the present experiments improves the detection of outliers and, above all, it improves the percentage of valid vectors which are detected as wrong vectors by usual validation algorithms.

Another algorithm has been developed for the detection of outliers in multi-passes PIV. It simply uses the lowest order, low-resolution velocity field (validated

for instance by using the technique described above) as a ”pattern” for the higher-resolution field; vectors which have large differences with respect to the corresponding interpolated vector in the low-resolution field, are rejected.

The velocity field is then interpolated by local splines in the positions where vectors have been filtered out, in order to get a field on a regular grid.

Laser Induced Fluorescence

Here I recall briefly the use of Laser Induced Fluorescence. LIF is a technique that we have used only in order to visualize the instantaneous flow structures and to tell apart the vortex cores from the turbulent background. The arrangement for using LIF is the same used for PIV; the difference is in the seeding, which for LIF is *Disodium fluorescein* (green dye) with an absorption wavelength of 500 *nm* and an emission wavelength of 535 *nm*. The light recorded on the digital images is not the scattered light, as for PIV particles, but the fluorescent light emitted during the transition of electrons in the dye molecules from the lowest vibrational level in the excited singlet state to the non-excited state.

See Walker (1987) and Aanen et al. (2000) for details on this technique, which is efficiently used for passive tracer concentration measurements, since the fluorescent light emitted by the dye molecules (thus, the image intensity) is approximately a linear function of the dye concentration.

2.2.6 Data collection

During the experiments we collect two types of raw data:

- photographic images and sequences of digital images of the fluid seeded with fluorescein. The flow structures are visible without any post-processing. It is possible to visually follow the time evolution of the coherent vortices and the displacement of the float-like tracers;

- sequences of digital PIV images of the fluid seeded with microscopic particles. These images need post-processing in order to extract quantitative data on Eulerian velocity, vorticity, kinetic energy, horizontal divergence and other dynamical variables.

In order to get direct Lagrangian information, we also use a few float-like tracers, whose description is postponed to Chapter 3; digital images of the positions of these tracers are available, and post-processing techniques (float tracking) can be used in order to extract quantitative information on their trajectories.

The sequences of velocity fields obtained with PIV processing form a large data set available for detailed studies of the Eulerian properties of the vortices with different values of the Rossby and Reynolds numbers, as well as for studies of passive tracer transport (which is the topic of Chapter 3).

2.3 The evolution of the quasi-2D turbulent field

In this section, I refer to an experiment carried out by using: tank rotation period $T = 50$ *s*, rake speed $U = 6.5$ *cm/s* and rake spacing between two teeth $l = 35$ *cm*. This corresponds to an initial Rossby number $Ro = 1.1$ and a Reynolds number $Re = 15000$. Comparisons between different experiments are discussed in the next section.

After the passages of the "rake", the flow is almost unstructured; small scale vortical patches, produced as wakes by the rake teeth, interact each other and undergo merging phenomena, which lead to a rapid increase of size. Figure 2.5 provides a sequence of pictures of the flow obtained by using LIF; see figures 2.6, 2.7 and 2.8 for the fields of velocity, vorticity, kinetic energy and Q-value at different times, obtained by using PIV. During this first stage, the turbulence has a three-dimensional structure, as we have verified by illuminating the seeded flow with vertical laser sheets.

After some minutes (between 5 and 8, depending on the rotation period), individual coherent vortices emerge as structures distinct from the turbulent, unstructured background, and their following evolution can be clearly tracked. The separation between vortices and background, then, occurs very early after the initial energy input, where "early" means that the time scale at which this separation occurs is very small when compared to the time scale of evolution of the freely-decaying turbulent flow: after more than one hour, in fact, the flow does not yet come back to the state of rest, and evolution is still active, although the velocities are feeble.

During the first stage in which vortical patches and turbulent background are not clearly distinct, an important role is played by the three-dimensional component of turbulence: for an initial Rossby number of order one, anticyclonic[1] vorticity filaments subject to a straining field in a quasi-2D flow are destabilized by rotation, whereas rotation has a stabilizing effect (compared with the non-rotating case) on cylonic vorticity filaments (Lesieur 1993, p. 81). This implies that, after the separation between vortices and background, cyclones are more abundant than anticyclonic vortices, which have been destabilized before the self-organization of the turbulent field could reinforce them. This effect has been verified in all the experiments we have performed, with different Rossby and Reynolds number: already at early times, there are mostly cyclones in the flow, and the few anticyclones are generally weaker. This effect is strongly different from the results obtained numerically by using both a quasi-geostrophic model (in which there is no asymmetry at all between cyclones and anticyclones) and a shallow-water model (which predicts an asymmetry, but favours anticyclonic vortices), and is due to the initial three-dimensionality of the flow. When the fluid is very shallow (in the case with 35 *cm* depth, for instance), also the Ekman layer contributes to destabilizing an-

[1] I remind that "cyclonic" and "anticyclonic" are terms referred to the rotation of the reference frame: a cyclonic motion occurs in the same direction as the reference frame rotation, while it is the contrary for an anticyclonic motion.

ticyclonic vortices, as pointed out by means of experimental evidence by Chabert D'Hieres et al. (1989). The combination of these two effects leads to a total lack of fully-developed anticyclones in experiments with very shallow water.

The second stage of evolution of the turbulent flow is, on the contrary, almost two-dimensional, and it can be described by means of the quasi-geostrophic model in the case of small Rossby numbers ($Ro = O(10^{-1})$), with possible ageostrophic effects when the Rossby number is larger.

Particular care is devoted to test the hypothesis of quasi two-dimensional flow at this stage. A qualitative confirmation of the two-dimensionality of the flow is obtained during the experiments, as the horizontal laser beam used to illuminate the flow, positioned at different vertical levels in the fluid, shows the same structure on different horizontal planes (a fact that confirms the columnar structure of the flow). More quantitatively, the estimated values of the horizontal divergence are close to zero, as discussed further below. This happens for both the slower (period of 100 *s*) and the faster (period of 50 *s*) tank rotation speed and it becomes more clear as the turbulence evolves.

During this stage, coherent vortices carry most of the energy and enstrophy of the flow, and interact with each other mainly by merging processes which increase their size up to a diameter of order one meter (one third of the camera view field). This stage has a long duration, more than half an hour if the initial Reynolds number is higher than 10000, and it is characterized by advection of vortices throughout the turbulent flow, induced by the field created by the other coherent structures. This advection of vortices increases the probability of interactions, which are mainly reduced to merging or straining, since cyclone-anticyclone coupling is not possible due to the lack of anticyclonic vortices. The turbulent field becomes more and more inhomogeneous: vortices with increasing size are separated by large unstructured areas of low energy.

As time goes on, dissipation reduces drastically the energy in the system; at this point the background has negligible velocity, and the energy is concentrated in large scale rotating vortices. Close interactions among coherent vortices are less and less likely due to the reduction of their mutual advection. The only motion which persists is the slow rotation of fluid inside vortices, still visible after more than ninety minutes after the start of the experiment, if the Reynolds number is sufficiently high.

2.4 Characteristics of the turbulent field at different Rossby and Reynolds numbers

I compare here four different experiments, characterized by the following initial parameters:

1. $Re = 29000$ and $Ro = 2.3$, obtained by using: tank rotation period $T = 50$ *s*, rake speed $U = 13$ *cm/s* and rake spacing $l = 35$ cm.

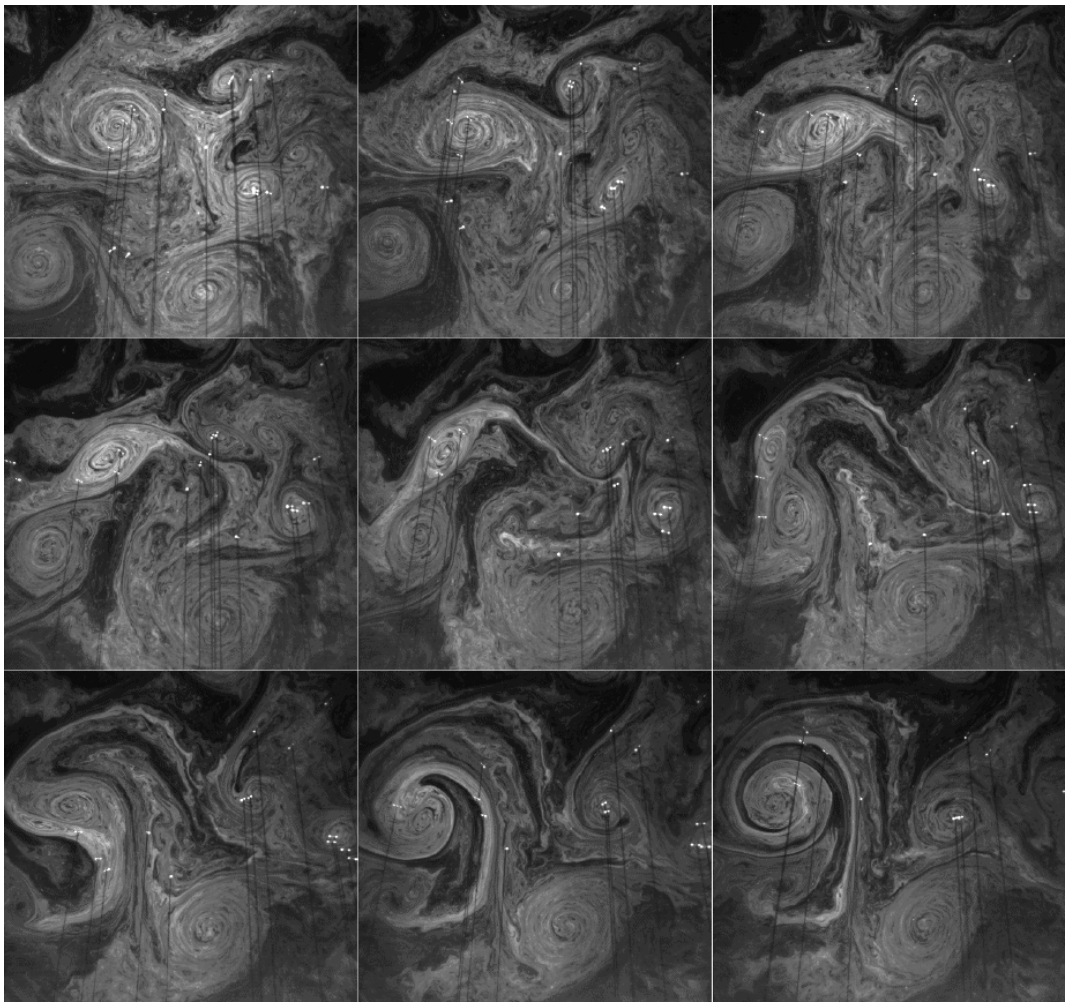

Figure 2.5: Sequence of flow visualizations obtained by LIF. Each snapshot represents the structure of the turbulent flow in a $3 \times 3\ m^2$ area placed at a few centimeters below the surface. The time interval between the snapshots is 50 *s* and the first snapshot is taken 6 *min* after the passage of the rake. In this experiment, the water depth is 90 *cm* and the rotation period is 50 *s* ($Re = 15000$ and $Ro = 1.1$). The white dots are float-like tracers, whose shadows are visible as black straight lines.

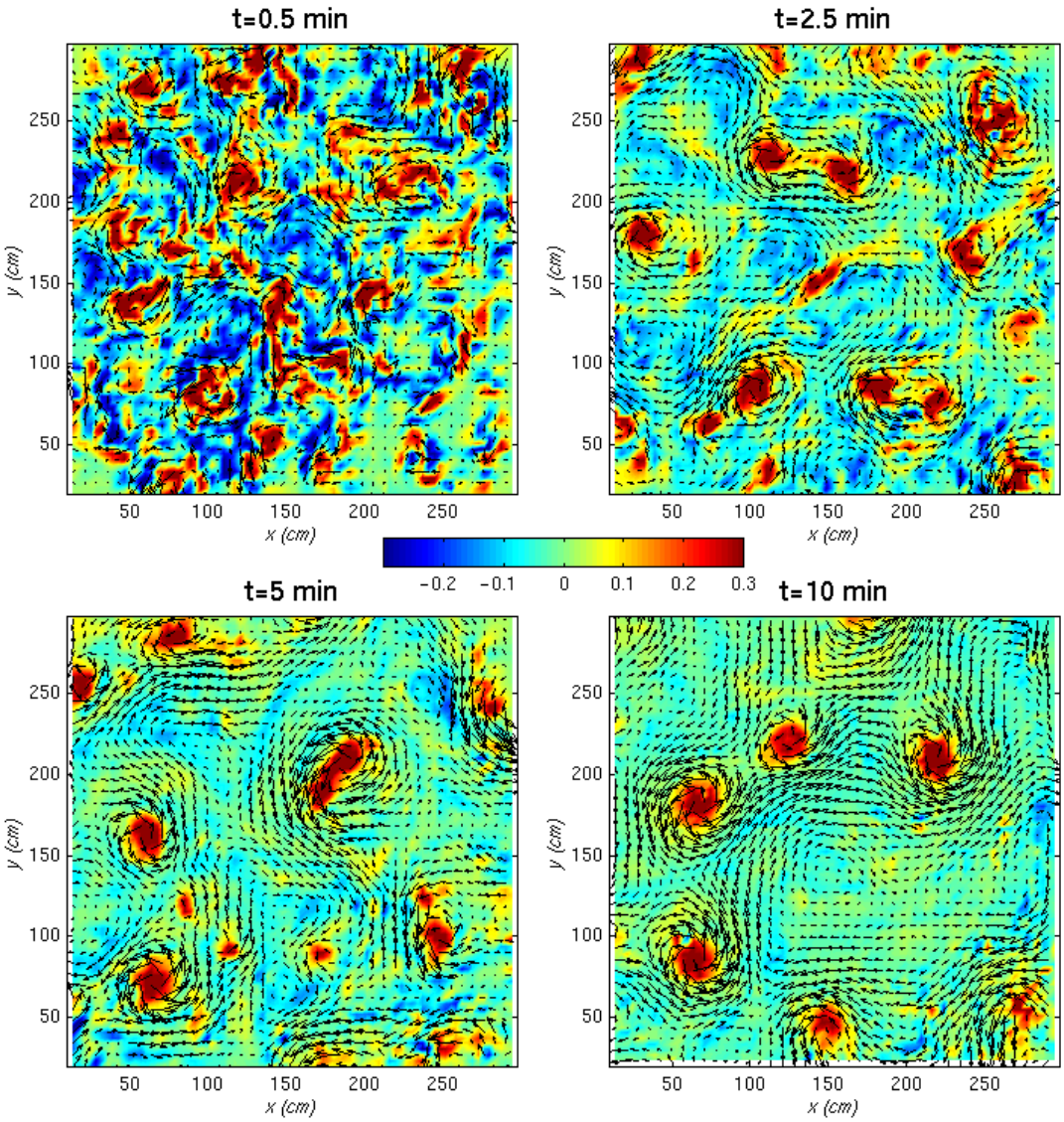

Figure 2.6: Sequence of velocity (vectors) and vorticity (color) fields obtained by PIV for an experiment with $Re = 15000$ and $Ro = 1.1$. Velocity unit is *cm/s* and vorticity unit is s^{-1}. The resolution of the fields is 3.6 *cm*, although the velocity field in figure is plotted each 7.2 *cm*. The description of the evolution of the fields is in the text.

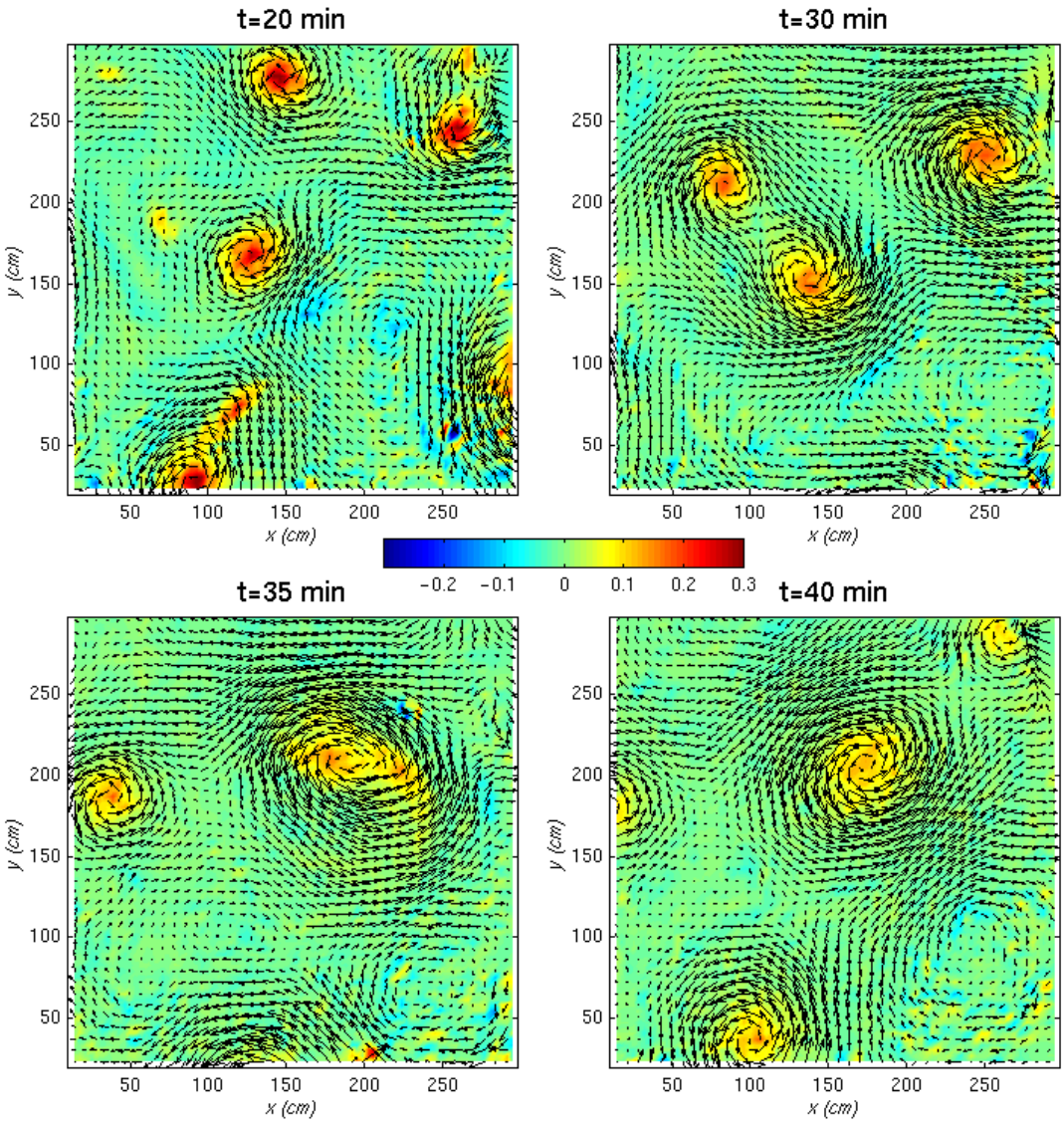

Figure 2.6: (continued)

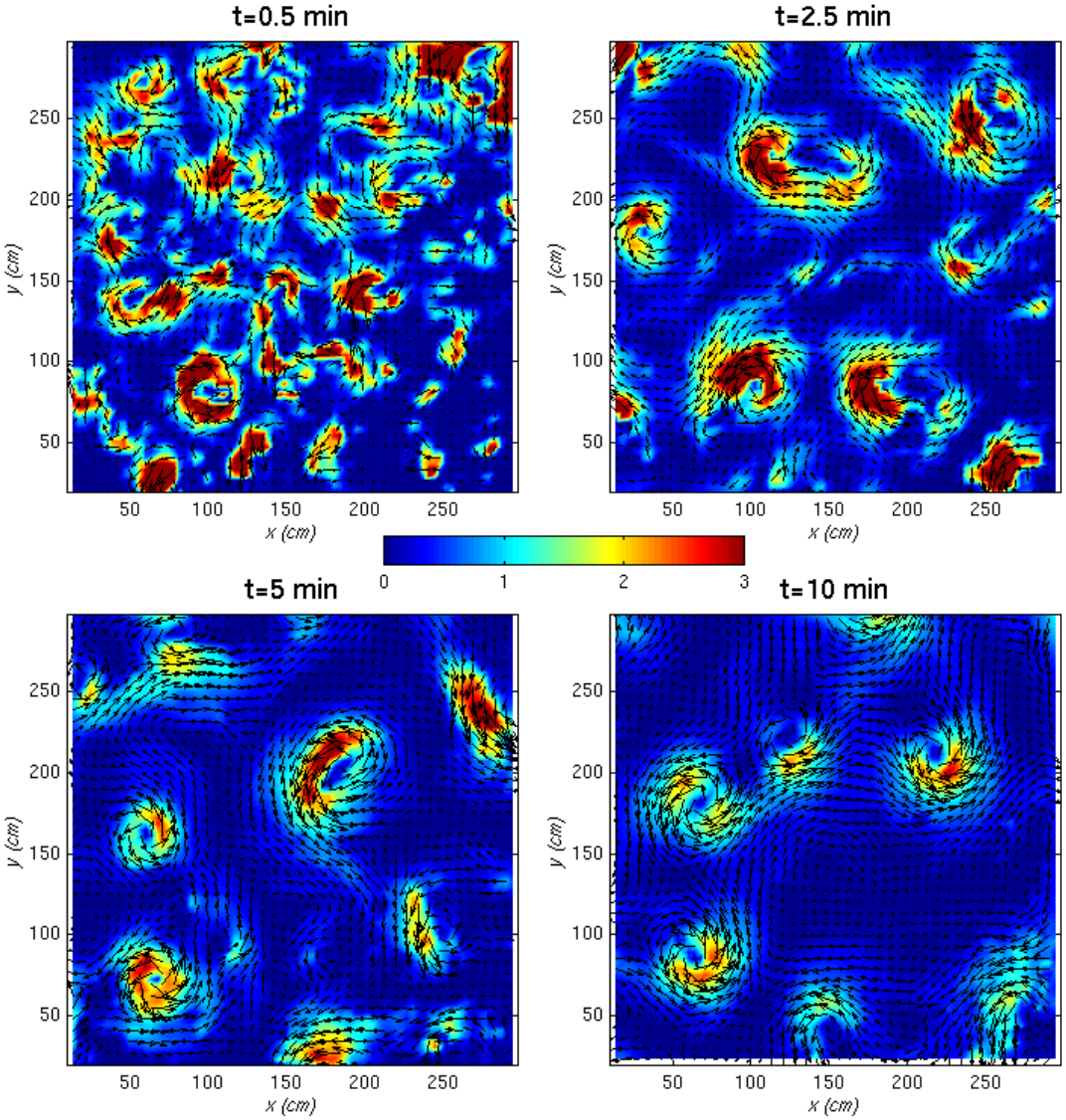

Figure 2.7: Same as in figure 2.6, but for velocity (vectors) and kinetic energy (color) fields. The unit of the kinetic energy is (cm/s^2).

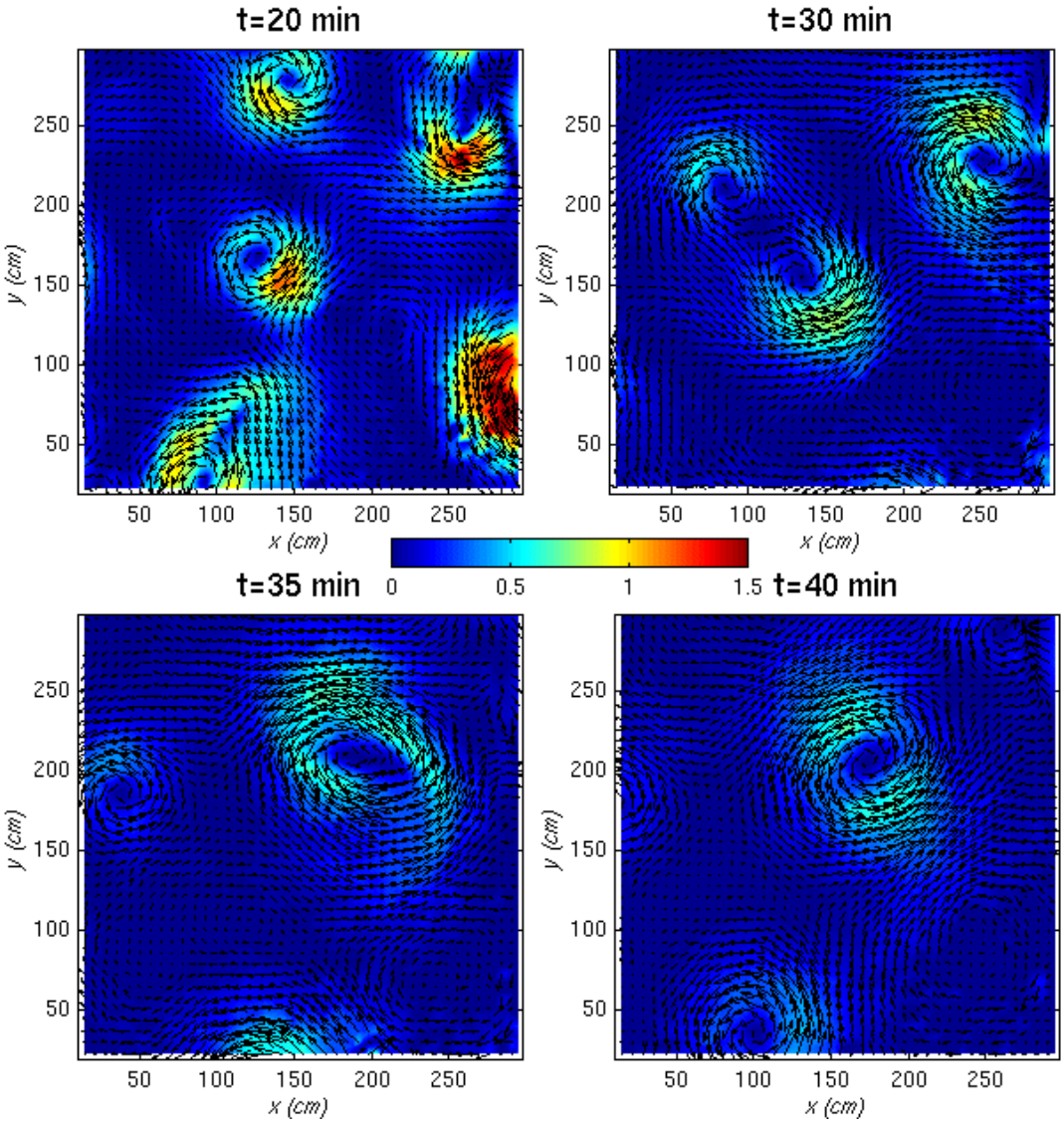

Figure 2.7: (continued)

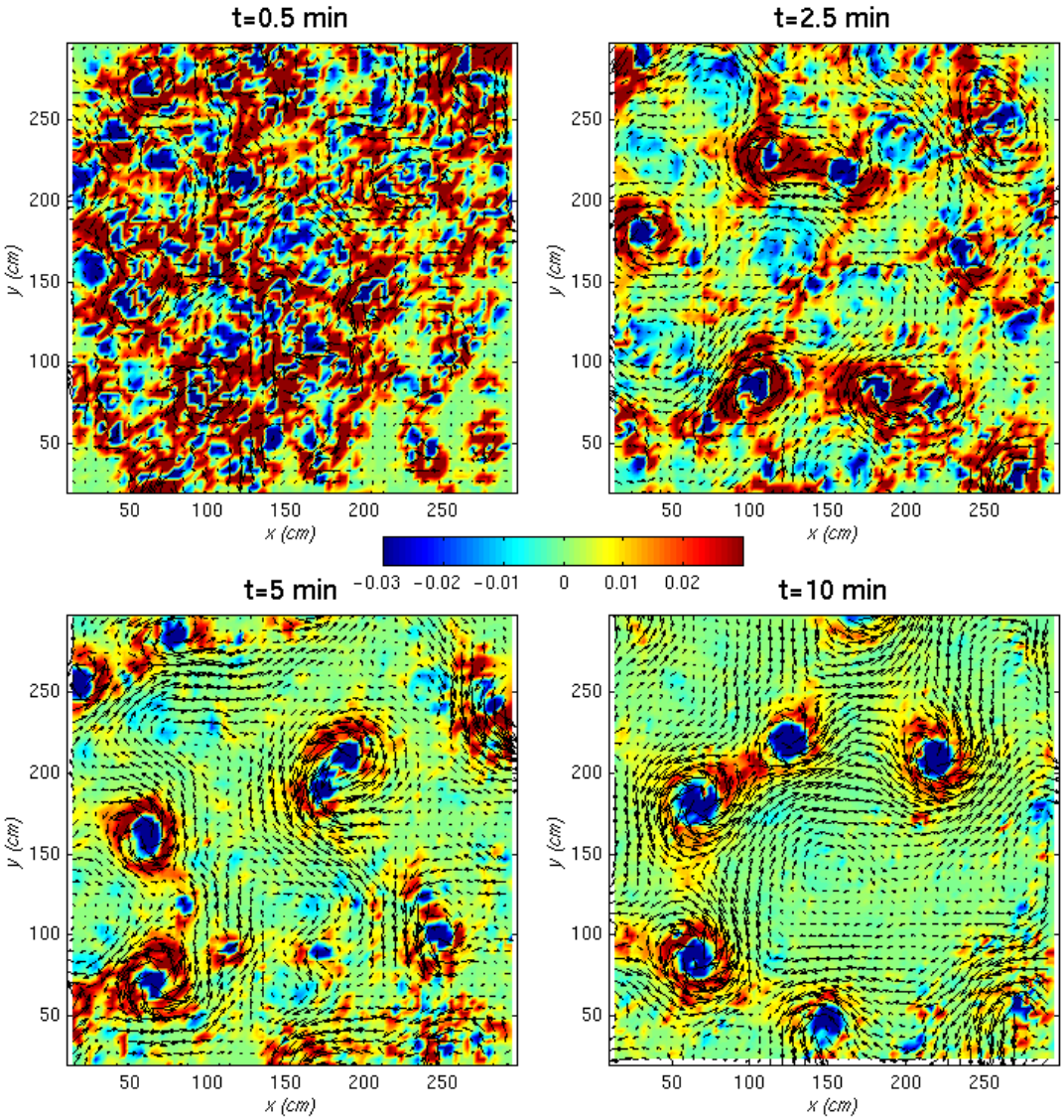

Figure 2.8: Same as in figure 2.6, but for velocity (vectors) and Q-function (color) fields. The unit of the Q -function is (s^{-2}).

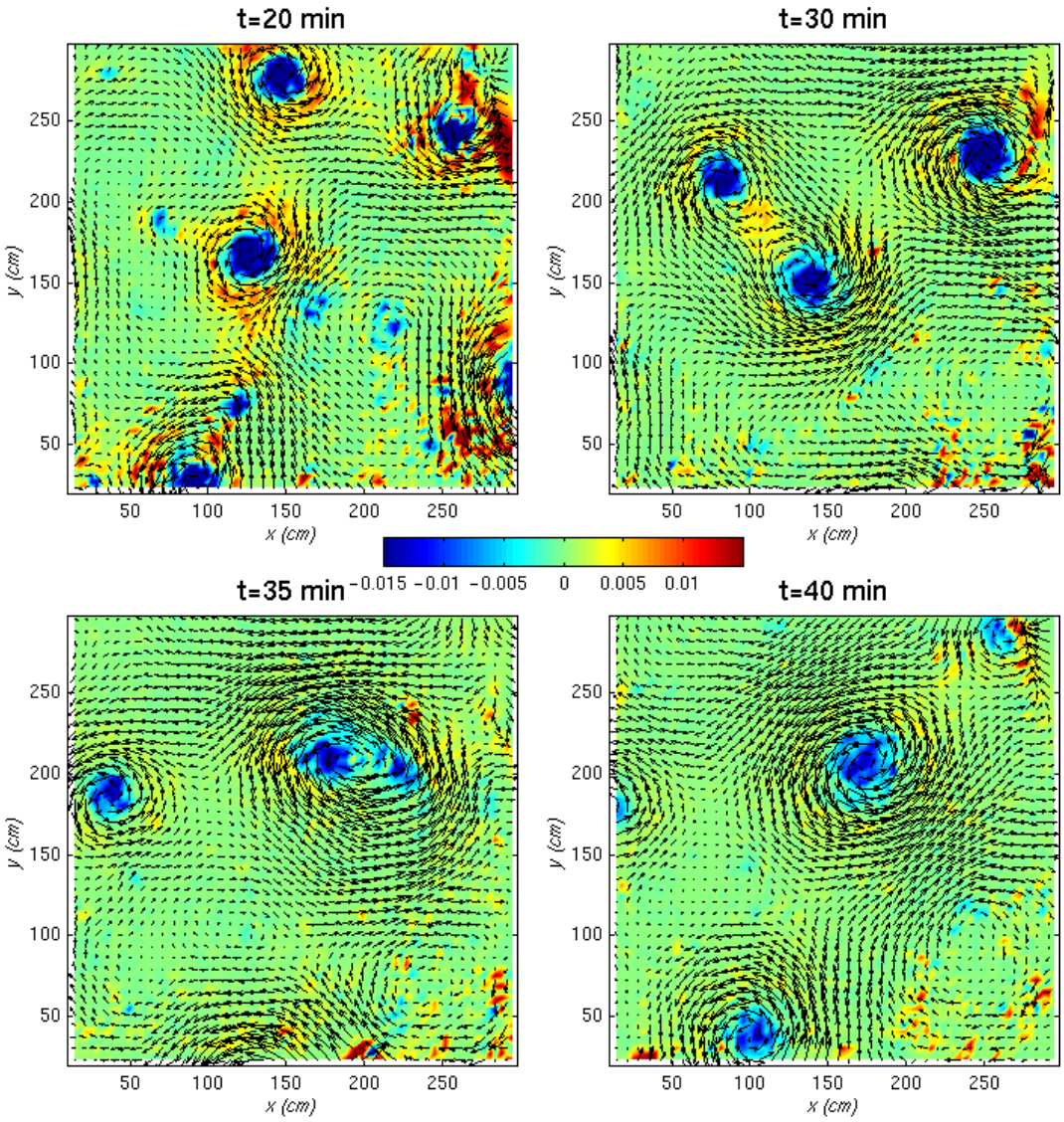

Figure 2.8: (continued)

2. $Re = 15000$ and $Ro = 2.3$, obtained by using: tank rotation period $T = 100$ *s*, rake speed $U = 6.5$ *cm/s* and rake spacing $l = 35$ cm.

3. $Re = 7000$ and $Ro = 2.3$, obtained by using: tank rotation period $T = 50$ *s*, rake speed $U = 6.5$ *cm/s* and rake spacing $l = 17.5$ cm.

4. $Re = 15000$ and $Ro = 1.1$, obtained by using: tank rotation period $T = 50$ *s*, rake speed $U = 6.5$ *cm/s* and rake spacing $l = 35$ cm.

2.4.1 Energy, enstrophy and horizontal divergence

Figures 2.9, 2.10 and 2.11 show, respectively, the time evolution of the total kinetic energy, the total enstrophy and the mean square divergence in logarithmic scale for the four cases mentioned above.

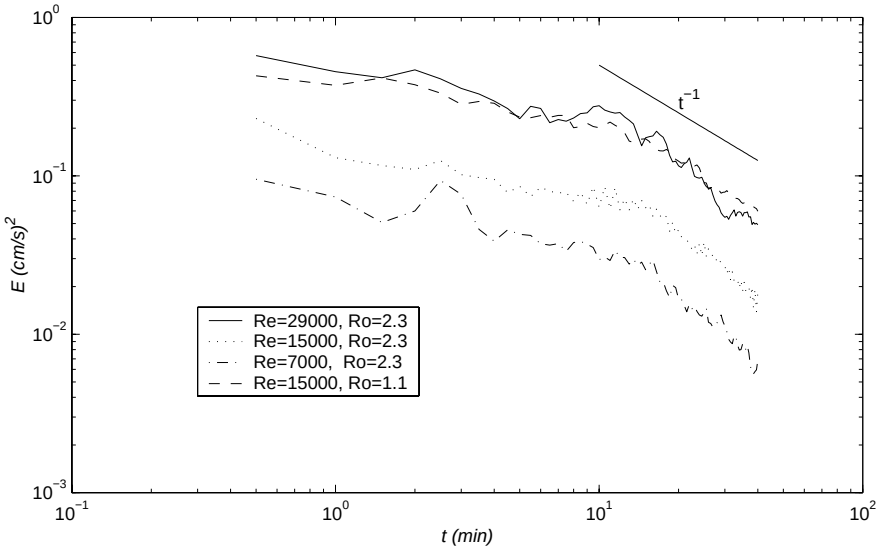

Figure 2.9: Time evolution of the total kinetic energy for four different experiments: $Re = 29000$ and $Ro = 2.3$ (solid line), $Re = 15000$ and $Ro = 2.3$ (dotted line), $Re = 7000$ and $Ro = 2.3$ (dash-dot line) $Re = 15000$ and $Ro = 1.1$ (dashed line). The straight solid line in figure is proportional to t^{-1}.

The total kinetic energy is defined by the integral over the study domain (normalized by the domain area) of the square velocity, whereas the total enstrophy is the integral of the square vorticity. Both the total kinetic energy and the total enstrophy show approximately the same behaviour for the different cases considered: after an initial slow decrease, 10 minutes after the start of the experiments the kinetic energy shows a trend proportional to t^{-1} and the enstrophy has a trend proportional to $t^{-3/2}$. The mean square horizontal divergence is proportional to t^{-1} from the beginning. Note that fast rotation ($Ro = 1.1$ with respect to the case

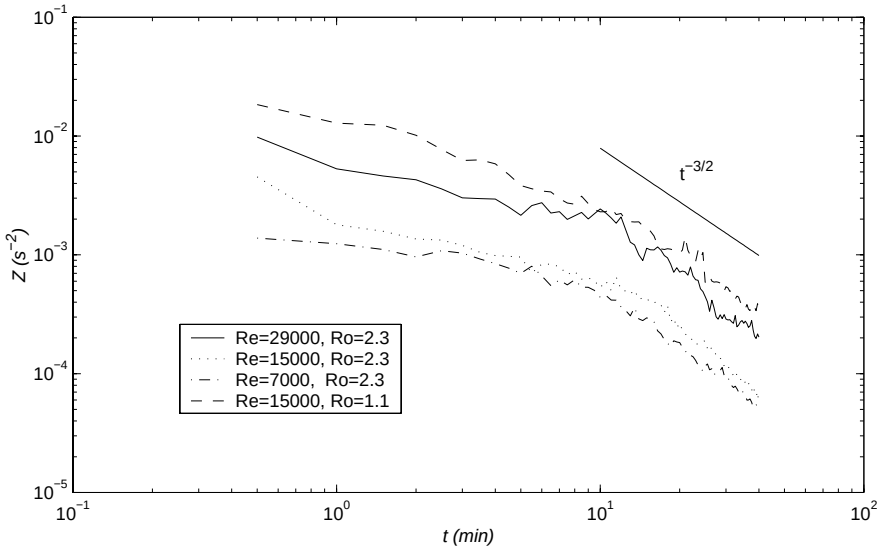

Figure 2.10: Same as in figure 2.9, but for the total enstrophy. The straight solid line in figure is proportional to $t^{-3/2}$.

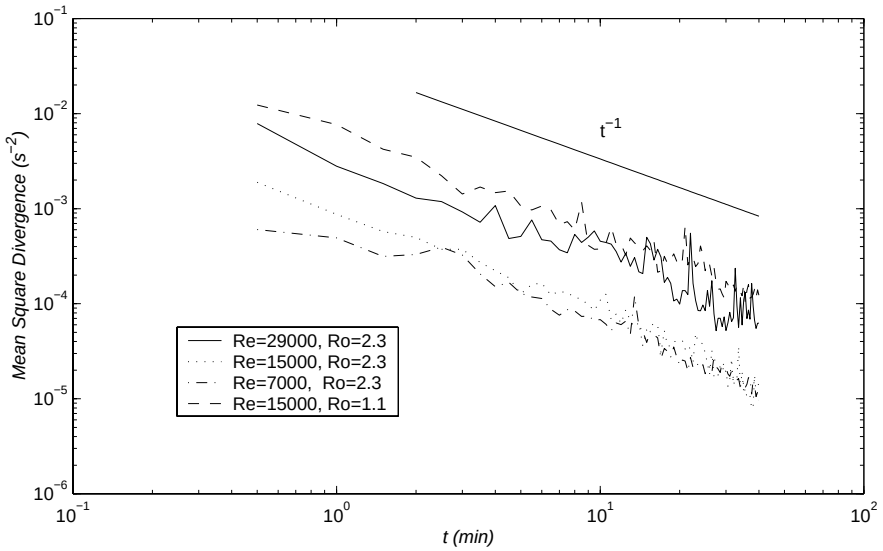

Figure 2.11: Same as in figure 2.9, but for the mean square horizontal divergence. The straight solid line in figure is proportional to t^{-1}.

with $Ro = 2.3$) increases the amount of energy and enstrophy in the system, which is also large as the Reynolds number is high.

An important indication about the quasi two-dimensionality of the system is given by the ratio between the mean square horizontal divergence and the mean

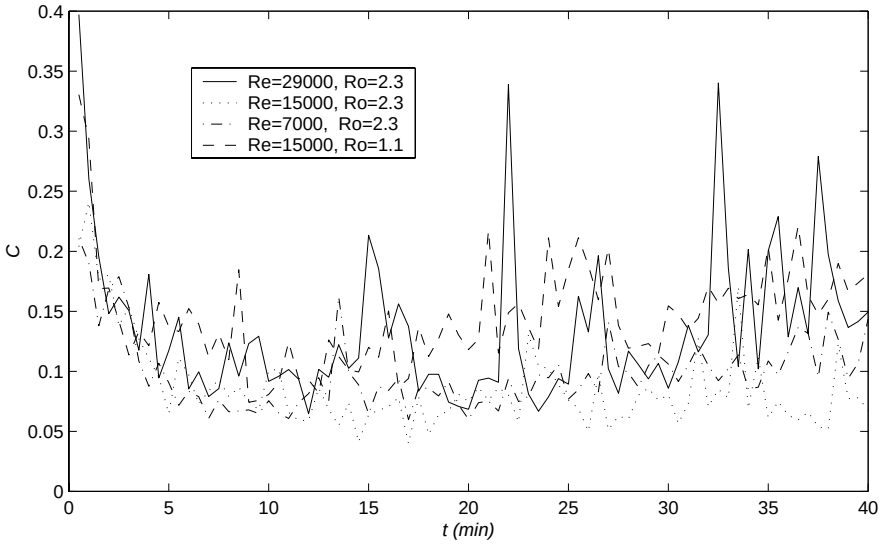

Figure 2.12: Time evolution of the ratio C between the mean square horizontal divergence and the mean enstrophy

enstrophy, which is plotted in figure 2.12. As one can see, five minutes after the arrest of the rake the square horizontal divergence is one order of magnitude lower than the mean enstrophy in all the experiments considered (both slow and fast rotation and low and high Reynolds number), providing a proof of the quasi two-dimensionality of the flow. Note that the values of the horizontal divergence can be overestimated due to the possible presence of spurious vectors in the lower part of the velocity fields, where the laser illumination of the flow is less efficient.

2.4.2 Cross-sections of kinetic energy, vorticity and Q-function in vortices

Figures 2.13-2.16 provide cross-sections of different quantities in vortices that emerge in the four cases described above. Cross-sections are given at two different times, i.e., 10 minutes and 40 minutes after the arrest of the rake.

The overall aspect of the different cross-sections is similar to what is found in numerical simulation of two-dimensional turbulence (see e.g. Elhmaidi et .al 1993). Nevertheless, differences are clear among the different experiments. High Reynolds numbers and fast rotation (small Rossby number) lead at late times to vortices that still have a high peak of vorticity and well defined profiles of kinetic energy and Q-function, as well as large sizes (up to 80 *cm* in the cases presented here).

It is clear, however, that the vorticity peak decreases as time goes on, and reduces more than one half. Another characteristic that can be seen in the figures (but also in the Q-value fields at late time in figure 2.8) is that there is no a clear

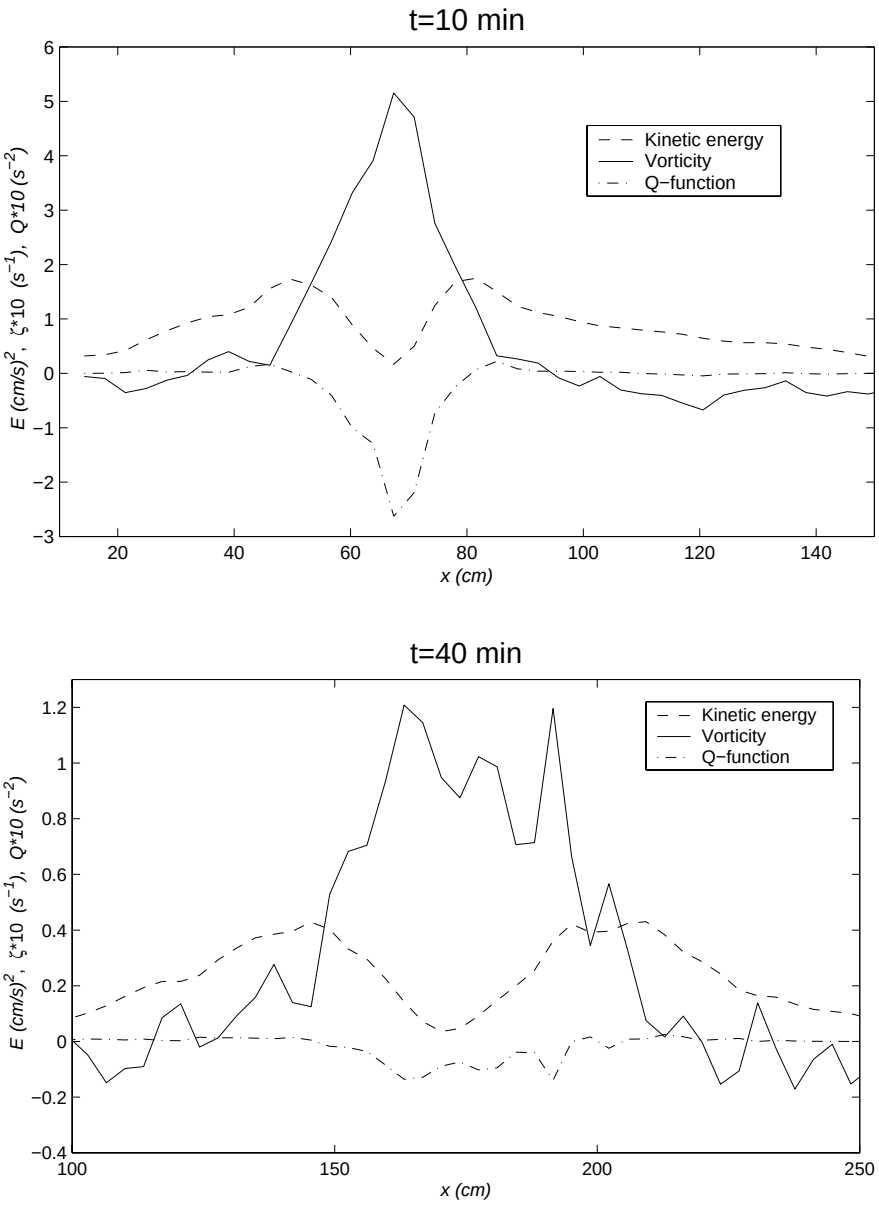

Figure 2.13: Cross-sections of vorticity (solid line), kinetic energy (dashed line) and Q-function (dash dot line) in a vortex at two different times for the experiment with $Re = 15000$ and $Ro = 1.1$. Note that the values of kinetic energy and Q-function are multiplied by 10.

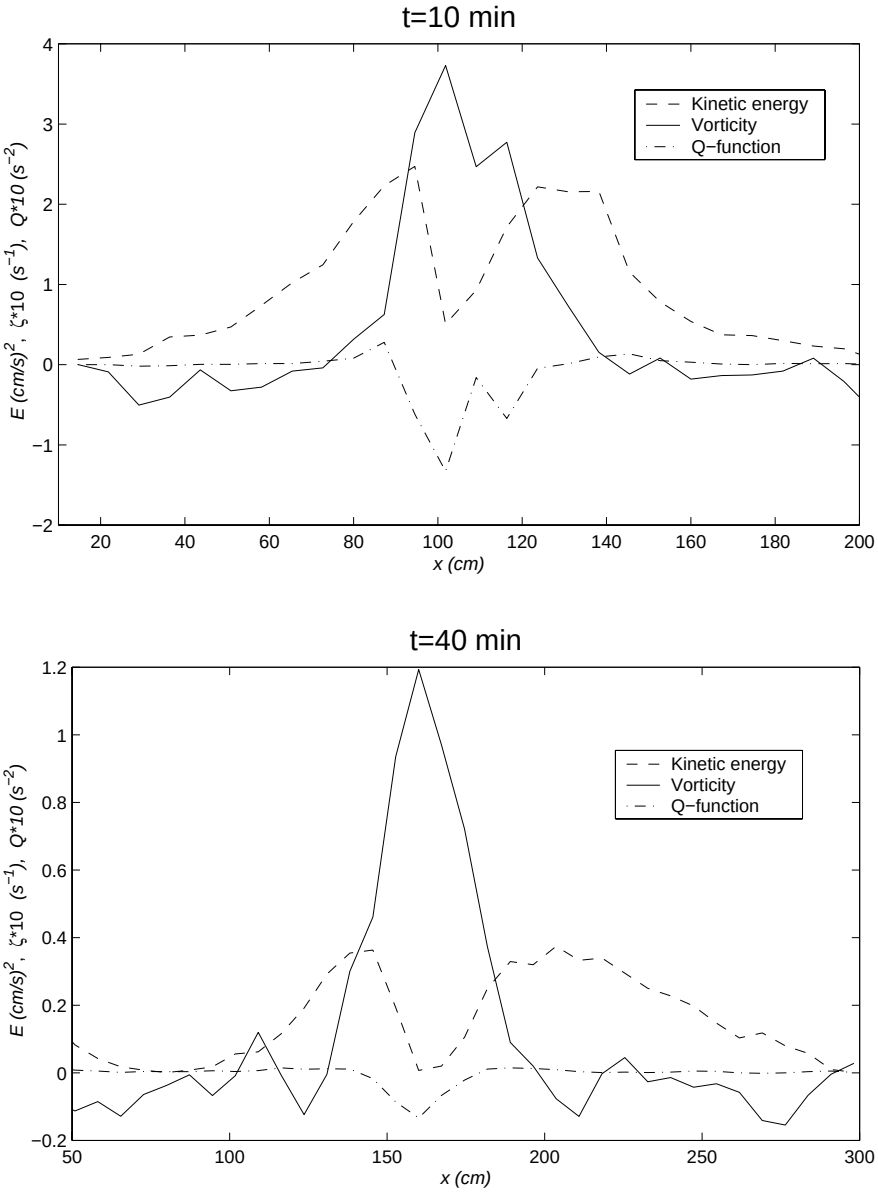

Figure 2.14: Same as in figure 2.13 for the experiment with $Re = 29000$ and $Ro = 2.3$

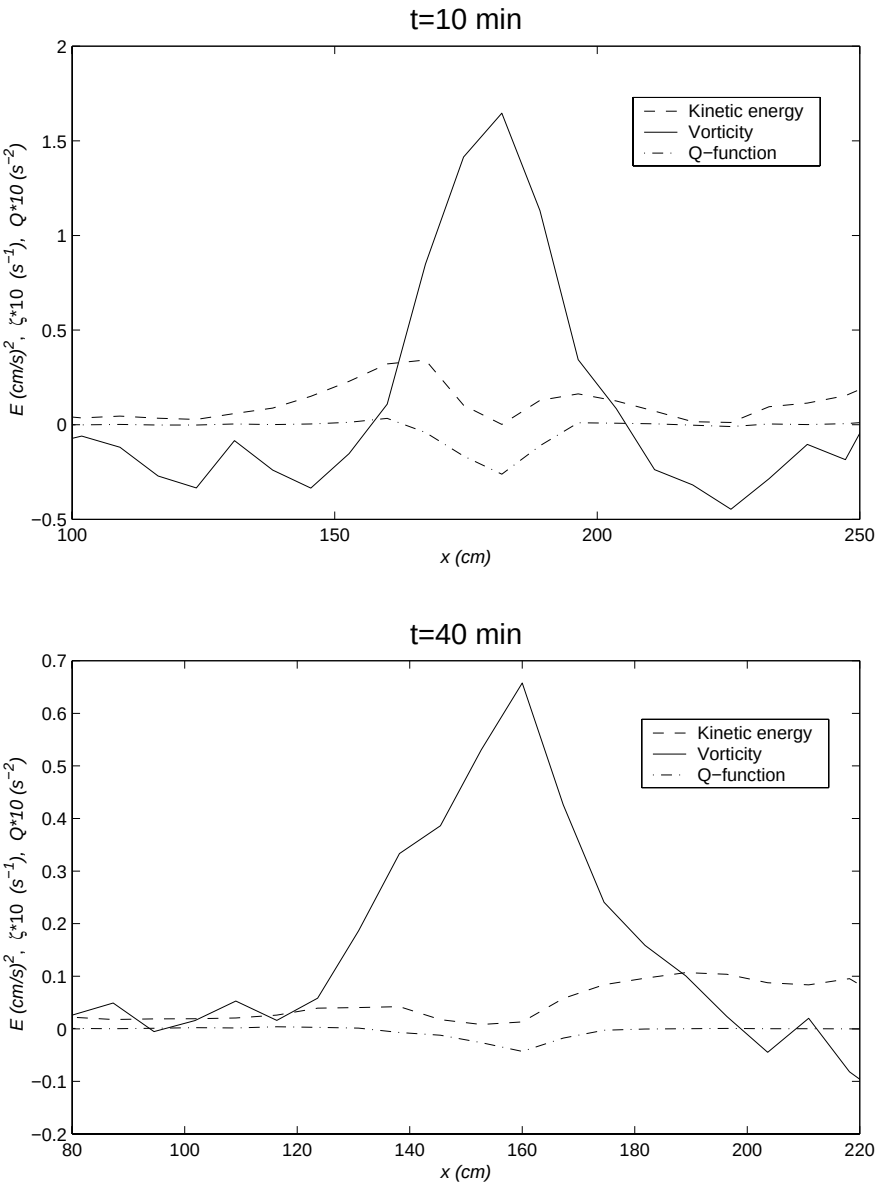

Figure 2.15: Same as in figure 2.13 for the experiment with $Re = 15000$ and $Ro = 2.3$

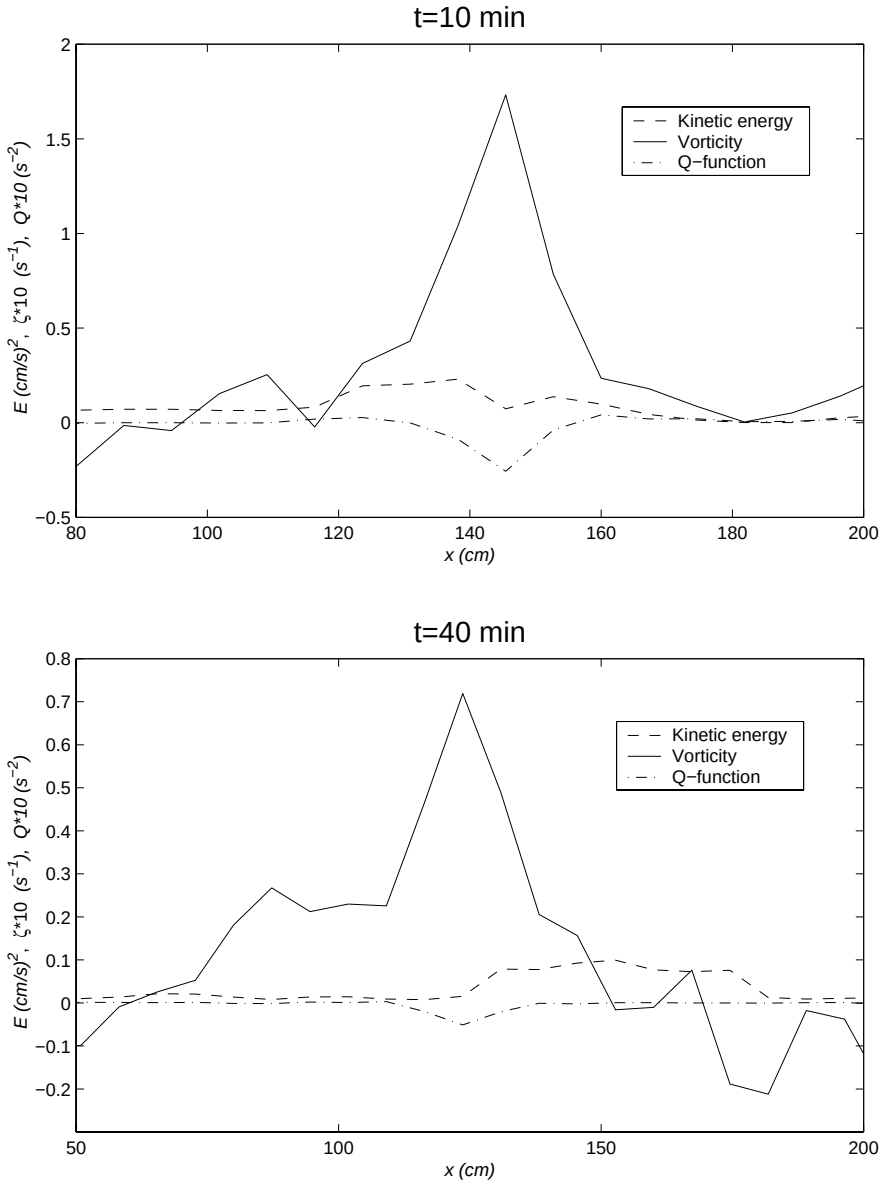

Figure 2.16: Same as in figure 2.13 for the experiment with $Re = 7000$ and $Ro = 2.3$

circulation cell around the vortices, in all the cases discussed here (above all at late times, there are no rings of high positive Q around vortex cores with high negative Q-values). The strain field around the vortex cores, therefore, seems to be weak in comparison with numerical simulations of two-dimensional turbulence. This might have an effect on the dispersion laws of passive tracers in quasi two-dimensional turbulence, as *anomalous dispersion* is often related to the presence of circulation cells around vortex cores (see section 3.1).

Chapter 3

Transport of passive tracers by coherent vortices: a laboratory view

Lagrangian dynamics of passive tracers and transport by coherent vortices in laboratory experiments is the central topic of this chapter. Tracers consist both in float-like tracers seeded in the fluid and numerical tracers whose trajectories are obtained by integration of the Lagrangian equation of motion, by means of a pseudo-experimental technique that uses experimental Eulerian fields as input data. Trapping of passive tracers in vortex cores and the impermeability of vortex edge to inward fluxes of tracers are discussed.

3.1 Numerical background on transport by coherent barotropic vortices

Coherent vortices have been studied numerically from both the Eulerian and the Lagrangian points of view. The Lagrangian approach is used to examine the transport properties of passive scalars and/or passive tracers[1] in turbulent flows characterized by the presence of fully-developed vortices. In particular, coherent vortices have been shown to be very efficient in trapping passive tracers for long times and transporting them over large distances (Elhmaidi et al. 1993, Babiano et al. 1994, Paparella et al. 1997). Furthermore, vortices show a strong impermeability to inward fluxes of particles, due to the strong gradient of vorticity at their edges (McIntyre 1989).

Figure 3.1 shows these key properties of vortices. In panel (a), two ensembles of passive tracers are seeded inside a two-dimensional, freely decaying, turbulent vorticity field, whose initial conditions are the same as in figure 1.3a; 1800 yellow tracers are seeded inside the core of an anticyclonic vortex, whereas 1800 green tracers are seeded in the turbulent background. After a long time, compared to the eddy turnover time, the evolved distribution of particles in panel (b) shows that particles seeded in the vortex remained there during the turbulent evolution, whereas particles seeded in the background spread throughout the field without entering any vortex.

Coherent vortices act as "islands" of regular motions, in contrast with the Lagrangian chaoticity which characterizes the turbulent background (Babiano et al. 1994), and passive tracers display an almost null radial relative dispersion[2] and a linear azimuthal dispersion in vortex cores (Provenzale et al. 1999). This is shown in figure 3.2, which represents a zoom of an anticyclone in the field shown in figure 3.1, seeded with passive tracers placed on a radial line. After a (nondimensional) time $T = 13$, almost no radial dispersion is evident, while one can see azimuthal dispersion due to the differential rotation inside the vortex core. Two radially nearby particles, therefore, undergo circular motions around the vortex centre, lying almost always on the same orbits, but with slight different azimuthal velocities.

Numerical simulations have also pointed at the presence of coherent vortices (and, in particular, of the circulation cells around vortex cores) to interpret the *anomalous dispersion* regime at intermediate times, which has been found in the absolute dispersion[3] curves in two-dimensional turbulence, which is neither bal-

[1] An advected scalar is a general scalar entity, such as the concentration of dye, which satisfies an advection-diffusion equation. Tracers, on the other hand, are individual particles, ideally point-like and massless, whose equation of motion is given by the equivalence between the Lagrangian and the Eulerian velocities at the tracer positions. They are also called *Lagrangian tracers* or *Lagrangian particles*. The attribute "passive" means that the dynamics of the scalars or of the tracers does not influence the dynamics of the flow

[2] Relative dispersion is defined as the mean square displacement at time *t* between a pair of initially nearby particles.

[3] Absolute dispersion (also called single-particle dispersion), $A^2(t, t_0)$, provides a measure of

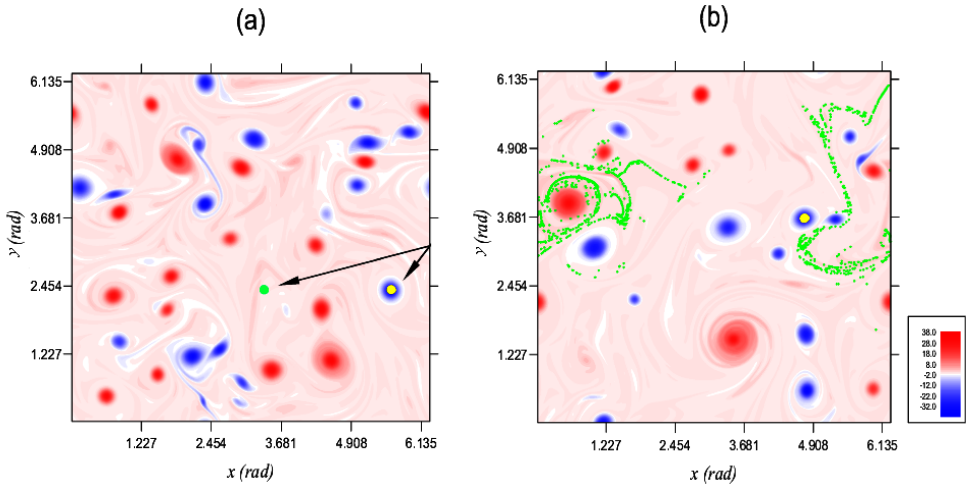

Figure 3.1: Two ensembles of passive tracers are seeded in a freely decaying, 2D turbulent field with fully-developed vortices: 1800 yellow tracers are seeded inside the core of an anticyclonic vortex, while 1800 green tracers are seeded in the turbulent background (panel a). The evolved distribution in panel (b), after a (nondimensional) time $T = 13$, shows that vortex core are able to trap passive particles for a long time, compared to the eddy turnover time, and are impermeable to inward fluxes of particles from the background. The numerical simulation is performed in a doubly periodic square domain with size 2π and using a time step $dt = 10^{-3}$. The initial conditions for the vorticity field are the same as in figure 1.3a.

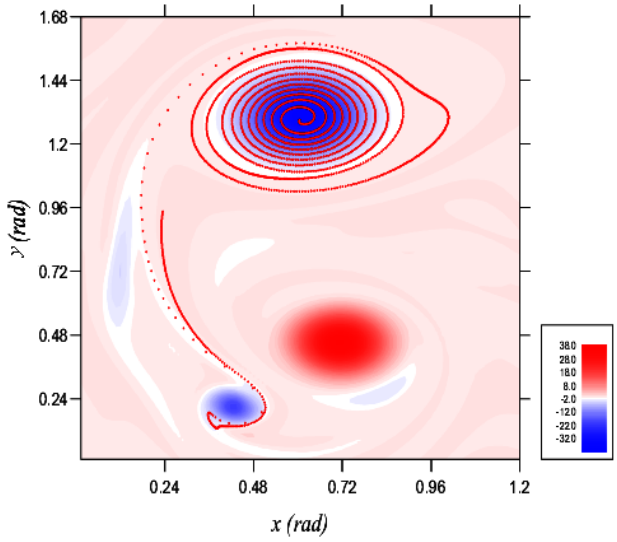

Figure 3.2: Zoom of an anticyclonic vortex in the vorticity field shown in figure 3.1b. The vortex is initially seeded with passive particles placed on a radial line. After a (nondimensional) time $T = 13$, tracers inside the core show almost no radial dispersion but only azimuthal dispersion due to the differential rotation.

the mean square displacement of individual particles at a certain time *t*, as function of their initial positions at time t_0. The average is calculated over the particle ensemble.

listic ($A^2(t) \propto t^2$) nor Brownian ($A^2(t) \propto t$), but is characterized by a trend $A^2(t) \propto t^{5/4}$ (Elhmaidi et al. 1993).

3.2 Experimental Lagrangian data

The experiments carried out in the "Coriolis" rotating tank have also the purpose of verifing some properties of transport by coherent vortices from the laboratory point of view. In order to do this, together with the Eulerian data provided by the PIV technique, we have collected Lagrangian data provided by both float-like tracers (direct Lagrangian data) and numerical tracers whose trajectories are obtained by integration of the equation of motion by using the experimental velocity fields (indirect Lagrangian data).

Float-like tracers are composed by a buoyant stick and an approximately ellipsoidal container in the lower part (the "balloon"), see figure 3.2. Iron pellets are placed inside the balloon, in order to equilibrate the float at a certain depth. We used floats with balloons at 20 *cm* depth. The particular shape of these floats avoids "sticking effects" due to surface tension. The floats are furnished with a fluorescent upper bright stick to visualize their path and to record their positions by the camera. The frame rate acquisition is in this case higher than for PIV, up to one frame every 5 seconds, but necessarily the total acquisition time is shorter (up to 15 minutes).

Although the size of these tracers is not negligible, they can provide important qualitative information on particle transport. Their inertia, as pointed out in the last chapter, is important above all in a short, initial transient of time after they are released in the fluid (with null initial velocity); afterwards, their dynamics approaches the dynamics of Lagrangian tracers, except for small scale motions (large wave numbers) or high frequency motions that are filtered out. The experiments performed in the large-scale "Coriolis" tank deal with properties of the turbulent flow at small wave numbers and low frequencies, and the tracers we use are able to catch much of the dynamics in the interesting range.

Float-like tracers are used above all in combination with LIF technique, when coherent structure are well recognized; they cannot be used in combination with Particle Image Velocimetry, because of the possible shadow effects that arise when the stick or the balloon below the water surface crosses the laser sheet. The vortices or the turbulent background are seeded with these tracers (we have used up to 25 tracers in each experiment) with the aim of studing the impermeability properties of coherent structures.

Because of the technical difficulties to obtain long sequences of many Lagrangian tracer trajectories with high sampling frequency in a large-scale experiment, the technique we use to obtain trajectories of passive tracers is pseudo-experimental. The idea is to use the time sequences of the Eulerian velocity fields provided by PIV, interpolated in time and space in order to obtain high frequency and large wavenumber samples, and to integrate numerically the equation of mo-

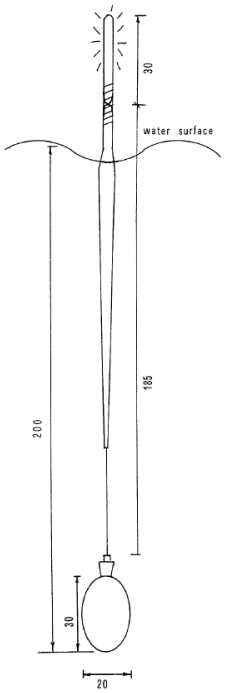

Figure 3.3: Sketch of a float-like tracer used as a Lagrangian tracer. See description in the text. In the figure, units are in millimeters.

tion for Lagragian tracers:

$$\frac{d\mathbf{X}}{dt} = \mathbf{u}(X, Y, t), \tag{3.1}$$

where $\mathbf{u}$ is the experimental velocity interpolated in the position $\mathbf{X} = (X, Y)$ of the numerical tracer.

This technique is often used to extract Lagrangian data from meteorological wind field, by interpolating in space and time the Eulerian data provided every six-twelve hours over a certain region (see Paparella et al. 1997 for a geophysical application of this technique to the Antarctic polar vortex). One of the crucial point for the use of this technique is the temporal resolution of the sequence of the velocity fields. The experimental, original sampling has been limited to a frequency of 1/30 *Hz*, due to data storage problems occurring for very long sequences. This temporal resolution is not sufficient for smooth integration of equation (3.1). The criterium I use in order to evaluate the requested temporal resolution is an equivalent of the *Courant-Friedrichs-Lewy* (CFL) stability criterium: the minimum sampling frequency that is requested for a certain experiment is given by:

$$\frac{1}{\delta t} \geq \frac{|u|}{\Delta x}, \tag{3.2}$$

where u is the maximum value of the velocity components and Δx is the grid spacing. This criterium ensures that the position of each tracer does not change

more than a grid step during every time step. For the experiments described here, having a grid resolution of 3.6 *cm*, $\delta t = 1$ *s* has been determined as a sufficient temporal resolution.

Both the temporal and the spatial interpolation is performed by using a spline algorithm, respectively cubic and bicubic. The reason for this choice lies in the smoothness of the interpolating spline function, which is also smooth in the first derivative (gradients). The time integration of the equation of motion for Lagrangian tracers is performed by using a third-order Adams-Bashford scheme.

Both for direct and for indirect Lagrangian data, one big problem is given by the lack of boundaries in the camera view field. This means that tracers can easily and rapidly get out of the view field, making very difficult the evaluation of late time statistics, such as absolute dispersion or maximum Lyapunov exponent. On the other hand, the distance of the camera view field from the channel walls assures that boundary effects can be neglected.

3.3 Laboratory results on transport by barotropic vortices

The results discussed in this section and in the following of the chapter concern some experiments performed with fast tank rotation (period of $T = 50$ *s*), medium rake speed ($U = 6.5$ *cm/s*) and coarse rake spacing (35 *cm*). This conditions correspond to an initial Rossby number $Ro = 1.1$ and an initial Reynolds number $Re = 15000$. Together with the creation of initial turbulence by means of the rake, some results obtained by using the cylinder are also discussed.

3.3.1 Impermeability to inward and outward tracer fluxes

The experiments we have carried out in freely-decaying turbulent flows confirm that coherent vortices have a strong capability of trapping passive tracers for long times, much longer than the eddy turnover time and comparable with the vortex life-time. Release of tracers trapped inside a vortex occurs during vortex-vortex interactions, above all during merging processes (see next section).

Figures 3.4, 3.5 and 3.6 show pictures of vortices seeded with either fluorescein or with the microscopic particles used for the PIV. The vortex in figure 3.6 is generated (inside a background turbulence obtained by means of the rake) by stirring the water inside a cylinder lowered into the channel at a pre-selected position, as explained in section 2.2. Due to the zero mean circulation into the flow, this method does not yield, generally, a monopolar vortex, but rather a tripole, at least at late times.

Trapping and impermeability are evident in figure 3.4, where the core of the anticyclone in the dipole is seeded with PIV particles (blue bright colour) and the cyclone is unseeded. Fluorescein is seeded in the background (green colour). The core of the cyclone remains devoid of fluorescein. This latter does not enter the

vortex except for molecular diffusion at late times. A similar situation is depicted in figure 3.5, where fluorescein is released inside the large vortex on the right, whereas PIV particles are released in the two smaller vortices. Even if the two smaller vortices are in the process of merging, there is no exchange of material between the two cores at this stage. Trapping and regular motion of PIV and float-like tracers are evident in figure 3.6, where tracers are released in an artificially created vortex which, at this early stage, shows the onset of instabilities at the edge.

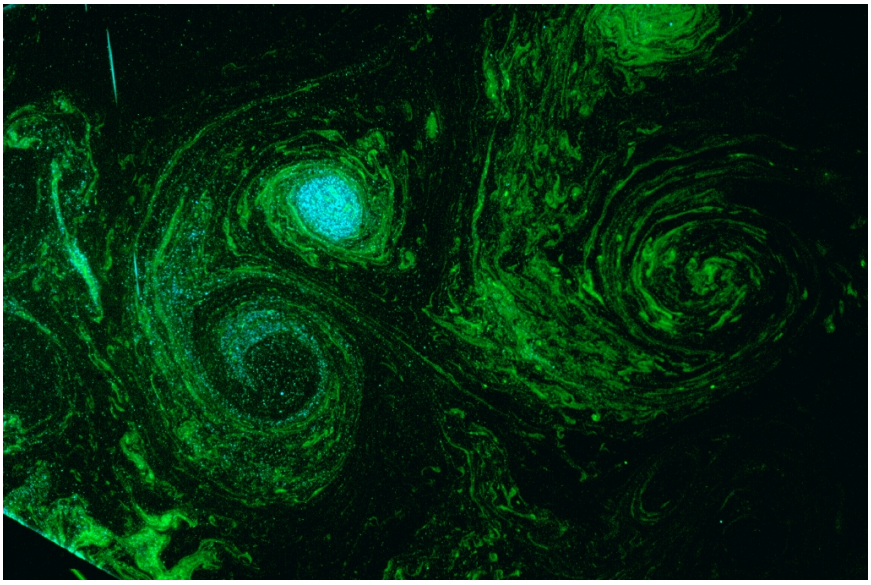

Figure 3.4: A picture of a dipole, where the core of the anticyclone has been seeded with PIV particles and the cyclone is unseeded. Fluorescein is seeded between vortices. The core of the cyclone remains devoid of fluorescein. Photo: A. Provenzale.

The fact that tracers seeded inside coherent vortices are trapped for long times is also evident in figure 2.5 shown in chapter 2, where float-like tracers are represented by white points. Thus, one can observe that strong tracer trapping takes place in non-merging vortex cores, and this is associated with a well-defined impermeability of the vortex edge to inward and outward tracer fluxes.

The results of the observations are also confirmed by means of the pseudo-experimental Lagrangian technique. Figures 3.7a and 3.7b show the initial release of two patches of passive tracers and their evolved distribution at later time. A total of 1800 tracers (red) are released inside a cyclonic vortex which does not interact much with the others during the evolution of the turbulent field, whereas 1800 (black) tracers are released into the background. As shown in figure 3.1 for a numerical simulation, also in laboratory experiments the patch in the vortex core is trapped for many rotation periods, whereas the patch in the background is stretched and spread throughout the turbulent field, without entering any vortex.

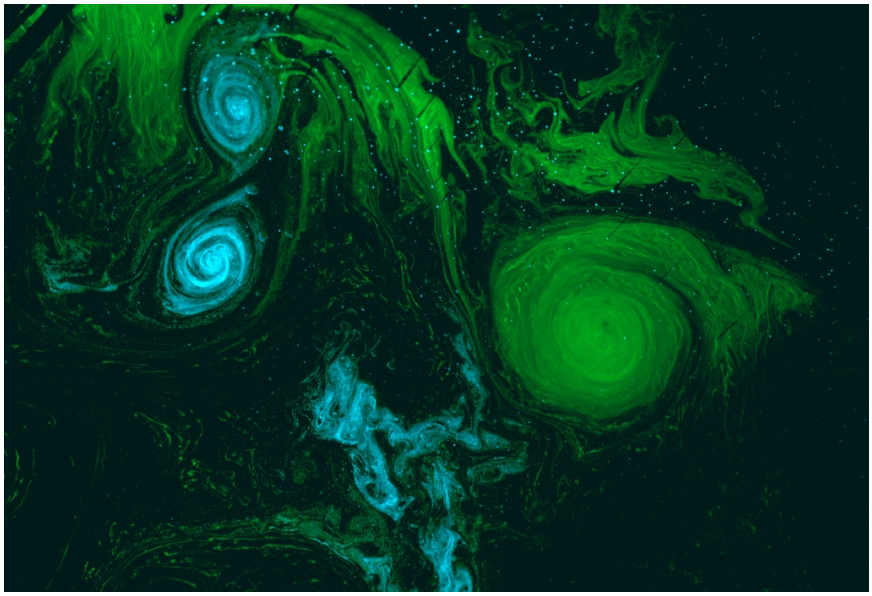

Figure 3.5: This picture shows three vortices. Fluorescein is released inside the large vortex on the right, whereas particles are released in the two small vortices. The background is contaminated with both fluorescein and PIV particles. No exchange of fluid occurs between the cores of the two smaller vortices, even if they are in the process of merging. Photo: A. Provenzale.

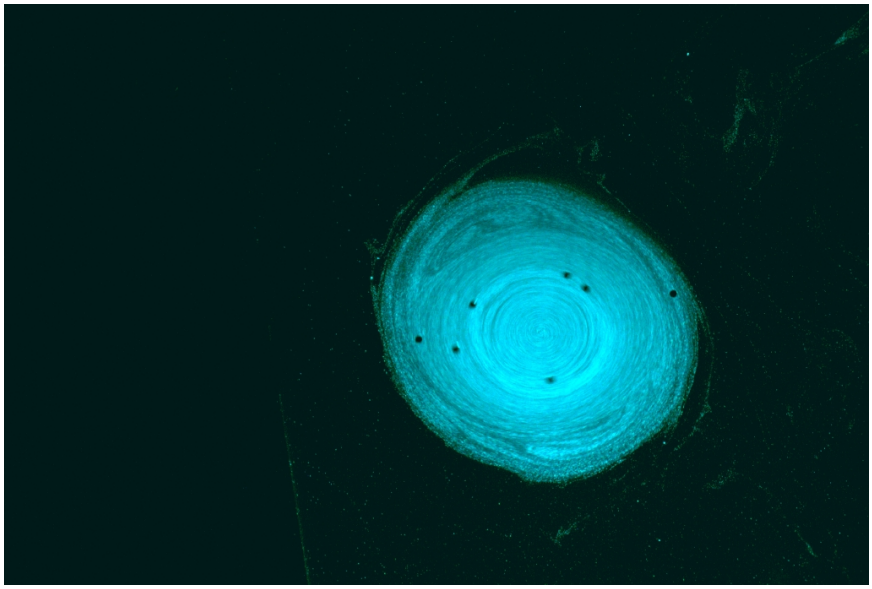

Figure 3.6: A picture of a monopolar vortex that has been created by using the cylinder with rotating blades. The tracers inside the vortex core (particles and float-like tracers) display a regular motion around the center. Photo: A. Provenzale.

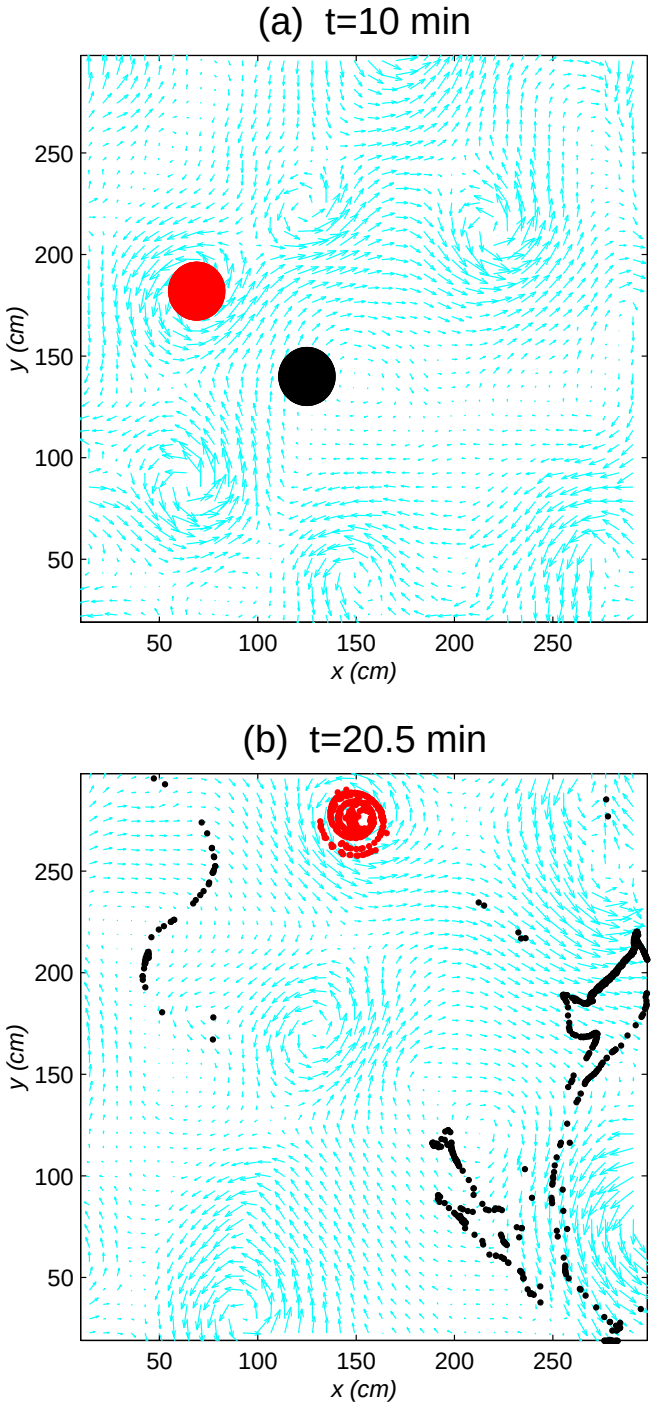

Figure 3.7: In this figure, the initial distribution (a) and the evolved distribution (b) of 3600 passive numerical tracers seeded inside experimental velocity fields are presented. 1800 (red) tracers are seeded in a cyclonic vortex core and 1800 (black) in the turbulent background. The evolved distribution is characterized by trapping of red tracers and spreading of black tracers throughout the turbulent field, except for vortex cores. The flow in the figure has an initial Rossby number $Ro = 1.1$ and an initial Reynolds number $Re = 15000$. The times indicated in figure are evaluated since the arrest of the rake.

3.3.2 Regular motion inside vortex cores

As already shown in some previous figure, the motion of passive tracers inside vortex cores is characterized by regular, circular trajectories around the centre (figure 3.8 shows a typical trajectory in a cyclone), in contrast with the chaotic nature of trajectories in the turbulent background.

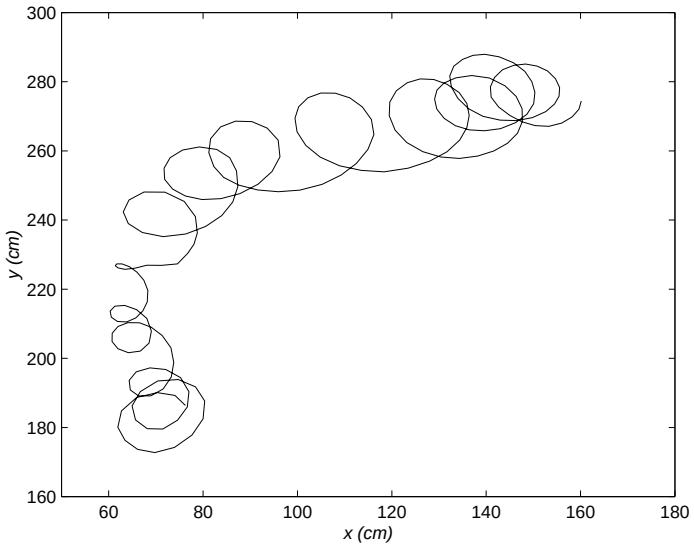

Figure 3.8: A typical trajectory of a passive tracer inside a vortex core, obtained by means of the pseudo-experimental technique.

Regular motion of float-like tracers inside a cyclonic core can be appreciated in the time sequence of figure 3.9. This figure is a zoom of the upper left vortex in the sequence of LIF images in figure 2.5, much before the merging process that it finally participates in. Tracers (white double points) are released inside the core and, apart for drift effects during an initial transient, they undergo regular trajectories around the center; differential rotation in the vortex allows for a larger speed of the most external tracers.

The azimuthal dispersion which characterizes tracers inside a vortex core is better shown by reproducing the same initial distribution of tracers as in figure 3.2, i.e., a radial line starting from the vortex centre. By means of the pseudo-experimental Lagrangian technique, a beautiful spiral of tracers is obtained after some time (three minutes after the release), which also confirms the almost null radial dispersion of passive particles inside vortices.

3.4 A Lagrangian view of vortex merging

One of the most impressive processes that one can watch when visualizing a turbulent field with fluorescein is, in my opinion, the merging of two same-sign vortices.

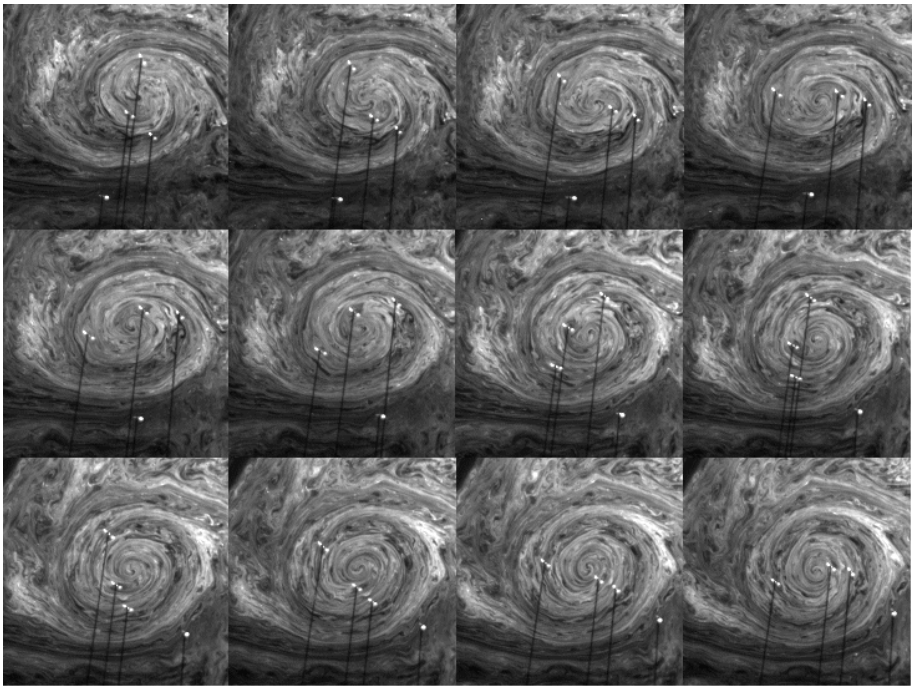

Figure 3.9: This figure is composed by a sequence of frames taken every 5 seconds. It shows (during a time interval of 55 *s*, which corresponds approximately to the eddy turnover time for the present experiment) the evolution of a cyclone and the deplacements of some float-like tracers seeded into the vortex core. The double bright point is an effect of the laser illumination; the shadows indicate the tracer positions. Regular trajectories inside the core are displayed by the motion of the tracers.

One of these episodes is depicted in the sequence of figure 3.11 by using the LIF technique, another is represented in figure 3.12 by using the pseudo-experimental Lagrangian technique. Both of these visualizations, however, do not render entirely the speed of the process, which can be appreciated only by means of an animation (otherwise, during a real experiment).

As shown in chapter 2, merging of vortices is the best way to increase vortex size and to reduce vortex number. Although merging occurs only when two vortices are close enough to each other, there is a large time interval during which advection of vortices by the turbulent field and the large number of coherent structures make this process very common. From the Eulerian point of view, merging is characterized by an initial interaction of two same-sign vortices which start to exchange material from their edges. A fast circling motion of one vortex around the other occurs afterwards, up to the complete coalescence of the two structures.

A Lagrangian view of the process is provided by using tracers seeded in one of the two merging vortices, or fluorescein throughout the turbulent field. Two main results are evident from figures 3.11 and 3.12. The first one is that during vortex merging, processes of filamentation lead to the expulsion of tracers out of

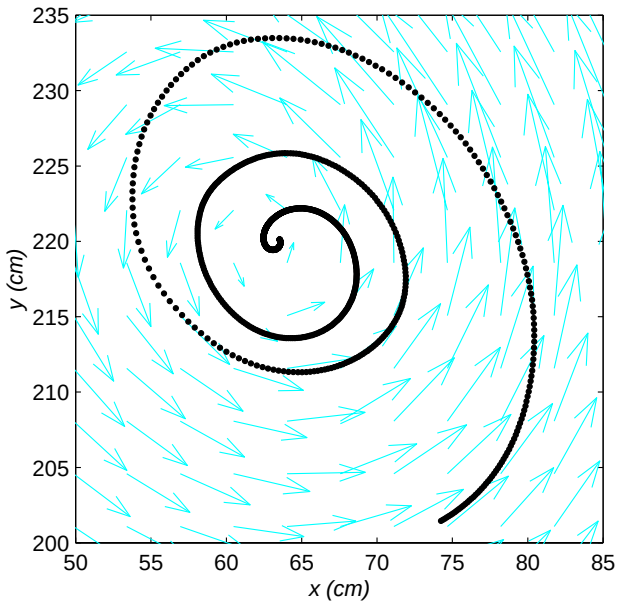

Figure 3.10: Evolved distribution after $t = 180$ *s* of a group of 3600 tracers initially placed on a radial line starting from the vortex centre. Azimuthal dispersion due to differential rotation is evident.

the coherent structures, the second one is that one can clearly distinguish the two vortex cores as individual entities even after the merging process has completed and only one vortex remains.

Entering the details, the first stage of the merging is characterized by a simple interaction of the two vortices which exchange materials through the saddle point localized in the middle of the line connecting their center (clearly visible in figure 3.12 at time $t = 30$ and $t = 32.5 min$). At this early stage, tracers which pass from one vortex to the other or are ejected into the background come from the outer shells of the merging vortices (black colour in figure 3.12). This stage can also evolve into incomplete merging of the two vortices, if the distance between the vortex centres is above a certain critical value (Melander et al. 1988) or if the external strain field keeps them apart; in this case, just some material coming from one vortex becomes part of the other.

If the merging process goes on, the following stage is characterized by stretching and elongation of one of the two vortices, normally the weaker one. At this stage, the core of the elongated vortex is still distinct, although tracers belonging to different shells start to mix together (figure 3.12, $t = 34$ *min*). Circling motion of the two vortices and differential rotation act together to produce vorticity filaments and tracer filaments. The tracers in the filaments do not belong to the inner shells, confirming that also during merging processes, trapping of tracers in vortex cores is very efficient (figure 3.12, $t = 35$ *min*).

The last stage of the merging is the axisimmetrization of the vortex derived

from the coalescence of the two original vortices. The final vortex has generally a larger size, if the two merging vortices have sizes comparable, while the maximum vorticity is almost conserved. Inside the core, tracers coming from the original vortices are still separated (although it is no more possible to distinguish the original shells). Filaments are released into the turbulent background, where they are dissipated by viscosity. Only on diffusive time scales the tracer populations of the two original vortices will mix together.

Experimental evidence, therefore, confirm the results obtained by means of numerical simulations of barotropic turbulence, and underline the importance of vortex structures in the overall transport of passive tracers. Vortices in a turbulent flow are shown to be topological areas with peculiar characteristics with respect to the turbulence itself, from both the Eulerian and the.Lagrangian points of view. The discussion on transport properties by coherent vortices will continue through next chapters, by considering real particles and tracers with finite size and finite inertia with respect to the fluid.

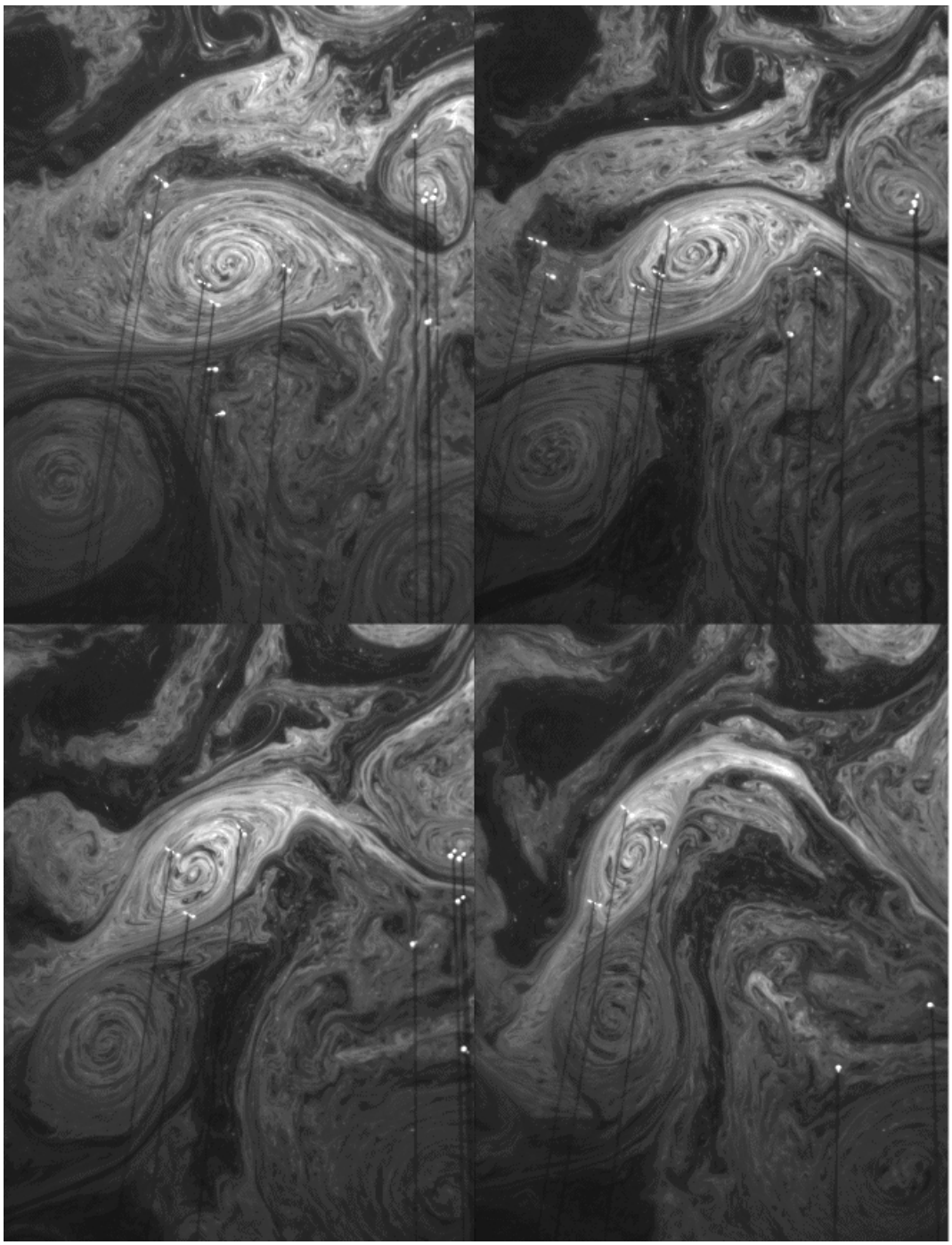

Figure 3.11: Sequence of LIF pictures showing the merging process of two cyclonic vortices. The time step between two subsequent images is 50 *s*. The experimental conditions are the same as in figure 3.7.

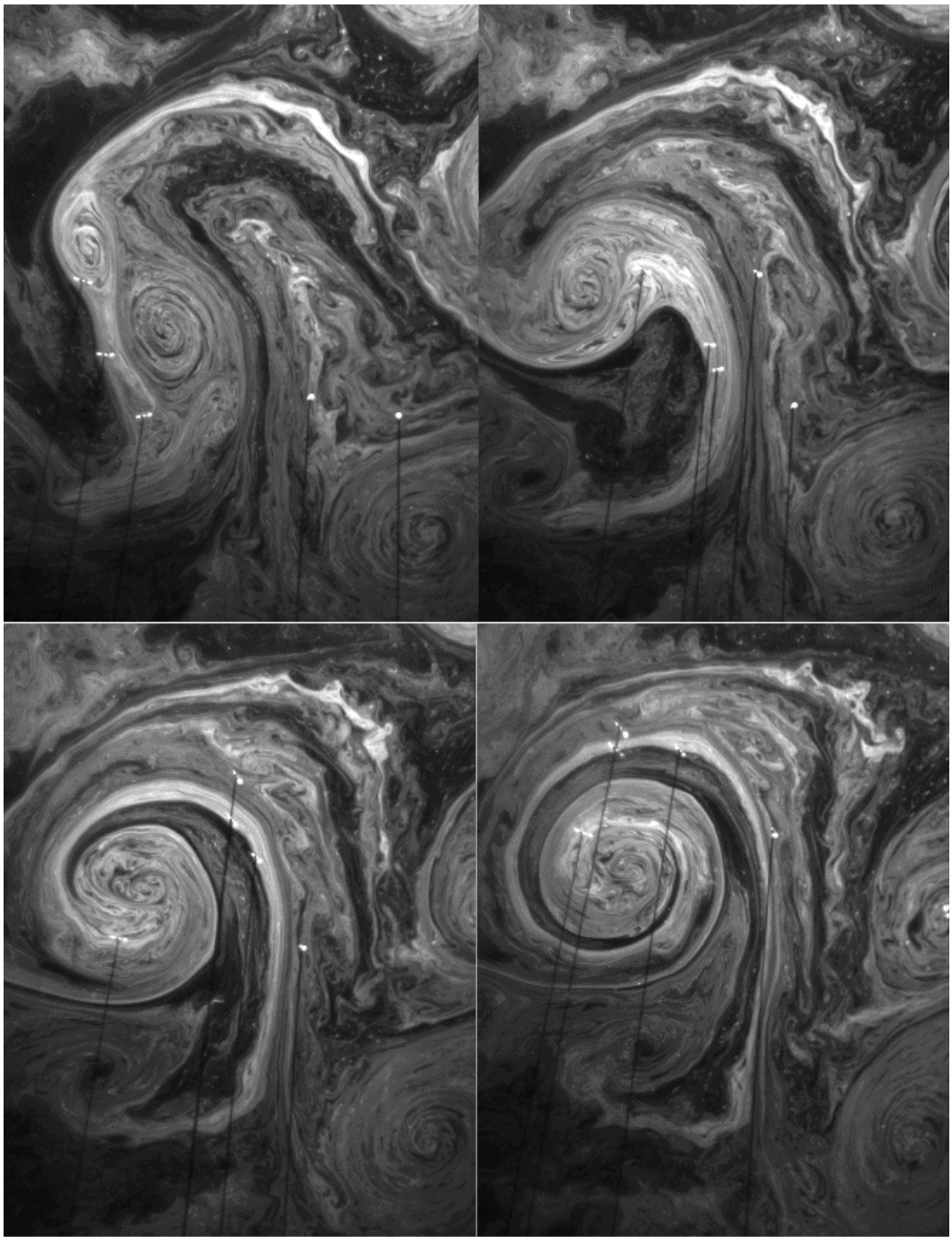

Figure 3.11: (continued)

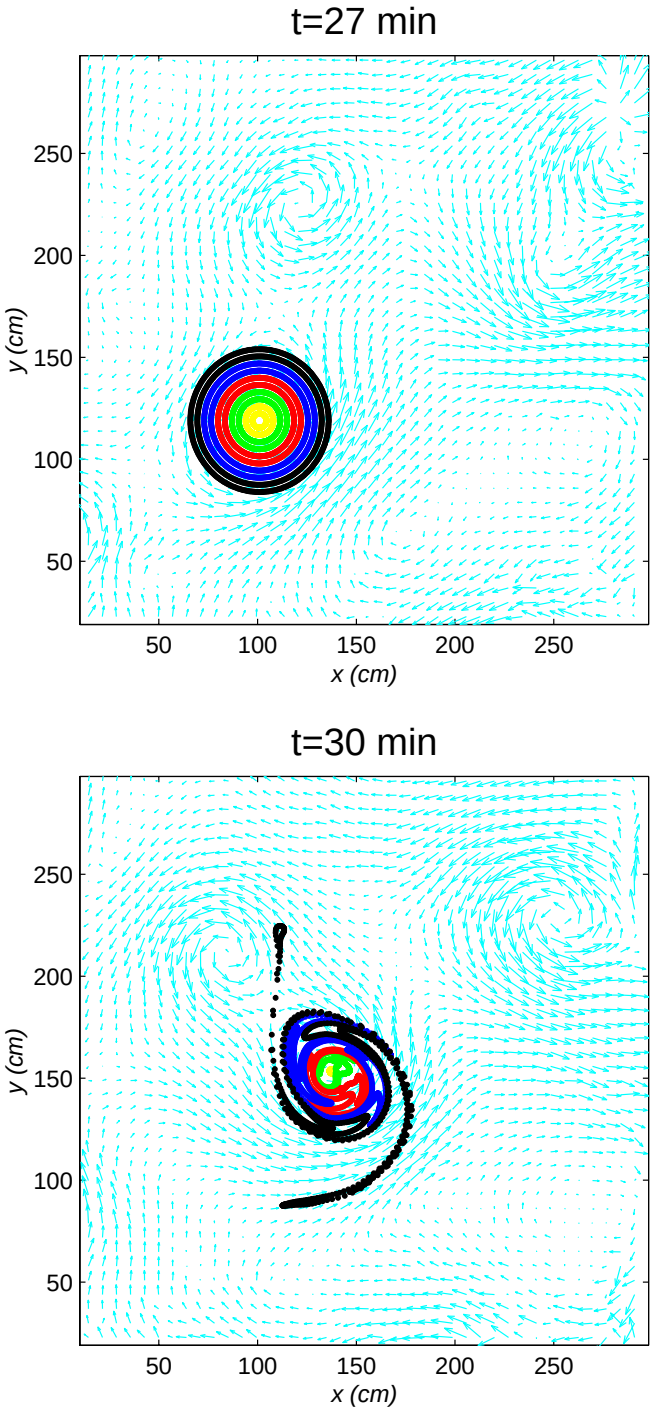

Figure 3.12: A view of vortex merging by means of the pseudo-experimental technique. The different panels show different times of the evolution of a patch of (3600) passive tracers seeded inside a merging cyclonic vortex. Different initial distance from the vortex centre is indicated by different colours. The experimental conditions are the same as in figure 3.7. The time $T = 0$ corresponds to the arrest of the rake.

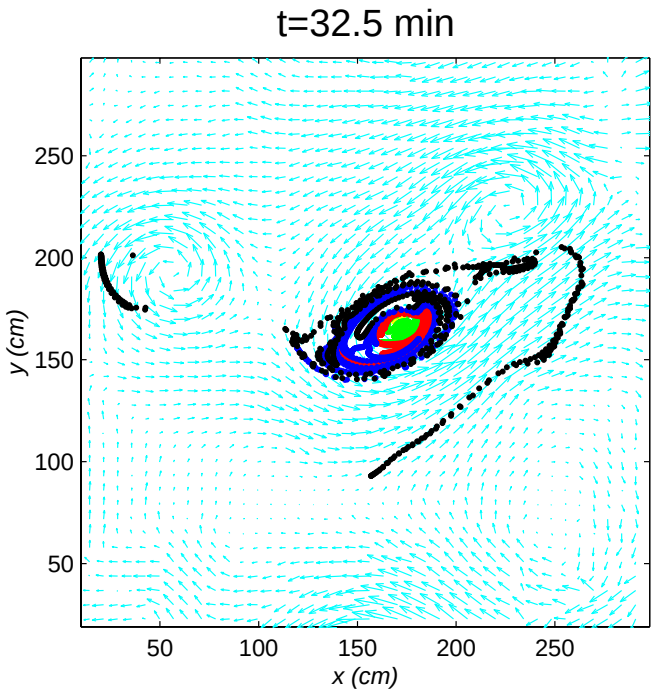

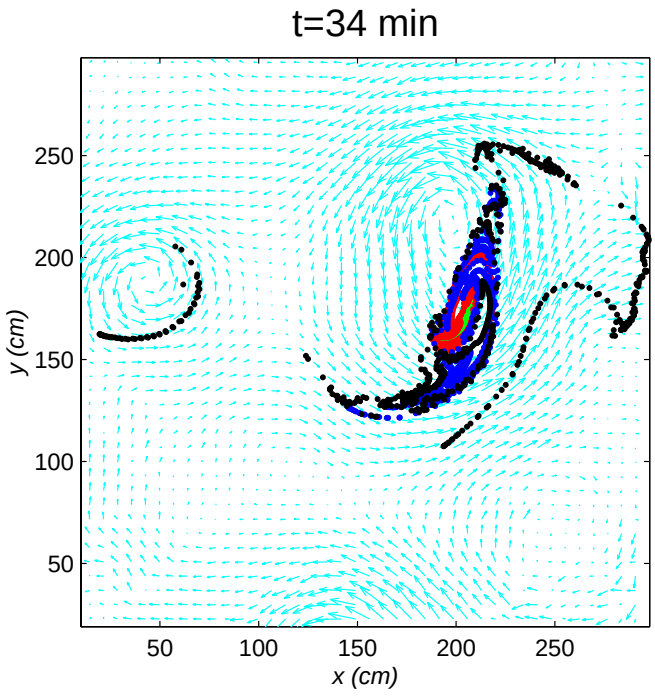

Figure 3.12: (continued)

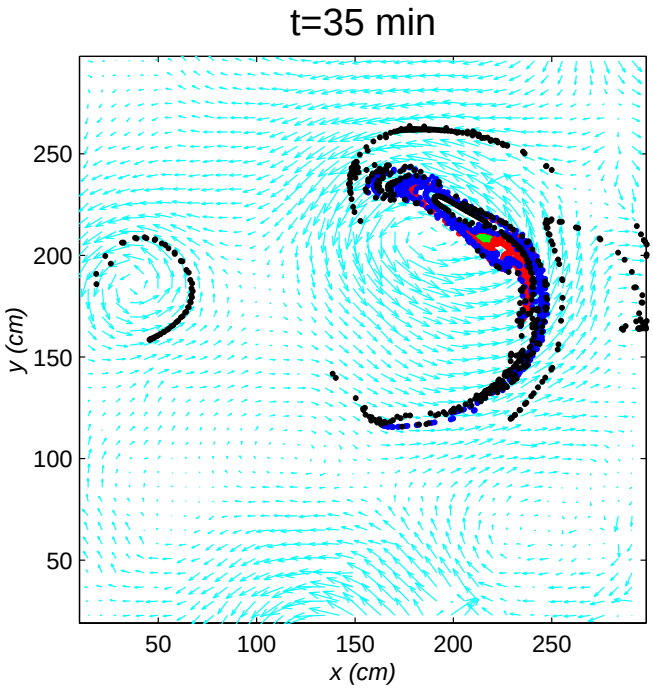

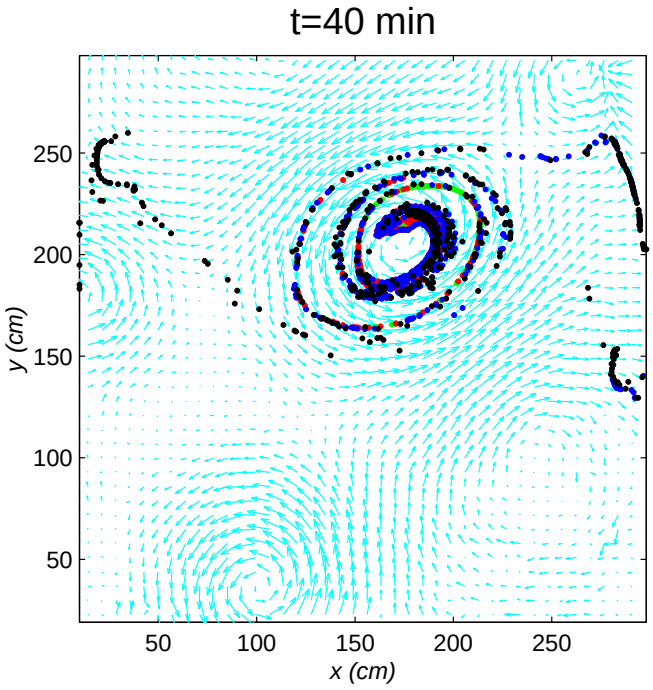

Figure 3.12: (continued)

Chapter 4

Lagrangian particles and impurities

Lagrangian particles are ideal neutrally-buoyant elements with infinitesimal size; their dynamics is described by the equivalence between the Lagrangian velocity at the particle and the Eulerian velocity of the particle position, and their trajectories are assimilated to fluid particle trajectories. Real particles embedded in a fluid, however, have small but finite size, and may have different density with respect to the surrounding fluid. For these *impurities*, the equation of motion comes from Newton's second law of dynamics. This chapter is devoted to the discussion of the equation of motion for impurities, to the description of the numerical set-up used to integrate the trajectories of individual impurities in a barotropic two-dimensional model, and to review some previous results on impurity dynamics in flows with the presence of vortices.

4.1 Fluid elements and Lagrangian particles versus impurities

Most of Lagrangian dynamics deals with ideal neutrally-buoyant elements which are considered point-like and massless. The dynamics of such elements is assimilated to the dynamics of fluid particles, therefore the same flow can be viewed as an evolving field (Eulerian description) or an ensemble of moving fluid particles (Lagrangian description). The link between the two descriptions is given by the equality between the Lagrangian velocity and the Eulerian velocity in the position of the fluid particles:

$$\mathbf{U}_f = \frac{d\mathbf{X}_f}{dt} = \mathbf{u}, \tag{4.1}$$

where $\mathbf{U}_f(t)$ is the Lagrangian velocity of a fluid particle whose position is given by $\mathbf{X}_f(t)$, and $\mathbf{u}(\mathbf{X}_f, t)$ is the velocity of the Eulerian field at the position $\mathbf{X}_f$.

Given the equation (4.1), it should always be possibile to pass from one description to the other, at least theoretically. Practically, it is possible only for stationary two-dimensional flows, whereas non-stationary flows displays chaotic Lagrangian dynamics even if the Eulerian velocity field is very simple (e.g., time periodic) and non-turbulent; see, for instance, Aref (1984), Aref & Balachandar (1984), Falcioni et al.(1988), Beloshapkin et al. (1989).

The description of a flow in term of trajectories of fluid elements is only accessible theoretically and numerically, not always experimentally. Laboratory and in-situ experiments use tracers which are not fluid elements, but external "impurities", although their characteristics approach those of fluid elements: the tracers have small size with respect to the fluid length scale and they have almost the same density as the fluid in which they are embedded. Such tracers are called *quasi-Lagrangian particles* or *quasi-Lagrangian tracers*, since they provide Lagrangian information almost as though they were fluid elements. Nevertheless, they are neither point-like (they have a finite size) nor massless (they may have small inertia with respect to the fluid).

The class of small particles with finite size and/or inertia (i.e., density different from the density of the fluid in which they are embedded), is altogether indicated by means of the term "impurities". Impurities may be such different as quasi-neutral buoyant tracers used in laboratory experiments (PIV tracers, for instance) or in in-situ geophysical measurements (floats and drifters in the oceans, balloons in the atmosphere), but also droplets or bubble in a two-phase flow, dust grains in the atmosphere, settling particles in turbulent flows or dust particles in the early solar nebula.

For such particles, equation (4.1) is no more valid. The equation of motion for impurities comes from Newton's second law of dynamics, where one has to take into account all the forces which can act on a small, foreign particle embedded in a viscous advecting flow:

$$m\frac{d^2\mathbf{X}}{dt^2} = \mathbf{F}(\mathbf{U}, \mathbf{u}); \tag{4.2}$$

here, m is the mass of the impurity, $\mathbf{X}$ and $\mathbf{U}(t)$ are, respectively, its position and velocity, $\mathbf{u}$ is the Eulerian velocity and $\mathbf{F}$ is the sum of the forces acting on the impurity (which are usually functions of the impurity velocity and the Eulerian velocity).

It is evident that the dynamics of impurities can be totally different from the dynamics of fluid elements, as well as from the dynamics of ideal Lagrangian tracers. Eulerian description of the flow and Lagrangian trajectories of impurities have not a biunivocal correspondence, not even in stationary flows: the Eulerian velocity field determines the impurity trajectories, but the contrary does not apply.

4.2 The equation of motion for passively advected impurities

4.2.1 Historical background

The equation of motion for small impurities that are passively advected by a velocity field has been matter of intense debate since the time of Stokes (1845), who formulated the steady-state equation of motion of a sphere in a viscous fluid, Boussinesq (1885a, 1885b) and Basset (1888a, 1888b), who developed independently the mathematical framework and the expression for the unsteady motion of a solid sphere inside an infinite, viscous and quiescent fluid, up to the recent formulation by Maxey & Riley (1983) in non rotating systems, which seems to be the dominant reference for most recent papers on this subject, both from the physical and the engineering points of view.

Maxey & Riley's equation of motion is developed for very small (with respect to the length scale of the flow), rigid, spherical impurities with small particle Reynolds number[1]. The impurities are considered as passive particles, i.e., they do not influence the dynamics of the advecting flow, except for local disturbances which are reflected in the equation of motion itself and are used for its derivation. In this formulation (which is valid for a three-dimensional flow), forces that act on an impurity are provided by an "inertial" term which is the force exerted by the flow directly on the impurity (and provided by the Navier-Stokes equation), the Stokes drag force, the gravitational force, the so-called "added-mass" term which is related to the boundary layer that forms around the moving impurity, and the Basset term which takes care of the past history of the impurity (it is also called "memory" term). Other less important terms are given by the so-called "Faxen corrections", which are due to the non-uniformity of the advecting flow.

The formulation by Maxey & Riley is valid in non-rotating reference frames; furthermore, it does not consider the possible lift force which arises when the spherical particles rotate in a fluid with different local translational velocity ("Magnus

[1]The particle Reynolds number is defined as $Re_{imp} = Wa/\nu$, where W is taken as a representative velocity scale for $\mathbf{U} - \mathbf{u}$, the velocity of the impurity relative to that of the surrounding fluid, a is the radius of the spherical impurity and ν is the kinematic viscosity of the fluid.

effect", Magnus 1861) or simply move in a shear flow ("Saffman effect", Saffman 1965). Usually the Magnus effect is difficult to evaluate, except than in very specific situations; on the other hand, Saffman proposed a model for the expression of the lateral force (i.e., lift force) on a sphere in shear flows, which is used mostly as an added component to the total hydrodynamic force acting on an impurity. More recently, Auton (1987) and Auton et al. (1988) have calculated the lift force on a sphere in rotating flows.

A complete of the history of the equation of motion for impurities in non-rotating systems is provided by Michaelides (1997). In rotating reference frames, apparent forces arise (Coriolis force and centrifugal force), thus in the equation of motion one has to take them into account. Tanga et al. (1996) and Chavanis (2000) have recently dealt with impurities in a rotating system. In these two cases, the rotating reference frame is the early solar nebula and the key issue is the effect of the Coriolis force on very heavy dust particles.

4.2.2 The equation of motion for impurities in a 2D rotating flow

In this thesis, I address the study of the dynamics of impurities in a barotropic, rapidly rotating, turbulent flow. In particular, my purpose is to clarify the role played by coherent vortices in the dynamics and transport of finite-sized particles which are lighter or heavier than the surrounding fluid. The special case of finite-sized, neutrally-buoyant tracers is also considered in chapter 7; this case has an immediate application to laboratory experiments.

The system in which I study the dynamics of impurities is two-dimensional freely-decaying turbulence. No free-surface or ageostrophic effects are considered, thus my results are not directly applicable to a geophysical model. Nevertheless, this is a basic study of the impurity dynamics in a turbulent flow characterized by fully-developed coherent vortices, thus the choice of a simple model is, without loss of generality, the first step to understand the behaviour in more complicated flows.

A two-dimensional equation of motion for impurities is used. It comes from the formulation by Maxey & Riley (1983), which is extended to a rotating reference frame. For very small[2], rigid, spherical impurities with a small Reynolds number, embedded in a 2D rotating fluid layer, the equation of motion are written as:

$$\begin{aligned}\rho_p \frac{d^2\mathbf{X}}{dt^2} &= \rho_f \frac{D\mathbf{u}}{Dt} - \frac{9\rho_f \nu}{2a^2}\left(\frac{d\mathbf{X}}{dt} - \mathbf{u}\right) - \frac{1}{2}\rho_f \frac{d}{dt}\left(\frac{d\mathbf{X}}{dt} - \mathbf{u}\right) \\ &\quad -2\boldsymbol{\Omega} \times \left(\rho_p \frac{d\mathbf{X}}{dt} - \rho_f \mathbf{u}\right) + \frac{1}{2}\rho_f \left(\frac{d\mathbf{X}}{dt} - \mathbf{u}\right) \times \omega, \qquad (4.3)\end{aligned}$$

where $\mathbf{X}(t) = (X(t), Y(t))$ is the instantaneous position of the impurity in the two-dimensional Eulerian velocity field $\mathbf{u}(\mathbf{x}, t) = (u(\mathbf{x}, t), v(\mathbf{x}, t))$, $d/dt = \partial/\partial t + (d\mathbf{X}/dt) \cdot \nabla$ is the total time derivative following the impurity (the "particle derivative"), $D/Dt = \partial/\partial t + (\mathbf{u} \cdot \nabla)$ is the material derivative following the fluid motion,

[2] $a \ll L$, where a is the radius of the impurity and L a characteristic length scale of the flow

a is the radius of the spherical impurity, ρ_p and ρ_f are respectively the density of the impurity and of the fluid element with the same volume, ν is the kinematic viscosity, $\mathbf{\Omega}$ is the angular velocity of the rotating reference frame and $\boldsymbol{\omega} = \nabla \times \mathbf{u}$ is the vorticity.

The l.h.s. of equation (4.3) represents the Lagrangian acceleration of the impurity due to the forces acting on it, which are provided by terms on the r.h.s. of the equation. These are:

(i) $\rho_f \frac{D\mathbf{u}}{Dt}$, the force exerted by the fluid on the impurity, in general provided by the Navier-Stokes equation applied in the instantaneous position occupied by the particle. This is also called "inertial term";

(ii) $-\frac{9\rho_f \nu}{2a^2}\left(\frac{d\mathbf{X}}{dt} - \mathbf{u}\right)$, the Stokes drag on the impurity. This term depends on the relative velocity between the fluid and the particle. The present formulation is appropriate for laminar motion; for turbulent flows, this term is sometimes written as $-C\left(\frac{d\mathbf{X}}{dt} - \mathbf{u}\right)\left|\frac{d\mathbf{X}}{dt} - \mathbf{u}\right|$, which has, however, a similar effect on the dynamics;

(iii) $-\frac{1}{2}\rho_f \frac{d}{dt}\left(\frac{d\mathbf{X}}{dt} - \mathbf{u}\right)$, the added mass term. This is due to the boundary layer that forms around the moving impurity;

(iv) $-2\Omega \times \left(\rho_p \frac{d\mathbf{X}}{dt} - \rho_f \mathbf{u}\right)$, the Coriolis force that acts only in a rotating reference frame and depends on the velocity difference between the impurity and the fluid, weighted by the respective densities;

(v) $\frac{1}{2}\rho_f \left(\frac{d\mathbf{X}}{dt} - \mathbf{u}\right) \times \omega$ is the lift force in the formulation by Auton (1987) and Auton et al. (1988) in rotating flows.

Having in mind possible geophysical applications of the 2D flow model in which I study the dynamics of impurities, buoyancy and centrifugal force do not compare into equation (4.3), since they depend on the gradient of the total (gravitational and centrifugal) potential, which is mostly in the local vertical direction on the Earth's surface; buoyancy and centrifugal force, therefore, do not influence the horizontal motion.

Further on, I disregard the effect of the so-called Faxen corrections, which are terms proportional to $a^2\nabla^2\mathbf{u}$, due to the non-uniformity of the Eulerian flow. The reason is that, performing a scale analysis where L is the length scale of the flow and a is the particle radius, the Faxen terms are of order $O\left(a^2/L^2\right)$ with respect to the other terms, and can thus be discarded, since we suppose $a \ll L$. I do not consider another term in equation (4.3), that is the Basset term, or "memory term". The Basset term is assumed to have negligible influence on the impurity dynamics in rotating flows; see Paradisi & Tampieri (2001) for details about the effects of this term on the impurity dynamics in non-rotating systems.

The equation of motion (4.3) may be conveniently nondimentionalized in order to identify the parameters which govern the dynamics of the impurities:

$$\begin{aligned}\frac{d^2\mathbf{X}}{dt^2} &= \Delta\frac{D\mathbf{u}}{Dt} - \gamma\left(\frac{d\mathbf{X}}{dt} - \mathbf{u}\right) + \frac{1}{2}\Delta\frac{d\mathbf{u}}{dt} \\ &\quad -\frac{\Delta}{\delta}Ro^{-1}\mathcal{Z}\times\left(\frac{d\mathbf{X}}{dt} - \delta\mathbf{u}\right) + \frac{1}{2}\Delta\left(\frac{d\mathbf{X}}{dt} - \mathbf{u}\right)\times\omega, \qquad (4.4)\end{aligned}$$

where now $\mathbf{X}$, $\mathbf{u}$ and t are nondimensional variables and $\mathcal{Z}$ is the versor of the local z-axis: I consider, in fact, an angular velocity vector for the rotating system given by $\mathbf{\Omega} = (0, 0, \Omega_z)$, which can be thought as the local vertical projection of the Earth's angular velocity, and $\omega = (0, 0, \zeta)$ is the relative vorticity vector, which has only the vertical component in a 2D flow.

The free parameters of equation (4.4) are given by the *Rossby number* $Ro = U/fL$ (where f is the Coriolis parameter, which is equal to $2\Omega\sin(\theta)$ if we consider a fluid layer on the *f*-plane at latitude θ) and by:

$$\delta = \frac{\rho_f}{\rho_p}, \quad \gamma = \frac{9}{2}\Delta\left(\frac{L}{a}\right)^2 Re^{-1}, \qquad (4.5)$$

where L and U are respectively the length and velocity scale of the flow, $Re = UL/\nu$ is the *Reynolds number*, $\Delta = 2\delta/(2+\delta)$ is the scaled density ratio, due to the presence of the added mass term, and γ is sometimes called the *Stokes number* or Stokes parameter. The crucial difference among light, heavy and neutral impurities is given by the parameter δ: $\delta < 1$ is for impurities lighter than the fluid, $\delta > 1$ characterizes heavy impurities and $\delta = 1$ is for neutrally-buoyant tracers.

4.3 Numerical set-up

After the discussion on impurity dynamics in simple, stationary, analytical flows in chapter 5, chapter 6 and chapter 7 are devoted to the study of impurity dyamics in a two-dimensional turbulent flow. The numerical set-up used at this purpose is briefly outlined in this section.

The incompressible, homogeneous, rotating, 2D advective flow is governed by the (nondimensional) 2D vorticity equation (1.47) in free decay. Newtonian viscosity is replaced by hypeviscosity, in order to reach higher effective Reynolds numbers and to have dissipation at smallest scales (see footnote at page 27. The equation for the advective flow thus reads:

$$\frac{\partial\zeta}{\partial t} + J(\psi, \zeta) = -\nu_2\nabla^4\zeta, \qquad (4.6)$$

where $\zeta = \nabla^2\psi$ is the vertical component of the relative vorticity, $\psi(x, y)$ is the stream function, defined in such a way that the components of the horizontal velocity are $u(x, y) = -\partial\psi/\partial y$ and $v(x, y) = \partial\psi/\partial x$, J is the Jacobian operator

$J[a,b] = a_x b_y - a_y b_x$ and $\nu_2 = 5 \cdot 10^{-8}$ is the hyperviscosity coefficient (see Benzi et al. 1987, McWilliams 1984, 1990, Larichev & McWilliams 1991).

I perform the numerical experiments in a doubly periodic square domain with size 2π, using a pseudospectral code with standard $2/3$ dealiasing and a third-order Adam-Bashford time integrator scheme for the Eulerian equation (4.6); the spatial resolution is 512×512 grid points and the non-dimensional time step is $dt = 10^{-3}$.

The positions of impurities are obtained by integration of the (nondimensional) equation of motion (4.4). A third-order Adam-Bashford time integrator scheme and a sixth-order spectral spline interpolator are used for the integration of this latter equation.

Since I am interested in the dynamics of impurities in fully developed two-dimensional turbulence, I firstly perform the numerical integration of equation (4.6) until a nondimensional time $t_i = 20$, which is equivalent to 664 times the initial eddy turnover time $\tau_{eddy}\,(t=0)$. The initial conditions for the vorticity field in this first step are the same as in McWilliams (1990), i.e. a Gaussian random realization for the phases of each Fourier component of the field, using a fixed energy spectrum and an initial kinetic energy $E_0 = 0.5$ (see figure 1.3a). Secondly, 4096 impurities are seeded uniformly in the vorticity field at time $t_i = 20$, dominated by fully developed vortices (the pattern of the turbulent field is similar to that depicted in figure 1.3b), and the numerical simulations are performed until time $t_f = 35$, corresponding to 47 eddy turnover times at $t = t_i$ (at this time, the turbulent field is shown by figure 1.3b). The initial velocities of the impurities are equal to the Eulerian velocity (except fot the special case of neutrally buoyant impurities, as specified in chapter 7, for which initial velocities are zero).

The free parameters in equation (4.4) are chosen accordingly to geophysical scales. For a two-dimensional model of the ocean or the atmosphere on the f-plane, for instance, the typical scales are $L = 10^5$ *m* and $U = 0.1 \div 1$ *m/s*, which give a Reynolds number $Re = 10^{10} \div 10^{11}$ and a Rossby number $Ro = 0.1 \div 0.01$ at mid-latitudes where $f = O\left(10^{-4}\right)$. Using these scale values, and considering a ratio $(L/a) = O\left(10^5 \div 10^6\right)$, the order for the γ parameter is $O\left(10\right)$. I thus study the dynamics of impurities with γ in the range $5 \div 50$ and Ro in the range $0.01 \div 0.1$.

4.4 Previous results on impurity dynamics in vortical flows

Several studies have been carried out in the last ten years in order to understand the dynamics of small impurities embedded in a fluid when vortices are a strong component of the flow. Most of them have been performed by using very simple, mostly stationary, 2D analytical flows characterized by the presence of a sequence of cellular vortices. In non-rotating systems, vortex centres (both cyclonic and anticyclonic) are asymptotically stable fixed points for light impurities ($\delta < 1$), which are attracted toward the center of vortices, whereas they are unstable for

heavy particles ($\delta > 1$), which are ejected out of vortex cores (Crisanti et al. 1990, 1992, Tanga & Provenzale 1994). In the case $\delta = 1$ (neutral impurities), the initial relative velocity plays an important role in the dynamics: for zero initial relative velocity, vortex centres are neutrally stable points, but finite relative velocities allow the neutral impurities to approach the vortex centres in a transient time whose duration is determined by the Stokes parameter (Babiano et al. 2000).

In rotating systems, the Coriolis force acts as a centripetal force for heavy impurities in anticyclonic vortices, and tends to push them toward the center of anticyclones, providing, for instance, a possible astronomical mechanism for dust particles aggregation and formation of planetesimals in the early solar nebula (Tanga et al. 1996, Bracco et al. 1999, Chavanis 2000). Some other effects, due to the lift force and the so-called Basset force that act on an impurity, have been taken into account by Thomas (1992), Druzhinin and Ostrovsky (1994), Paradisi & Tampieri (2001).

Chapter 5

Dynamics of impurities in stationary vortical flows

The dynamics of impurities in stationary, analytical flows, characterized by the presence of vortex structures, is discussed. In particular, the cellular flow, constituted by the repetition of a sequence of vortices, and the Gaussian vortex model are considered. The dynamics of impurities is analyzed with respect to the different forces that occur in the equation of motion, and with respect to the different governing parameters. Both non-rotating and rotating reference frames are discussed.

5.1 Stationary vortical flow models

As pointed out at the end of the previous chapter, many results on impurity dynamics in vortices have been obtained by using simple, analytical, stationary, 2D flow models constituted by the repetition of a sequence of cyclonic and anticyclonic vortices (figures 5.1 and 5.2). These cellular flows may be described by the following (nondimensional) stream functions:

$$\psi_{c1}(x, y) = \psi_0 (\cos x + \cos y), \tag{5.1}$$

$$\psi_{c2}(x, y) = \psi_0 (\cos x \cdot \cos y), \tag{5.2}$$

which give different patterns for the Eulerian fields but the same results with respect to the dynamics of impurities: linearization of equations (5.1) and (5.2) in vortex centres (elliptic fixed points) and in vortex "vertices" (hyperbolic fixed points), in fact, leads to the same expression for the two stream functions.

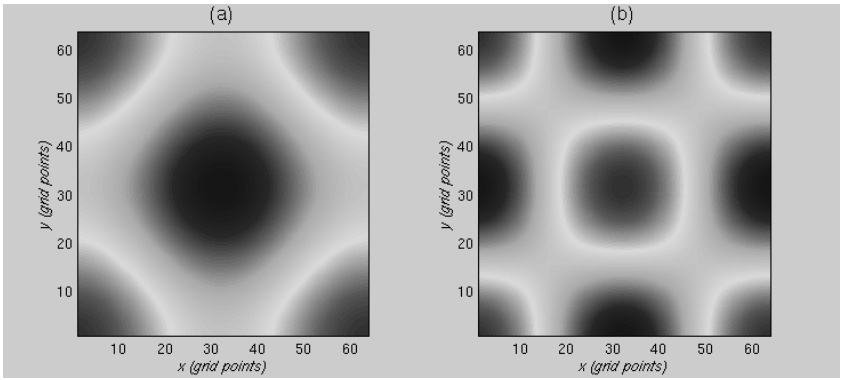

Figure 5.1: Pattern of the two-dimensional cellular flows described by the stream functions: (a) $\psi_{c1}(x, y) = \psi_0 (\cos x + \cos y)$; (b) $\psi_{c2}(x, y) = \psi_0 (\cos x \cdot \cos y)$.

By considering these analytical, advective flow models, linear stability analysis may be used in the (nondimensional) equation of motion for impurities (4.4), in order to study the dynamics of light and heavy particles around the fixed points (in particular, the vortex centres).

Cellular flows, although useful for obtaining analytical results, have limited physical correspondence: vorticity and velocity profiles of a vortex in a cellular flow are different from the profiles of a coherent vortex in 2D turbulence (see, e.g., figures 2.13-2.16). A more reliable model of a vortex structure is provided by Carton et al. (1989), and is often applied to laboratory vortices (see Hopfinger & van Heijst 1993) and oceanic vortices (see Simpson et al. 1984). This is an analytical model of an isolated, circular, two-dimensional vortex, parameterised by the vorticity-profile "steepness" α. Such a vortex is described, in polar coordinates

(r, θ), by a (nondimensional) expression for the stream function,

$$\psi'(r') = -\psi'_0 \exp\left(-2\frac{r'^{\alpha}}{\alpha}\right), \tag{5.3}$$

which depends only on the nondimensional distance $r' = r/L$ from the vortex centre, ψ'_0 being the value of the nondimensional stream function in the centre and L the scale of the vortex radius.

The case $\alpha = 2$ corresponds to a Gaussian profile of the stream function and it is called the *Gaussian vortex model* for an isolated vortex:

$$\psi'_G(r') = -\psi'_0 \exp\left(-r'^2\right). \tag{5.4}$$

In this model, the expressions for the (nondimensional) vorticity, the azimuthal velocity and the Okubo-Weiss parameter read:

$$\begin{aligned} \zeta'(r') &= 4\psi'_0\left(1 - r'^2\right)\exp\left(-r'^2\right), \\ u'_\theta(r') &= 2\psi'_0 r' \exp\left(-r'^2\right), \\ Q'(r') &= -16\psi'^2_0\left(1 - 2r'^2\right)\exp\left(-r'^4\right), \end{aligned} \tag{5.5}$$

and they are plotted in figure 5.2. The radial velocity, which is defined as $u'_r = -\dfrac{1}{r'}\dfrac{\partial\psi'}{\partial\theta}$, is throughout zero. The azimuthal velocity has an extreme (maximum or minimum depending on the vortex sign) at $r' = 1/\sqrt{2} \cong 0.71$, corresponding to the value $Q = 0$ (vortex edge). Note that the value $\psi'_0 = \zeta'_0/4$, where ζ'_0 is the vorticity in the centre of the vortex, is a new free (Eulerian) parameter for the study of the dynamics of impurities. This vortex model has the advantage to match the kinetic energy and Q-function curves that charachterize a typical isolated vortex in two-dimensional turbulence, as shown by the cross-sections in figures 2.13-2.16.

The isolated Gaussian vortex model described above consists of a core surrounded by an annulus of oppositely-signed vorticity, in such a way that the vortex contains zero net vorticity. In barotropic turbulence, however, usually a vortex has a single-signed vorticity. A Gaussian vortex model with single-signed vorticity can be obtained by writing a Gaussian expression for relative vorticity instead of stream function:

$$\zeta'_{IG}(r') = \zeta'_0 \exp\left(-r'^2\right). \tag{5.6}$$

Azimuthal velocity in this latter case reads:

$$u'_\theta(r') = \frac{\zeta'_0}{2r'}\left[1 - \exp\left(-r'^2\right)\right], \tag{5.7}$$

where the relationship $\psi'_0 = \zeta'_0/4$ still applies. Instead of rapidly decreasing to zero, azimuthal velocity for a non-isolated vortex has a longer, less steep tail, which extends the vortex influence far from its core (see figure 5.3).

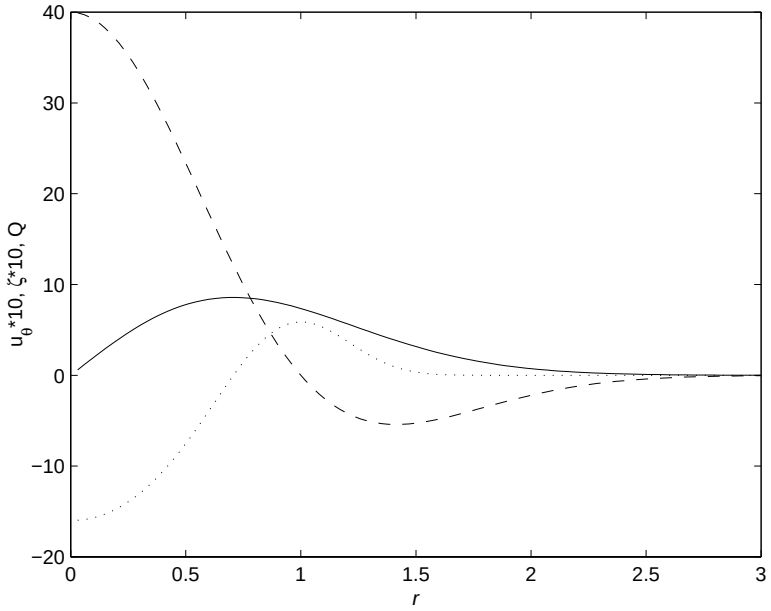

Figure 5.2: Plots of azimuthal velocity (solid line), vorticity (dashed line) and Okubo-Weiss parameter (dotted line) for the isolated Gaussian vortex model. The radial distance is nondimensional and $\psi_0' = 1$.

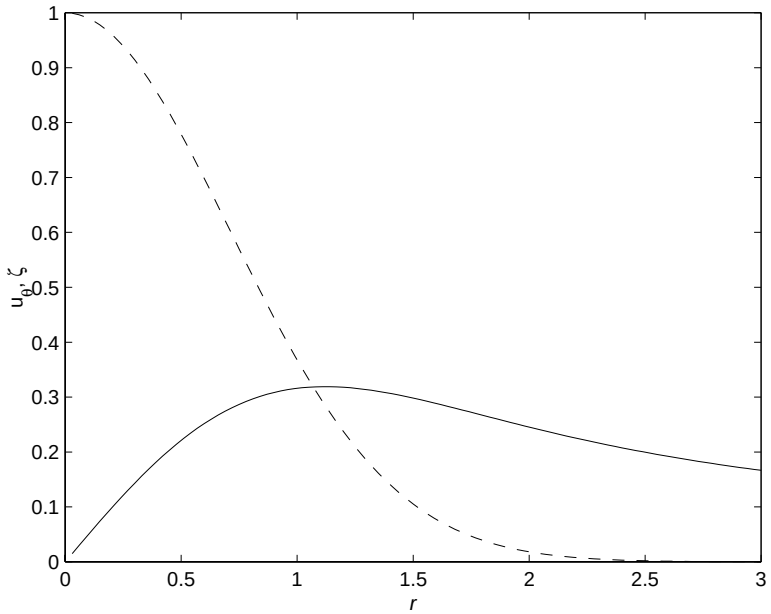

Figure 5.3: Plots of azimuthal velocity (solid line) and vorticity (dashed line) for the Gaussian vortex model with single-signed vorticity. The radial distance is nondimensional and $\zeta_0' = 1$.

By using the linearized, equivalent Cartesian expression of azimuthal velocity (5.5) or (5.7) in a neighborhood of the vortex centre, it is easy to verify that one obtaines the same results as by using the stream function for a cellular flow.

For the linear stability analysis of the equation of motion (4.4) for impurities around the vortex centres, the four models described above are equivalent. The difference of the Gaussian vortex model (isolated or non-isolated) with respect to the simple cellular flow lies in the nonlinear effect introduced by the presence of the extreme of the azimuthal velocity at the edge of the vortex, where $Q \approx 0$.

From now on, I disregard the primes. Variables have to be considered as nondimensional.

5.2 Linear stability analysis of the equation of motion for impurities

Inside vortex cores, a linear approach may capture the dynamical behaviour of light and heavy particles, thus a linear stability analysis of the complete equation (4.4) is performed around the centre of an isolated Gaussian vortex, by using both a cyclone and an anticyclone (given respectively by the values $\psi_0 > 0$ or $\psi_0 < 0$). The linearized Cartesian components of the velocity field in the neighborhood of $(0, 0)$ read:

$$\begin{aligned} u(x, y) &= -2\psi_0 y + O\left(\left(x^2 + y^2\right)^{3/2}\right) \\ v(x, y) &= +2\psi_0 x + O\left(\left(x^2 + y^2\right)^{3/2}\right). \end{aligned} \tag{5.8}$$

The analysis is performed separately in non-rotating and rotating reference frames, in order to isolate the effects of the Coriolis force on the impurity dynamics. Furthermore, the role of the lift force is also analized separately.

5.2.1 Non-rotating reference frames

In non-rotating reference frames, and without considering the lift force, the equation of motion for impurities simply reads:

$$\frac{d^2\mathbf{X}}{dt} = \Delta\frac{D\mathbf{u}}{Dt} - \gamma\left(\frac{d\mathbf{X}}{dt} - \mathbf{u}\right) + \frac{1}{2}\Delta\frac{d\mathbf{u}}{dt}. \tag{5.9}$$

The equivalent linearized system of differential equations can be written in matrix form (I set $a = 2\psi_0 = \zeta_0/2$, $U = dX/dt$ and $V = dY/dt$)):

$$\frac{d}{dt}\begin{pmatrix} X \\ Y \\ U \\ V \end{pmatrix} = \begin{pmatrix} 0 & 0 & 1 & 0 \\ 0 & 0 & 0 & 1 \\ -a^2\Delta & -a\gamma & -\gamma & -a\Delta/2 \\ a\gamma & -a^2\Delta & a\Delta/2 & -\gamma \end{pmatrix}\begin{pmatrix} X \\ Y \\ U \\ V \end{pmatrix}. \tag{5.10}$$

The solution for the linear system is expressed for each component of the impurity position vector in phase space $\mathbf{X} = (X, Y, U, V)$ as a linear combination of

exponentials, $X_i \sim \sum_k \exp(\lambda_k t)$, where the values λ_k are the solutions of the fourth-order eigenvalue equation given by $\det(A - \lambda I) = 0$ (being A the coefficient matrix in system (5.10) and I the identity matrix). For this system, the eigenvalues are complex conjugates, then only two real parts are distinct. The maximum relative value between the two distinct real parts determines the behaviour of the impurities where the linear approximation is valid: if $Re_M = \max(\lambda_1, \lambda_3)$ is negative, the vortex centre (which is a fixed point for system (5.10)) is a stable point, since all the eigenvalues have negative real parts, and Re_M is a measure of the time needed to the impurity to converge toward the centre, starting from an initial position $\mathbf{X} = (X_0, Y_0, U_0, V_0)$, supposed to be still in the linear regime; if Re_M is positive, the vortex centre is unstable, since there is at least one eigenvalue which has positive real part, and Re_M gives an estimate of the growth rate of the distance of the impurity from the initial position in phase space. If all the four eigenvalues have real part equal to zero, the vortex centre is neutrally stable.

The parameter δ (and thus the related Δ parameter) in the inertial and the added mass terms is fundamental in differing the dynamics of the three types of impurities (light, heavy and neutral) in vortex cores. Solutions for Re_M shows that the value $\delta = 1$ (and therefore $\Delta = 2/3$) represents a separation between two very different dynamical regimes: for values $\delta > 1$ (light impurities), the vortex centres (both cyclonic and anticyclonic) are asymptotically stable points, whereas for $\delta < 1$ (heavy impurities) these fixed points are unstable. Physically, this means that vortex centres attract impurities less dense than the fluid and repell impurities that are denser than the fluid, the further δ is from one, the stronger the effects. The Stokes drag further acts to increase or reduce (according to the value of γ) the speed of approach to the vortex centres of light particles or the speed of removal of heavy particles, but it does not change the scenario determined by δ (see also Crisanti et al. 1990, 1992 and Paradisi & Tampieri 2001). In the case $\delta = 1$ (neutral impurities), vortex centres are neutrally stable points (real parts of the eigenvalues are all zero), thus these particles undergo stable circular trajectories around the centre. But the initial relative velocity plays an important role in the dynamics of neutrally-buoyants impurities (see chapter 7).

As already pointed out, the value of Re_M gives an estimate of the capture time towards the vortex centre for light impurities or the expulsion time out of the vortex core for heavy impurities. The asymptotic behaviours of Re_M, at δ and ζ_0 fixed, for small and large Stokes parameters give an estimate of the corresponding behaviours of capture and expulsion times as function of γ: they are $\dfrac{1}{\gamma}$ at small Stokes parameters and γ at large ones (see Paradisi & Tampieri 2001).

5.2.2 The effects of the Coriolis force in rotating systems

In rotating reference frames, by adding the Coriolis force $-\dfrac{\Delta}{\delta} Ro^{-1} \mathcal{Z} \times \left(\dfrac{d\mathbf{X}}{dt} - \delta \mathbf{u} \right)$ in the equation of motion (5.9), the matrix form of the linearized system of differential equations reads (I set $\varepsilon = Ro^{-1}$):

$$\frac{d}{dt}\begin{pmatrix} X \\ Y \\ U \\ V \end{pmatrix} = \begin{pmatrix} 0 & 0 & 1 & 0 \\ 0 & 0 & 0 & 1 \\ -a\Delta\left(\varepsilon + a\right) & -a\gamma & -\gamma & -\Delta\left(\frac{a}{2} - \frac{\varepsilon}{\delta}\right) \\ a\gamma & -a\Delta\left(\varepsilon + a\right) & \Delta\left(\frac{a}{2} - \frac{\varepsilon}{\delta}\right) & -\gamma \end{pmatrix}\begin{pmatrix} X \\ Y \\ U \\ V \end{pmatrix} \tag{5.11}$$

For system (5.11), the results change if one considers an anticyclone or a cyclone. In particular, for an anticyclone the constant $a = 2\psi_0$ is negative, then the value $Ro = -1/2\psi_0$ is critical, as the terms (3,1) and (4,2) in the matrix become zero and the terms (3,4) and (4,3) reduce to, respectively, $-a$ and $+a$. It is possible to verify with some algebra that, in this particular case, two real parts of the four eigenvalues are zero and the other two are negative, which means that the anticyclonic centre becomes rapidly neutrally stable for $Ro = -1/2\psi_0 = -2/\zeta_0$, being ζ_0 the negative vorticity in the centre. This does not happen for a cyclonic vortex, for which a is positive; in this case, a critical value is given by $Ro = 1/\delta\psi_0$, for which the system (5.11) reduces to the simplest case, without Coriolis force and added mass term.

The differences between cyclones and anticyclones with respect to the dynamics of light and heavy impurities inside vortex cores can be summarized by using the plots of Re_M in figure 5.4, as function of the Rossby number and the Stokes parameter, in the case with $\zeta_0 = 4\psi_0 = 40$:

- in a cyclone, light impurities are always attracted toward the centre, heavy impurities always escape out of the core. The capture time and the expulsion time are minimum for large γ and small Rossby number. These properties depend of course on the value of the vorticity in the centre: in general, the stronger the vorticity is, the faster capture or expulsion processes are, especially at large γ and Rossby number;

- in an anticyclone, for $Ro < -2/\zeta_0$ light impurities are expelled whereas heavy impurities are attracted toward the centre (this result has already been underlined by Tanga et al. 1996 and recently by Chavanis 2000). A strong minimum in the capture and expulsion times is evident for small γ and $Ro \approx -1/\zeta_0$. For $Ro > -2/\zeta_0$, on the contrary, light impurities are slowly attracted and heavy impurities are slowly expelled. From a physical point of view, the discriminating condition is given by the comparison between the angular velocity in the centre of the anticyclonic vortex, due to the rotation of the vortex itself, and twice the value of the angular velocity of the rotating reference frame: this comes from the fact that $\frac{d\theta}{dt}\left(r = 0\right) = \frac{u_\theta}{r} = 2\psi_0$ and $Ro = U/2\Omega L$, where Ω is the angular velocity of the system.

5.2.3 The role of the lift force

Lift force does not introduce significant changes in the scenario previously depicted. The matrix form of the linearized system of differential equations reads:

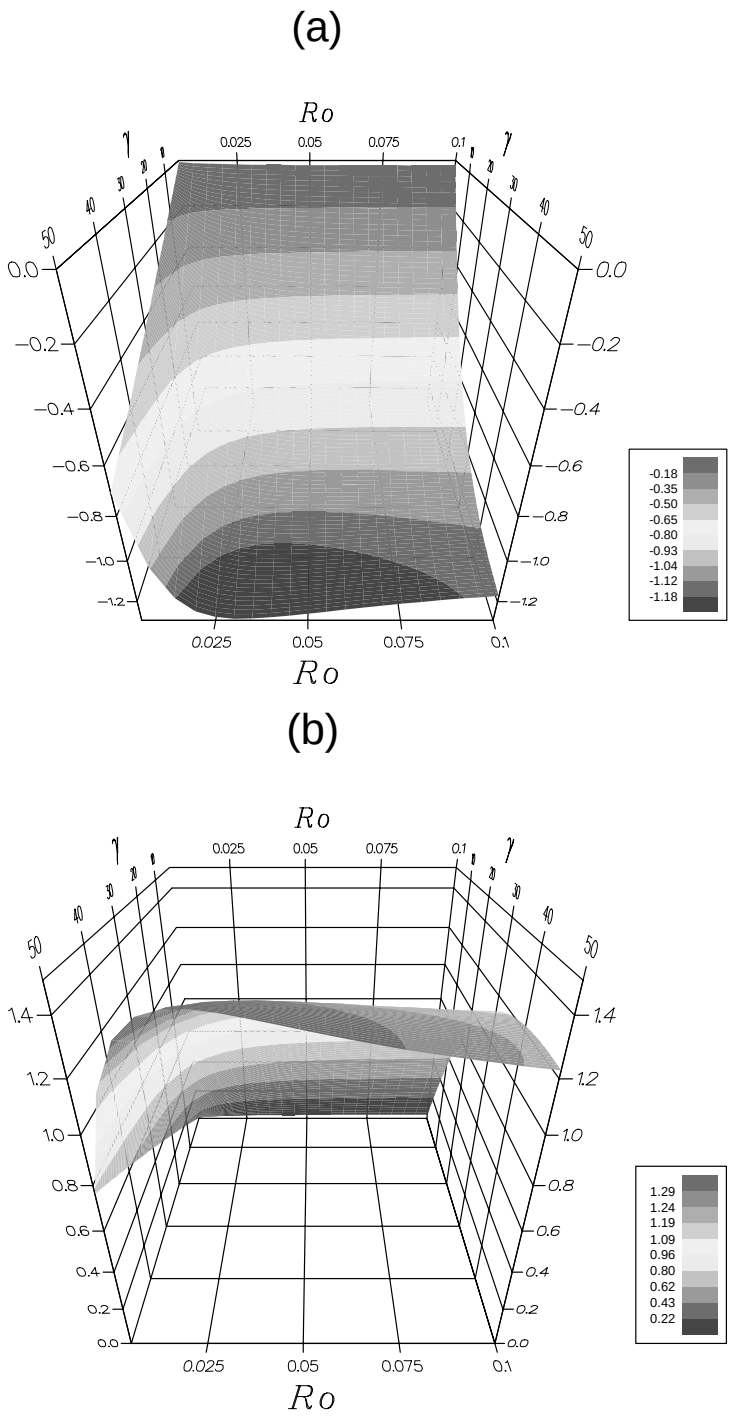

Figure 5.4: Plots of Re_M (maximum value of the real parts of the eigenvalues of system (5.11)) in the neighborhood of the centre of a Gaussian vortex for light and heavy impurities, as function of the Stokes parameter and the Rossby number. Panel (a) is for light impurities ($\delta = 1.2$) in a cyclone, panel (b) is for heavy impurities ($\delta = 0.8$) in a cyclone, panel (c) is for light impurities in an anticyclone and panel (d) is for heavy impurities in an anticyclone. In all the panels, $|\zeta_0| = 40$.

(c)

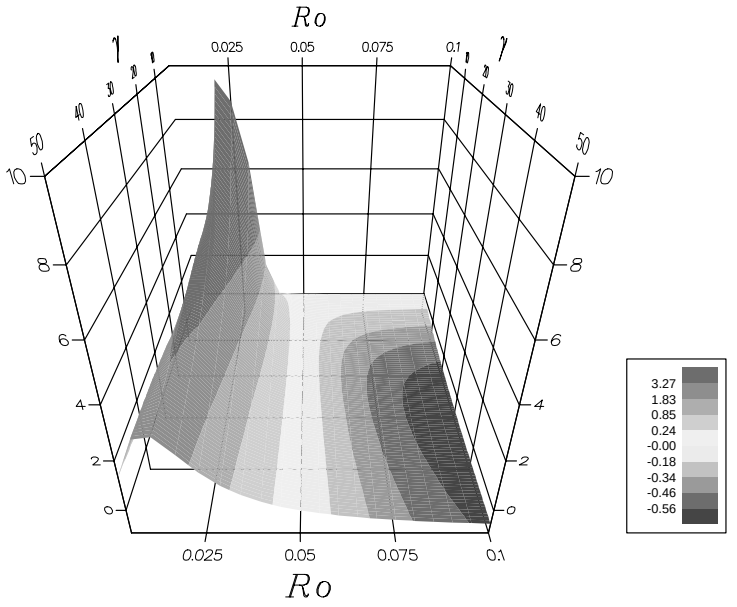

(d)

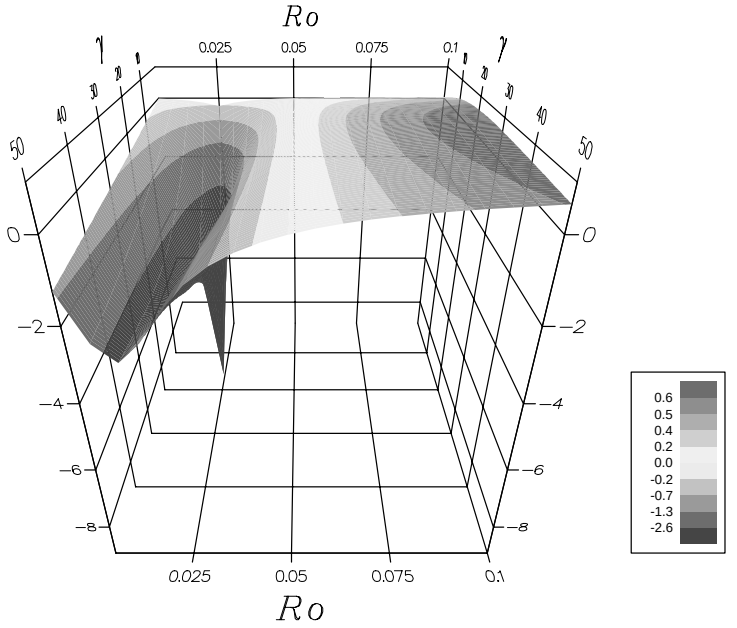

Figure 5.4: (continued)

$$\frac{d}{dt}\begin{pmatrix} X \\ Y \\ U \\ V \end{pmatrix} = \begin{pmatrix} 0 & 0 & 1 & 0 \\ 0 & 0 & 0 & 1 \\ -a\Delta\left(\varepsilon+2a\right) & -a\gamma & -\gamma & \Delta\left(\frac{a}{2}+\frac{\varepsilon}{\delta}\right) \\ a\gamma & -a\Delta\left(\varepsilon+2a\right) & -\Delta\left(\frac{a}{2}+\frac{\varepsilon}{\delta}\right) & -\gamma \end{pmatrix}\begin{pmatrix} X \\ Y \\ U \\ V \end{pmatrix} \tag{5.12}$$

It can be numerically verified that the critical value of the Rossby number occurs at $Ro = -1/2\psi_0$, such as in the previous case without the lift term. The plot of Re_M are very similar to the ones showed in figure 5.4.

5.3 Capture of impurities by vortices

Linear stability analysis applies rigorously only in a neighborhood of fixed points (the vortex centre in the case of the Gaussian vortex model). In practice, the results discussed in the previous section are valid inside vortex cores, far from the vortex edge.

For the study of transport of impurities in vortex-dominated flows, the dynamical behaviour out of vortex cores is important. Because of the presence of the extreme in the azimuthal velocity at vortex edge, nonlinear effects are introduced and capture or expulsion of impurities may change dramatically with respect to the results shown above.

Since linear analysis does not apply outside vortex cores, a different technique has to be used in order to explore the dynamics of light and heavy particles as a function of the governing parameters. One possibility is to write the equation of motion (4.4) in polar coordinates (r, θ), with the origin in the centre of a Gaussian vortex, and to analyze the trajectories of impurities in phase space.

The radial component of equation (4.4) (without considering the lift force) simply reads:

$$\frac{d^2R}{dt^2} = \frac{1}{R}\left[\left(R\frac{d\Theta}{dt}\right)^2 - \frac{3}{2}\Delta u_\theta^2\right] - \gamma\frac{dR}{dt} + \frac{\Delta}{\delta}Ro^{-1}\left(R\frac{d\Theta}{dt} - \delta u_\theta\right), \tag{5.13}$$

where u_θ is the Eulerian azimuthal velocity of the advective flow (which is provided, in the case analyzed here, by expression (5.5), while the radial velocity is equal to zero), R and Θ are respectively the radial and azimuthal components of the impurity position in polar plane, dR/dt and $R(d\Theta/dt)$ are its radial and azimuthal velocities.

A trajectory in phase space is given by the time evolution of the vector

$$\left(R(t), \Theta(t), \frac{dR}{dt}(t), \frac{d\Theta}{dt}(t)\right),$$

which at fixed time identifies the position of an impurity in phase space.

The projections of the impurity trajectories on the plane $\left(R, \frac{dR}{dt}\right)$ have particular importance, since impurities tend always to circle around the vortex centre, but are captured by (or ejected out of) vortex cores with different strenghts for different values of the governing parameters. In particular, I am interested in exploring the role of the Stokes parameter and the Rossby number in the process of capture of impurities by a vortex.

5.3.1 Capture of light impurities in non-rotating systems

If the density ratio δ is fixed, a simple analysis of the radial component (5.13) of the equation of motion for impurities (without the Coriolis force and the lift term), is useful to give a qualitative picture of the dynamics.

The first term in the r.h.s. of equation (5.13) gives always a centrifugal contribution, whereas the second term is always centripetal. The third term (which includes the Stokes parameter) gives a centrifugal contribution if the impurity approaches the vortex centre or a centripetal one if it is directed outwards, the larger is γ, the bigger the contribution. If we consider, for instance, a light impurity outside a Gaussian vortex, starting at the periphery of the circulation cell with the same velocity as the Eulerian velocity (thus, only azimuthal), the initial contribution is only given by $\left(1 - \frac{3}{2}\Delta\right)/R$, which is negative, thus centripetal. As time goes on, the term $-\gamma\frac{dR}{dt}$ increases (as absolute value), while the term u_θ^2/R becomes bigger as R decreases, up to the maximum at $R \cong 0.71$. If γ is small, the latter contribution, which is centripetal, may become prevalent and the impurity is easily captured by the vortex in a short time scale, with a nonnegligible centripetal acceleration. For large γ, the initial centripetal acceleration is immediately compensated by the centrifugal contribution given by $-\gamma\,\frac{dR}{dt}$, and the time scale of the fall of the impurity inside the vortex becomes very large.

More quantitatively, in figure 5.5, as an example, I plot the projections on the plane $\left(R, \frac{dR}{dt}\right)$ of the trajectories in phase space for a light particle with $\gamma = 5$ and a particle with $\gamma = 20$; the initial positions in phase space are given by the set $\left(R, \Theta, \frac{dR}{dt}, \frac{d\Theta}{dt}\right) = \left(1.75, 0, 0, \frac{u_\theta\,(1.75)}{1.75}\right)$, corresponding to a position inpolar plane at the pheriphery of the circulation cell (see figure 5.2). The trajectories in phase space are obtained as numerical solutions (for a total nondimensional time $T = 10$) of the system given by the equation for the radial component (5.13) and the corresponding equation for the azimuthal component of the impurity acceleration in a non-rotating reference frame.

The initial smaller centrifugal contribution given by the term $-\gamma\,\frac{dR}{dt}$ with $\gamma = 5$ allows the impurity to reach larger, negative radial velocity and to be strongly captured in a short time; during the same time, the light particle with $\gamma = 20$ does not go further than $R = 1.6$.

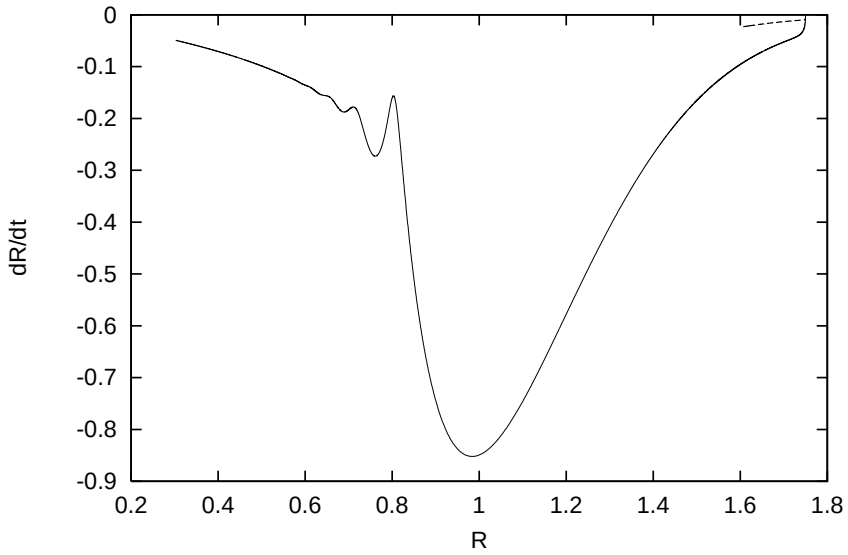

Figure 5.5: Trajectories on the plane $\left(R, \frac{dR}{dt}\right)$ of a light particle ($\delta = 1.2$) with $\gamma = 5$ and of a particle with $\gamma = 20$ for a Gaussian vortex with $\zeta_0 = 40$ (equation (5.5)). The initial positions in phase space are given by the set $\left(R, \Theta, \frac{dR}{dt}, \frac{d\Theta}{dt}\right) = \left(1.75, 0, 0, \frac{u_\theta(1.75)}{1.75}\right)$, corresponding to a position in polar plane at the pheriphery of the circulation cell, out of the coherent structure (see also figure 5.2). The solid line is for the impurity with $\gamma = 5$ while the dashed line is for the case $\gamma = 20$. The trajectories in phase space are numerically computed for a total nondimensional time $T = 10$.

Analogous results are obtained by using expression (5.7) for the Eulerian azimuthal velocity (Gaussian vortex with single-signed vorticity). The only difference is that, in this case, also large Stokes parameters allow light impurity to be captured in a shorter time scale (since initial azimuthal velocity is larger in the same initial, radial position) or, equivalently, the long tail of the azimuthal velocity allow light impurities with large γ to be captured even very far from the vortex core.

The same analysis performed for the capture of light impurities inside a vortex can be repeated for heavy particles outside a vortex core; in this latter case, the ejection of heavy impurities out of the circulation cells is favoured for small values of the Stokes parameter.

5.3.2 Capture of light and heavy impurities induced by the Coriolis force

In a rotating reference frame, two new terms appear in the radial component of the impurity acceleration, namely $\frac{\Delta}{\delta} Ro^{-1} R \frac{d\Theta}{dt}$, which gives a centrifugal contribution in a cyclone and a centripetal one in an anticyclone, and $-\Delta Ro^{-1} u_\theta$ which gives a contrary contribution. In the case in which $\delta \ll 1$, as pointed out by Tanga

et al. (1996), the only new important term is the former, which favours the capture of very heavy particles by anticyclonic vortices; if $\delta \gg 1$, the latter term favours the capture of very light impurities in cyclones. In all the intermediate cases, the equilibrium among the different terms in equation (5.13) determines the capture or expulsion of impurities, depending on the parameters. I will discuss here the role of the Rossby number in the process of capture of impurities in cyclones and anticyclones, if δ and γ are fixed.

To do that, I show in figures 5.6 and 5.7 the projections on the plane $\left(R, \frac{dR}{dt}\right)$ of the trajectories in phase space for a light particle ($\delta = 1.2, \gamma = 5$) with $Ro = 0.1$ or $Ro = 0.02$, which starts outside a cyclonic Gaussian vortex with $\psi_0 = 10$, and an heavy impurity ($\delta = 0.8$, $\gamma = 5$) which starts outside an anticyclonic vortex (the initial positions in phase space are the same as in the non-rotating case). As one can see in figure 5.6 for the case of light impurities in a cyclone, the particles are captured by the vortex both if the rotation of the system is strong ($Ro = 0.02$) and if it is weaker ($Ro = 0.1$); anyway, a weak rotation favours the capture of light impurities in cyclonic vortices, since the initial damped oscillations in the radial velocity for the case with $Ro = 0.02$ (strong rotation) lead to a smaller velocity for the fall inside the vortex, thus to a longer capture time scale.

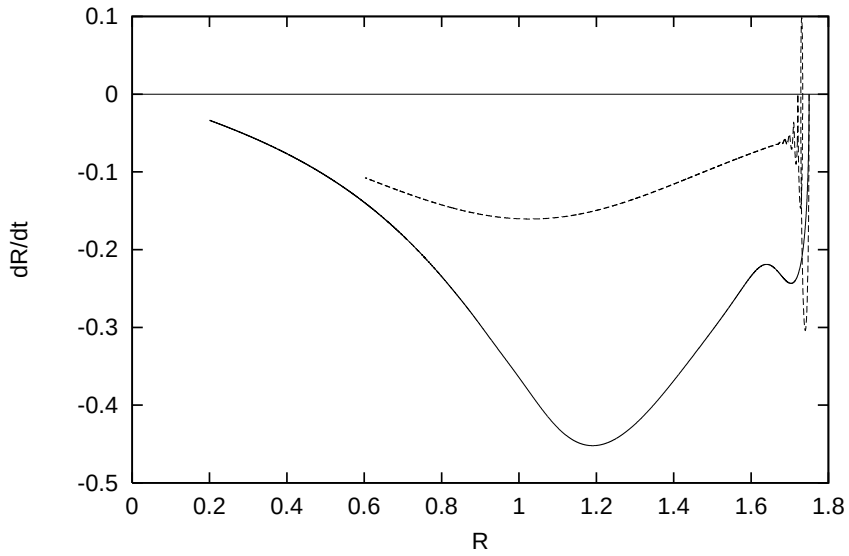

Figure 5.6: Trajectories on the plane $\left(R, \frac{dR}{dt}\right)$ of a light particle ($\delta = 1.2, \gamma = 5$) with $Ro = 0.1$ (solid line) and of a particle with $Ro = 0.02$ (dashed line) for the same cyclonic Gaussian vortex of figure 5.5. The initial positions in phase space are the same as in figure 5.5. The total nondimensional time of the computation of the trajectories in phase space is $T = 10$.

The situation changes for the case of heavy impurities in an anticyclonic vortex: a strong rotation ($Ro = 0.02$) leads to the fast capture of the heavy impurity, which reaches the center of the anticyclone in a finite time. On the contrary, in the case of

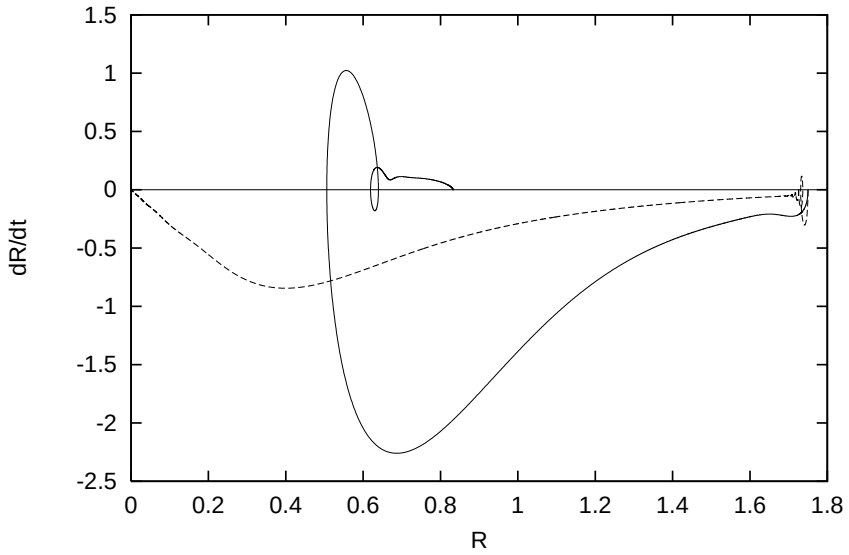

Figure 5.7: Same as in figure 5.6, but for an heavy impurity ($\delta = 0.8$, $\gamma = 5$) in an anticyclonic Gaussian vortex. The solid line is for the case with $Ro = 0.1$, the dashed line is for $Ro = 0.02$

weaker rotation ($Ro = 0.1$), the particle is initially attracted into the anticyclone up to a distance from the centre $R = 0.5$, but it is then expelled out of the vortex core, as the results given by the linear stability analysis predict. The heavy impurity is then attracted toward an equilibrium distance far from the vortex centre in which the centripetal and centrifugal forces equilibrate.

This situation corresponds in phase space to a limit cycle, described by the condition

$$\left(R, \Theta, \frac{dR}{dt}, \frac{d\Theta}{dt}\right) = \left(R_{eq}, \Theta, 0, \frac{u_\theta\left(R_{eq}\right)}{R_{eq}}\right), \tag{5.14}$$

where R_{eq} is the equilibrium distance far from the anticyclonic centre. The expression for R_{eq} is easily found by inserting in equation (5.13) the values which describes the limit cycle in phase space and by using the expression (5.5) for the azimuthal velocity. This yields:

$$R_{eq} = \sqrt{-\ln\left(-\frac{Ro^{-1}}{2\psi_0}\right)}. \tag{5.15}$$

It is clear that there is an equilibrium distance only for an anticyclonic vortex ($\psi_0 < 0$), when $Ro > -1/2\psi_0$. This is perfectly in accordance with the fact that for $Ro > -1/2\psi_0$ the anticyclonic centre is an unstable point for heavy particles, while these ones are anyhow attracted into the vortex, if they start outside.

The closed orbit in phase space, described by vector (5.14), is a stable attractor for heavy impurities in anticyclones. In the limit $Ro \to \infty$, thus in a non-rotating reference frame, one recovers the result found above: heavy impurities do not enter

any vortex, neither cyclonic nor anticyclonic, since the resulting equilibrium distance is infinite. Furthermore, since the expression for R_{eq} does not depend on δ, it is also valid for light particles in anticyclones. In this case, R_{eq} is an equilibrium distance at which centrifugal and centripetal forces cancel out, but it is not an attractor orbit in phase space: if $R < R_{eq}$, in fact, light particles are attracted toward the centre of the anticyclone (as seen by using linear stability analysis) and for $R > R_{eq}$ they are ejected out of the vortex. In the limit $Ro \to \infty$, light impurities are attracted into a cyclonic vortex from infinity.

Note also that expression (5.15) does not depend on the Stokes parameter, thus the equilibrium distance is the same for different sizes of the impurities or different Reynolds numbers.

5.3.3 The role of the lift force

The introduction of lift force, written in polar coordinates for a Gaussian vortex, yields a new term in equation (5.13) for the radial component of the impurity acceleration: $\frac{\Delta}{2}\left(R\frac{d\Theta}{dt} - u_\theta\right)\zeta$. This term leads to centrifugal or centripetal contributions to the radial acceleration which are formally similar to that produced by the Coriolis term. Indeed, the importance of the lift term contribution is greater where vorticity is larger, thus more inside vortex core than outside. Therefore, lift force does not change substantially the dynamics of capture of impurities by vortices in a rotating system.

Also the expression for the equilibrium distance R_{eq} is not modified by the presence of the lift term, since in a limit cycle described by condition (5.14), this term vanishes. The only remarkable effect concerns the dynamical behaviour of heavy impurities which enter an anticyclonic core when the Rossby number is small: trajectories in the plane $(R, dR/dt)$ reach a certain distance from the centre, then they make for outwards, but no equilibrium distance is present in the system, and finally the centripetal contribution becomes predominant and the particle falls towards the vortex centre (see figure 5.8).

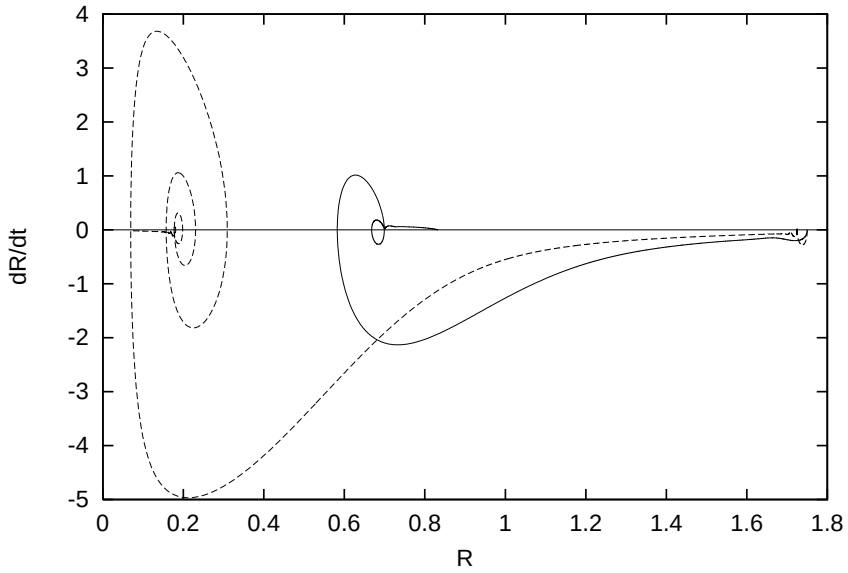

Figure 5.8: Same as in figure 5.7, with the addition of the lift term. The solid line is for the case with $Ro = 0.1$ and the dashed line corresponds to $Ro = 0.03$

Chapter 6

Dynamics of impurities in barotropic turbulence

The dynamics of impurities is numerically studied in a barotropic, two-dimensional fluid model, and the contributions given by the different terms in the equation of motion are separately taken into account. The results obtained in analytical, stationary flows are used to explain the behaviours of light and heavy impurities when the turbulent flow is dominated by coherent vortices.

6.1 Impurities advected by a two-dimensional turbulent flow

The results on impurity dynamics obtained in previous chapter by using simple, analytical vortex models, are precious to explain most of the dynamics of light and heavy particles in more complex, vortex-dominated turbulent flows, such as barotropic ones.

One of the most relevant differences between coherent vortices in barotropic turbulence and the Gaussian vortex model is that "real" vortices may have radial velocity (since they are not perfectly circular). Another difference is the fact that coherent vortices are not isolated and interact with each other; dynamics of impurities during vortex-vortex interactions (straining, coupling and merging processes) has not been taken into account in the previous chapter.

In the following, I will consider the impurity dynamics in a two-dimensional advecting turbulent flow, whose dynamics has been widely discussed previously. Results in a quasi-geostrophic or shallow-water approximation depend more on the different dynamics of the advecting flow itself, than on the dynamical behaviour of impurities in the presence of vortices.

The dynamics of light and heavy particles (as well as the dynamics of neutrally buoyant tracers in the next chapter) in 2D turbulence is studied by means of numerical simulations, whose set-up is described in chapter 4. The impurities have a density difference no larger than 25% with respect to the fluid: I use $\delta = 1.2$ for light particles (less dense than the fluid) and $\delta = 0.8$ for heavy particles (denser than the fluid).

6.2 Dynamics of impurities in non-rotating reference frames

In order to analyze separately in section 6.3 the effects on the impurity dynamics introduced by the Coriolis force in a rotating reference frame, I deal in this section with the simpler case in a non-rotating system, by using the following nondimensional equation of motion:

$$\frac{d^2\mathbf{X}}{dt} = \Delta \frac{D\mathbf{u}}{Dt} - \gamma \left(\frac{d\mathbf{X}}{dt} - \mathbf{u} \right) + \frac{1}{2}\Delta \frac{d\mathbf{u}}{dt}. \tag{6.1}$$

Figure 6.1 show typical trajectories of, respectively, a light impurity and an heavy impurity initially placed inside the core of an anticyclonic vortex. Impurities less dense than the fluid are attracted by vortex centres and undergo spiral trajectories around and toward them, whereas heavy impurities undergo spiral trajectories outwards, leaving the vortex cores devoid of particles.

The result at late times is a nonhomogeneous distribution of particles throughout the turbulent field, with high concentrations of light particles and lack of heavy particles inside vortices, as one can see in figure 6.2, which shows the distribution

of 4096 light impurities (panel a) and heavy impurities (panel b) with $\gamma = 5$ in the turbulent field at time $t = 33$ (depicted in figure 1.3).

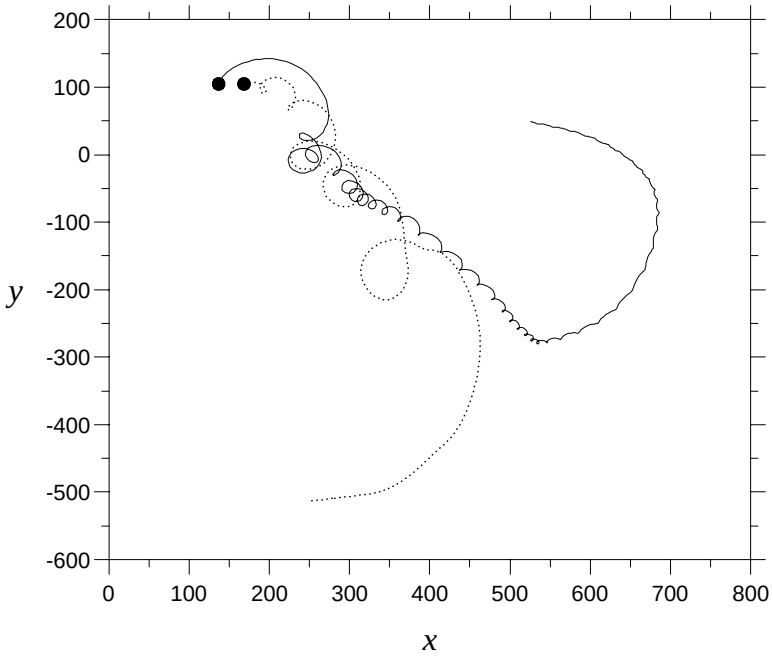

Figure 6.1: Typical trajectories of a light impurity with $\delta = 1.2$, $\gamma = 5$ (solid line) and a heavy impurity with $\delta = 0.8$, $\gamma = 5$ (dotted line) inside the core of a (cyclonic) coherent vortex. The initial velocities are the Eulerian velocities at the corresponding initial positions. In figure, units are the grid points; one has to multiply by $2\pi/512$ in order to have radiants.

At fixed δ, moreover, the *capture time* of light particles (namely, the time taken to reach the vortex centre, starting inside the core) and the *expulsion time* of heavy particles (namely, the time taken to leave the vortex core, starting close to the centre) depend on the value of the Stokes parameter γ, as figure 6.3 shows. In this figure, the capture time for light impurities (solid line) is evaluated by using the mean time taken by twelve particles with $\delta = 1.2$ and different γ to reach a distance from the centre of an antyciclonic vortex corresponding to 80% of the maximum vorticity, starting from a position from the centre that is associated with 10% of the maximum vorticity, whereas the expulsion time (dashed line) is evaluated for twelve particles with $\delta = 0.8$ that reach a distance far from the centre which corresponds to 10% of the maximum vorticity, starting from a position around the centre in which the vorticity is 80% of its maximum value. The anticyclonic vortex that is used has a well definite, quasi-circular shape and does not interact much with the others during the numerical experiments. Capture time and expulsion time curves show the same dependance from γ, with a minimum around $\gamma \cong 20$ and asymptotic behaviours for small and large γ given respectively by $\frac{1}{\gamma}$ and γ (see the inset of figure 6.3 in logarithmic scale).

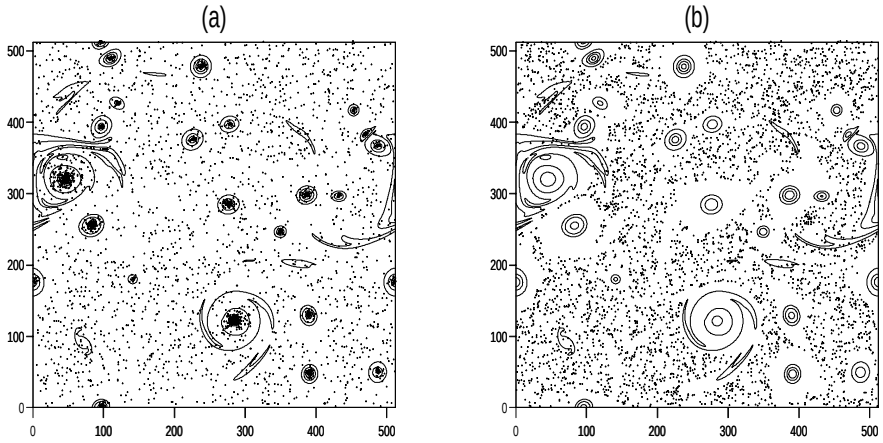

Figure 6.2: Distributions of 4096 light impurities with $\delta = 1.2$, $\gamma = 5$ (panel a) and 4096 heavy impurities with $\delta = 0.8$, $\gamma = 5$ (panel b) at time $t_f = 33$. The initial distributions are uniform, with initial velocities equal to the Eulerian velocities at the corresponding positions. In each panel the isolines of the vorticity field are superimposed, showing the well developed coherent structures (see also figure 1.3b). Units are the grid points (one has to multiply by $2\pi/512$ in order to convert into radiants

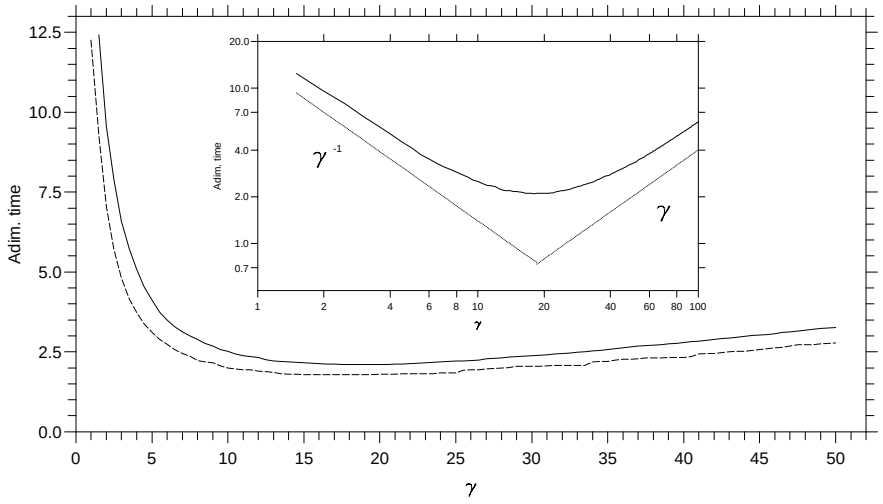

Figure 6.3: In this figure the continuous line represents the mean *capture time* of 12 light impurities ($\delta = 1.2$) toward the center of an anticyclonic vortex versus γ, whereas the dashed line represents the mean *expulsion time* of 12 heavy impurities ($\delta = 0.8$) out of the same anticyclonic vortex. The chosen vortex has a well defined quasi-circular shape and does not interact much with the others. The impurities are initially seeded equally spaced on a circle around the vortex center, with initial velocities equal to Eulerian velocities. The procedure of evaluation of the capture and the expulsion times is described in the text. In the inset, the scale is logarithmic for the capture time curve, and the dashed lines are proportional to $1/\gamma$ and γ.

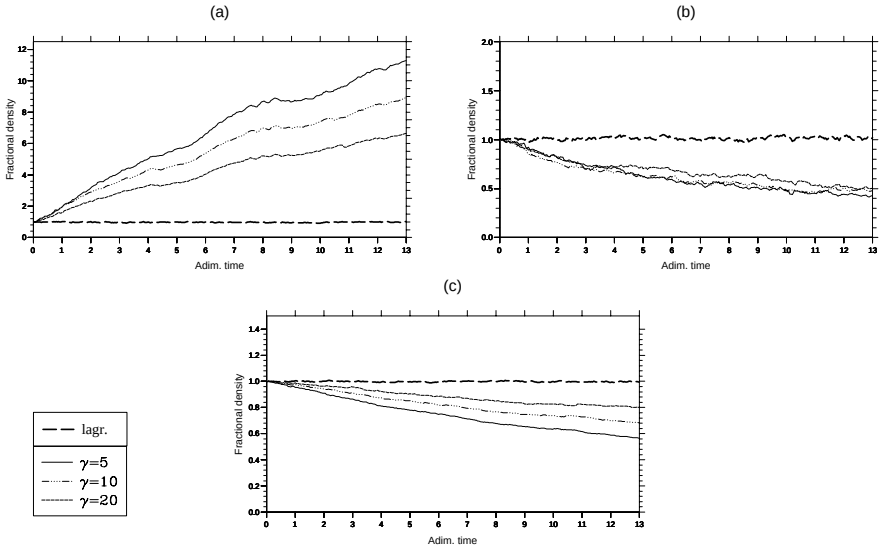

Figure 6.4: Time evolution of the fractional density $d = (N/N_{tot}) / (A/A_{tot}) = (N/A) \cdot (4\pi^2/4096)$ of 4096 light impurities ($\delta = 1.2$) in areas occupied by: (a) coherent vortices, (b) circulation cells, (c) turbulent background. The different curves are for different values of γ and for Lagrangian particles. The initial conditions for impurities are the same as in figure 6.2. Areas occupied by vortices are distinguished from the background by the values $Q \leq 0$ and vorticity $\zeta > 5$, whereas circulation cells are distinguished either by $Q > 20$ or by $Q > 0$ and $\zeta > 3$. These choices let a very good distinction among the three areas (vortices, circulation cells, background turbulence) for these experiments.

All these properties are completely in accordance with the results given by the linear stability analysis performed, in previous chapter, in the neighborhood of a Gaussian vortex centre and confirm that the dynamics of impurities inside vortex cores may be well explained by linear theory.

Vortices in two-dimensional turbulence are anyhow complex structures and the dynamics of impurities outside vortex cores can be explained only by referring to nonlinear effects. If one looks at figure 6.4, which shows the time evolution of the fractional density of light impurities $d = (N/N_{tot}) / (A/A_{tot}) = (N/A) \cdot (4\pi^2/4096)$, where N is the number of impurities in the area A of the turbulent field occupied by vortex cores (panel a), by circulation cells (panel b) or by the turbulent background (panel c), and defined by using the Okubo-Weiss criterion, two properties are evident:

1. light particles tend to concentrate inside vortex cores also at late times, coming from the turbulent background (the density in circulation cells, in fact, diminuishes such as in the background) and disregarding the barrier constituted by the strong vorticity gradients at the edge of vortex cores, unlike Lagrangian particles;

2. the concentration of light particles inside vortex cores depends inversely on

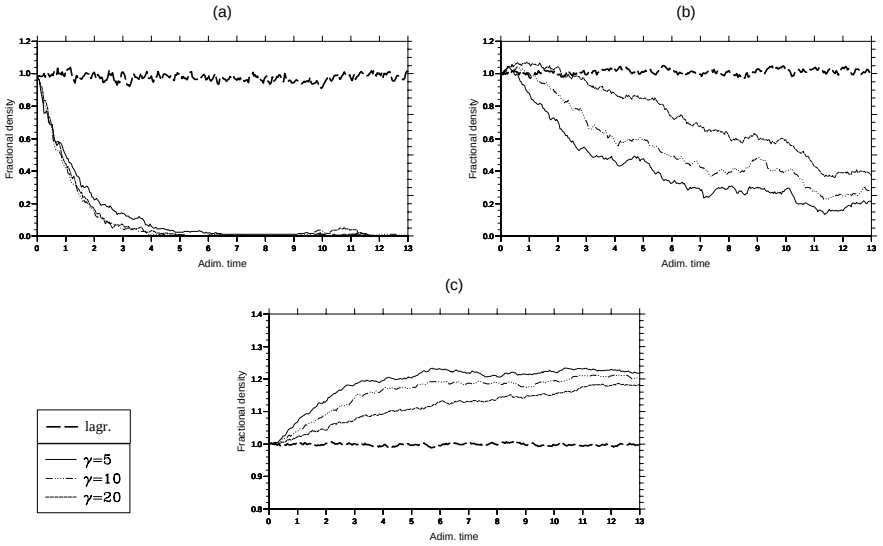

Figure 6.5: Time evolution of the fractional density $d = (N/N_{tot}) / (A/A_{tot}) = (N/A) \cdot (4\pi^2/4096)$ of 4096 heavy impurities ($\delta = 0.8$) in areas occupied by: (a) coherent vortices, (b) circulation cells, (c) turbulent background. The different curves are for different values of γ and for Lagrangian particles. The initial conditions for particles are the same as in figure 6.2. The criterion to distinguish vortices and cells from the background is the same as in figure 6.4.

γ: small values of the Stokes parameter favour the capture by vortices of light impurities moving in the background.

The effect of these properties is that, if on the one hand it might be possible to observe light particles with large γ very close to the centre of vortices already at short times, on the other hand one observes fewer light impurities inside coherent vortices if γ is large, also at late times. The latter effect cannot be explained neither with a linear theory, nor with the simple argument that, for very large γ, the most important term in the equation (6.1) is the difference $d\mathbf{X}/\mathbf{dt} - \mathbf{u}$ and the impurities move as Lagrangian particles, which is not valid for intermediate Stokes parameters. The explanation of this effect is given by the analysis of the trajectories of light impurities with different γ in the phase space, performed in previous chapter: the smaller net centripetal force which characterizes light particles with large Stokes parameters at the pheriphery of coherent structures may easily be contrasted by the background turbulence, allowing such impurities not to be captured.

The same consideration may be repeated for heavy impurities outside a vortex core: in this case, the expulsion of such impurities out of the circulation cells is favoured for small values of the Stokes parameter, and the result in the different partitions of the two-dimensional turbulent field can be seen in figure 6.5, where I plot the fractional density versus time for heavy impurities with different γ.

6.3 The effects of the Coriolis force

The introduction of the Coriolis term $-\frac{\Delta}{\delta} Ro^{-1} \mathcal{Z} \times \left(\frac{d\mathbf{X}}{dt} - \delta \mathbf{u} \right)$ in the equation for impurities in a rotating reference frame changes deeply the dynamics, leading to an asymmetry cyclone-anticyclone with respect to the capture or expulsion of light and heavy impurities by vortices, as predicted in previous chapter for the case of a Gaussian vortex.

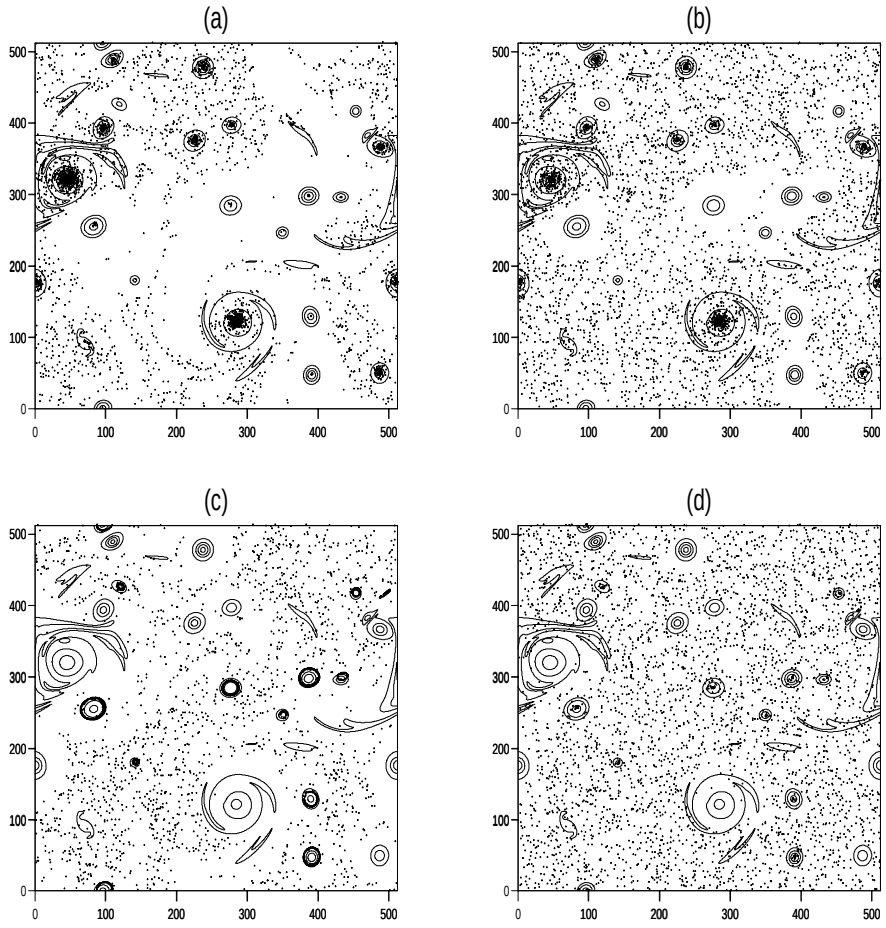

Figure 6.6: Distributions of 4096 heavy impurities ($\delta = 0.8$) and light impurities ($\delta = 1.2$) with different values of Rossby number and $\gamma = 5$ in a turbulent field: (a) $\delta = 1.2$, $Ro = 0.1$, (b) $\delta = 1.2$, $Ro = 0.02$, (c) $\delta = 0.8$, $Ro = 0.1$, (d) $\delta = 0.8$, $Ro = 0.02$. These distributions are given at $t = 33$ and the initial distributions are uniform, with initial velocities equal to the Eulerian velocities at the corresponding positions. In each panel the isolines of the vorticity field are superimposed. Units are the grid points.

The results discussed so far allow to explain the details of the dynamics of light and heavy impurities in the two-dimensional, rotating system described by equation (4.4), without considering the lift term. I have performed numerical ex-

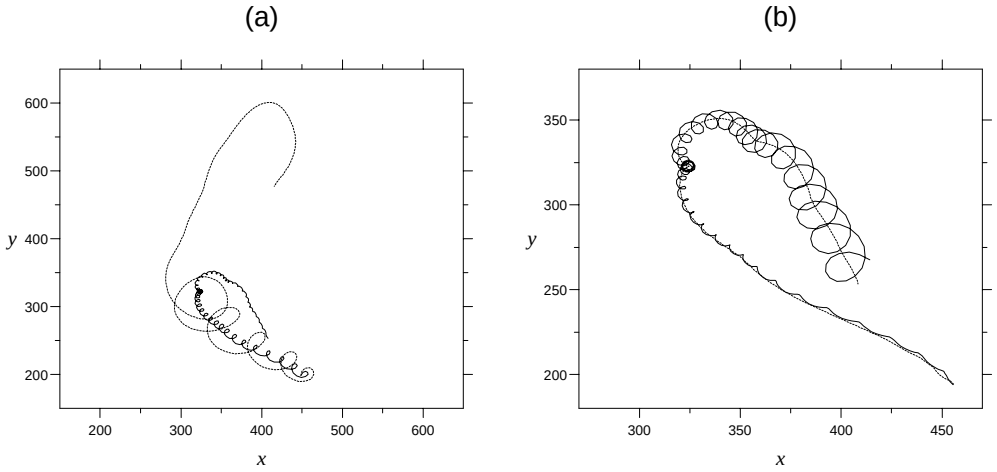

Figure 6.7: Trajectories of a light impurity with $\delta = 1.2$, $\gamma = 5$ (panel a) and an heavy impurity with $\delta = 0.8$, $\gamma = 5$ (panel b) inside the core of the same anticyclonic vortex. The solid lines are for $Ro = 0.1$ and the dashed lines are for the case with $Ro = 0.02$. The initial velocities are the Eulerian velocities at the corresponding initial positions.

periments by using 4096 light impurities ($\delta = 1.2$) and heavy impurities ($\delta = 0.8$) with a fixed $\gamma = 5$ and Rossby numbers $Ro = 0.1, 0.02$. The distributions of impurities in the turbulent field at time $t = 33$ (figure 6.6) reflect the analytical and numerical results obtained in the stationary case by using an isolated vortex: in general, light impurities concentrate inside cyclonic vortices and are expelled out of anticyclonic ones, and the contrary happens for heavy impurities.

By looking at details, for the case with $Ro = 0.1$ one can appreciate that there are some light particles very close to the center of anticyclonic vortices whereas there are no heavy particles very close to these centers; this apparent paradox is well explained by the fact that the anticyclones are characterized by the critical value $Ro = -2/\zeta_0$ and that for $Ro > -2/\zeta_0$ the anticyclonic centers become unstable for heavy particles and stable for light ones. Therefore, impurities that are seeded initially inside anticyclonic cores with a vorticity in the centre that is greater than 20, for the case with $Ro = 0.1$, undergo typical centerward (light particles) or outward trajectories (heavy particles) as figure 6.7 shows.

This behaviour inside anticyclonic vortices is also confirmed by the mean capture time plotted for 12 heavy impurities in figure 6.8a, for different Stokes parameters and Rossby numbers; it is evident that for $Ro \approx 0.06$ the capture time has a strong growth for all the values of γ, which is compatible with the critical value of the Rossby number for the anticyclonic vortex used in this experiment, which has a mean vorticity in the centre $\overline{\zeta_0} \approx -38$ (the mean is calculated for the temporal range $20 < t < 33$). Also the presence of the minima in the capture time plot for heavy impurities and for light ones (in figure 6.8b) is predicted by the linear stability analysis around the vortex centre, as shown by Re_M in figure 5.4.

(a)

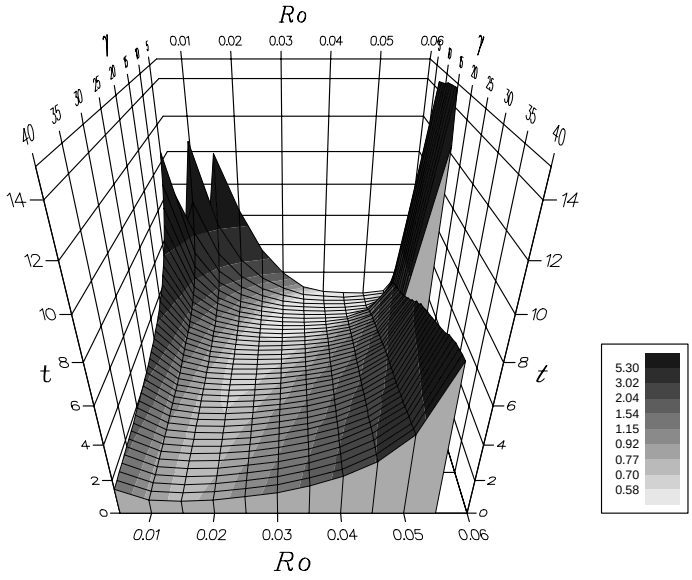

(b)

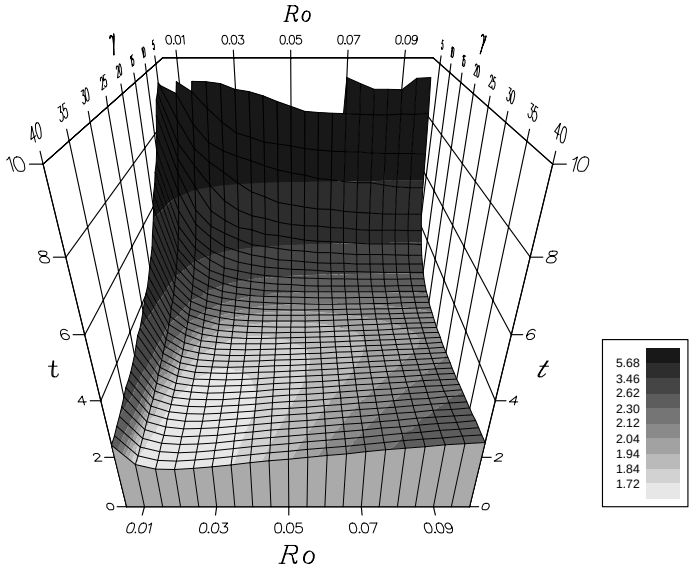

Figure 6.8: Panel (a) of this figure is the *capture time* towards the center of an anticyclonic vortex for heavy impurities, as function of γ and the Rossby number. The chosen vortex is the same as in figure 6.3, as well as the time evaluation procedure. Panel (b) represents the *capture time* towards the center of a cyclonic vortex versus γ and the Rossby number for light impurities. In this latter case, the chosen cyclonic vortex does not interact much with the others, and the time evaluation procedure is the same as in panel (a).

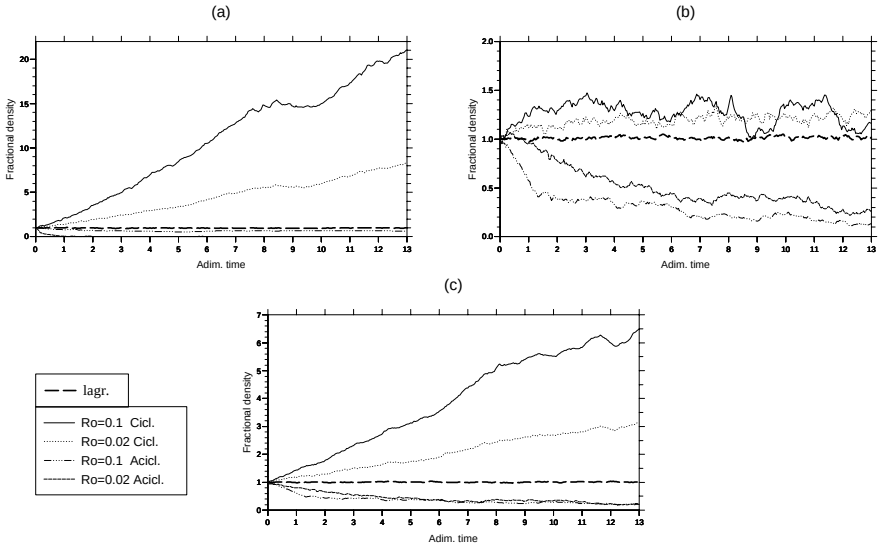

Figure 6.9: Time evolution of the fractional density $d = (N/N_{tot}) / (A/A_{tot}) = (N/A) \cdot \left(4\pi^2/4096\right)$ of 4096 light impurities ($\delta = 1.2$) with $\gamma = 5$ in areas occupied by: (a) coherent cyclone and anticyclone vortices, (b) cyclone and anticyclone circulation cells, (c) turbulent background. The initial impurities distribution is uniform and the initial velocities are equal to the Eulerian velocities. Areas occupied by vortices are distinguished from the background by the values $Q \leq 0$ and vorticity $\zeta > 5$, whereas circulation cells are distinguished either by $Q > 20$ or by $Q > 0$ and $\zeta > 3$. Cyclones and anticyclones are distinguished by the positive or negative value of vorticity.

The fact that a slow rotation of the reference frame favours the capture of light impurities inside cyclonic vortices and of heavy impurities inside anticyclonic ones, as seen by using the analytical model of the Gaussian vortex, shows its fingerprint in two-dimensional turbulence, as the fractional density of light and heavy particles inside cyclones and anticyclones points out in figures 6.9 and 6.10. Cyclones always attract light impurities coming from the turbulent background, but a larger density is reached when $Ro = 0.1$ with respect to the case with $Ro = 0.02$ (in the former case, the density is three times than that in the latter case). The analogous situation occurs for heavy impurities in anticyclones, except that anticyclonic cores are repulsive for $Ro > -2/\zeta_0$. This situation leads to concentration of heavy particles with $Ro = 0.1$ on stable orbits at a certain distance from the centre of anticyclonic vortices, as it is clear if looking at figure 6.6c. The fingerprint of the limit cycle is also given by the oscillations of the density of heavy particles with $Ro = 0.1$ in anticyclonic cores and circulation cells in figure 6.10.

Due to the fact that coherent structures in barotropic turbulence are neither perfectly circular nor isolated, we cannot speak about an unique equilibrium distance, but rather about a narrow *equilibrium range*, whose mean value can be evaluated by using expression (5.15). In the case of the quasi-isolated anticyclonic vortex already mentioned and used for the determination of the capture and expulsion times,

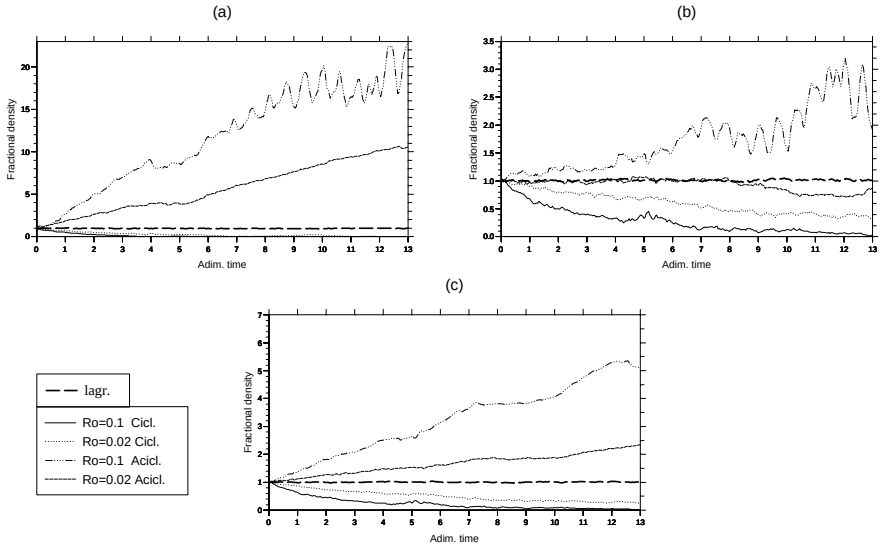

Figure 6.10: Time evolution of the fractional density of 4096 heavy impurities ($\delta = 0.8$) with $\gamma =$ 5 in areas occupied by: (a) coherent cyclone and anticyclone vortices, (b) cyclone and anticyclone circulation cells, (c) turbulent background.

in figure 6.11a I plot the distribution of heavy impurities with $Ro = 0.1$ at time $t = 33$, where the presence of an attractive line for the particle is evident.

It is convenient to use a reference frame centred in the vortex centre, in order to evaluate the radial distance and the radial velocity of the impurities. By plotting the projection on the plane $\left(R, \frac{dR}{dt}\right)$ of the positions in phase space for heavy impurities (figure 6.11b), it can be seen that the stable attractor, whose projection is represented by a simple point in the Gaussian vortex model, is here more complicated, due to the presence of nonnegligible radial velocities in the Eulerian field induced by the barotropic vortex. Anyhow, an equilibrium range is recognizable for $11.72 < R < 14.72$ grid points, with a mean value $\overline{R} = 13.35$ grid points and a standard deviation $\sigma_{\overline{R}} = 0.79$ grid points (calculated for all the impurities which lies on the attractor). If we scale the distance from the centre, by using a length scale given by the mean value (with respect to the azimuthal angle) of the scales $L_\theta = \sqrt{2} R \mid_{Q=0}$, where $R \mid_{Q=0}$ is the distance of the edge of the vortex core (at which the Q-value is zero), the nondimensional range is $0.67 < R' < 0.84$ and the mean value becomes $\overline{R'} = 0.76$, with a standard deviation $\sigma_{\overline{R'}} = 0.04$. By using the analytical expression (5.15) with the mean value $\overline{\zeta_0} \approx -38$ for the vorticity in the centre of the anticyclonic vortex, it comes out that $R_{eq} \approx 0.80$, which is compatible with the mean value of the equilibrium range.

Similar results are obtained by using heavy particles with $\gamma = 10$, although the attractor changes slightly its form (see figure 6.12). Nevertheless, the equilibrium range does not change a lot, confirming its independence of it from the value of the

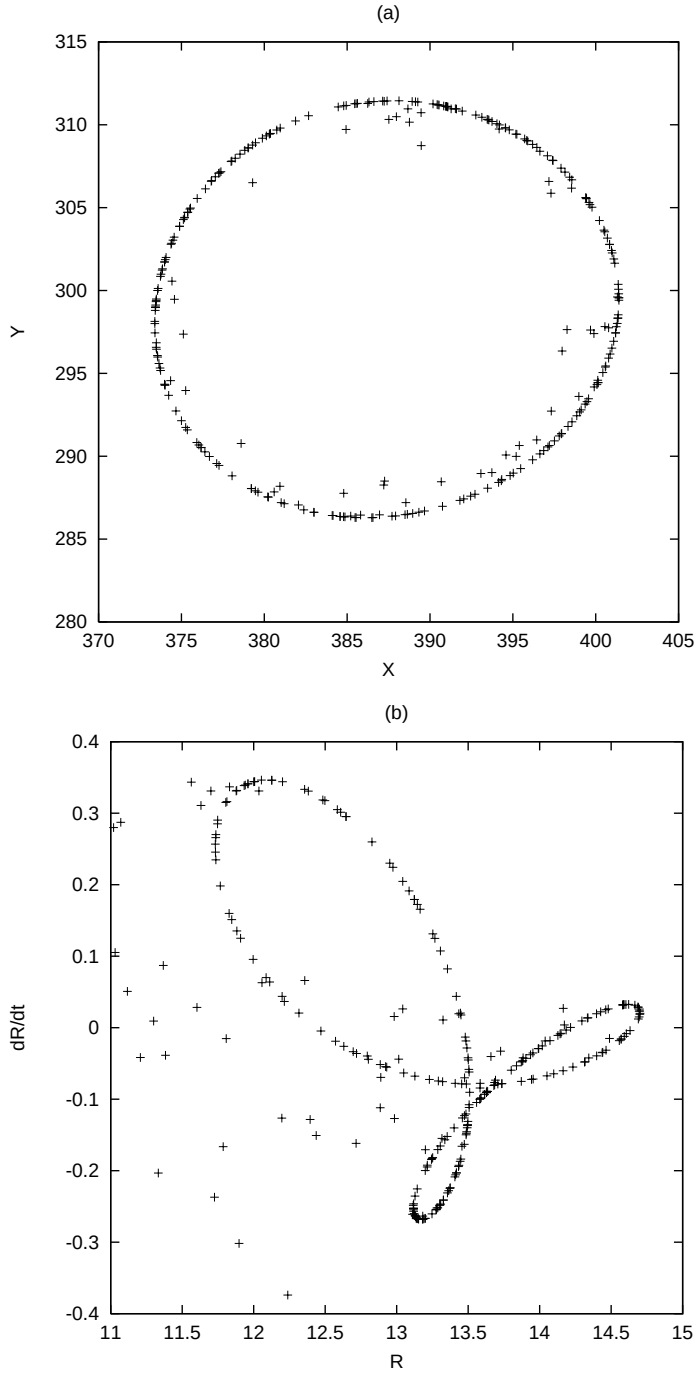

Figure 6.11: Panel (a): positions (in grid points) occupied at time $t = 33$ by heavy impurities with $\delta = 0.8$, $\gamma = 5$ and $Ro = 0.1$ in a anticyclonic vortex with the centre in (387,298) grid points. By using a reference frame centered in this position, panel (b) shows the projection on the plane $\left(R, \frac{dR}{dt}\right)$ of the positions occupied by the impurities in phase space, where an attractor is shown to concentrate the particles in the equilibrium range $11.72 < R < 14.72$ grid points.

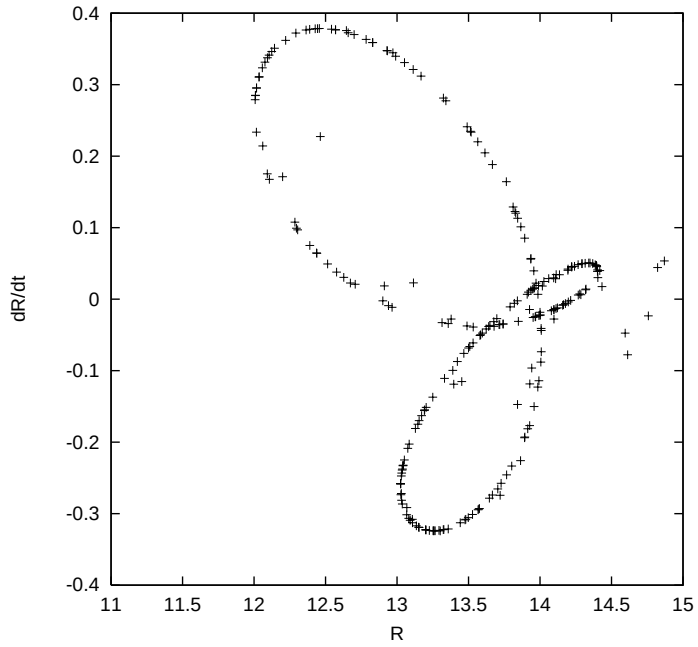

Figure 6.12: Plot of the projection on the plane $\left(R, \frac{dR}{dt}\right)$ of the positions occupied by heavy impurities with $\gamma = 10$ in phase space. The attractor is very similar to the one represented in figure 6.11b, as well as the equilibrium range $11.72 < R < 14.72$ grid points.

Stokes parameter, as predicted by equation (5.15).

6.3.1 The role of the lift force

It has been verified with the Gaussian vortex model that lift force does not change significantly the dynamics of impurities, except for some effects inside the anticyclonic cores, where the vorticity is larger. These effect are strictly limited to the cores, and no significant variations in the impurity densities inside cores and circulation cells can be appreciated. Not even the distributions of impurities in the turbulent field change with respect to the case wihout the lift term.

Chapter 7

The case of neutrally buoyant tracers with finite size

This chapter is devoted to the analysis of the dynamics of real tracers, neutrally buoyant but with finite size. It is pointed out that inertia can play an important role in the dynamics of such tracers, generating significant differences with respect to the dynamics of ideal fluid particles, and possibly introducing biasses in the Lagrangian statistics.

7.1 Floats, balloons and laboratory tracers

In experimental fluid dynamics, tracers are fundamental elements for the study of Lagrangian properties of a flow, as well as for the possible reconstruction of Eulerian velocity fields.

In laboratory experiments, microscopic particles are used to study the transport and dispersion properties of a turbulent flow or to get velocity information over a small portion of the fluid (Particle Image Velocimetry); in-situ experiments use floats and drifters in oceans and isopycnal balloons in atmosphere in order to reconstruct the dynamics of geophysical flows.

In all the examples above, tracers that are used are assimilated to fluid elements and their dynamics is considered "Lagrangian", i.e., their equation of motion is simply given by $d\mathbf{X}/dt = \mathbf{u}$, where $\mathbf{u}$ is the advecting Eulerian velocity. Fluid elements, however, are point-like particles, whereas real tracers have finite size. Also if they are perfectly neutral buoyants, because of their finite size (although small with respect to the flow length scale), their dynamics is rigorously described by the equation of motion for impurities (4.4), in which one has to put $\delta = 1$.

In this context, the dynamics of real tracers and, more in general, the dynamics of neutral buoyants with finite size, may be different from the fluid element dynamics, and possible biassed estimates of Lagrangian statistics may thus be introduced when data coming from tracers in laboratory or in-situ experiments are used. Furthermore, these data may lead to a misleading reconstruction of the Eulerian characteristics of a flow, which is added to the intrinsic difficulty to link the Lagrangian and Eulerian descriptions due to the chaotic advection which is present also in very simple flows (Aref 1984, Aref & Balachandar 1986, Falcioni et al. 1988).

In this chapter, I discuss the dynamics of neutrally buoyant particles ($\delta = 1$), advected by vortex-dominated flows. I will show as, also for neutrally buoyant tracers, the presence of vortices modifies the dynamics and the overall transport properties. First of all, the dynamics in a Gaussian vortex model is considered, afterwards the dynamics in two-dimensional turbulence will be discussed. Possible biasses in the statistics with respect to Lagrangian particles will be finally taken into account.

7.2 Dynamics of finite-size tracers in a Gaussian vortex

When the density ratio $\delta = 1$ is used into equation (4.4), the equation of motion reduces to:

$$\begin{aligned}\frac{d^2\mathbf{X}}{dt^2} &= \frac{2}{3}\frac{D\mathbf{u}}{Dt} - \gamma\left(\frac{d\mathbf{X}}{dt} - \mathbf{u}\right) + \frac{1}{3}\frac{d\mathbf{u}}{dt} \\ &\quad -\frac{2}{3}Ro^{-1}\mathcal{Z}\times\left(\frac{d\mathbf{X}}{dt} - \mathbf{u}\right) + \frac{1}{3}\left(\frac{d\mathbf{X}}{dt} - \mathbf{u}\right)\times\omega, \qquad (7.1)\end{aligned}$$

where the Stokes parameter is now simply $\gamma = 3\left(\frac{L}{a}\right)^2 Re^{-1}$. If we follow Crisanti et al. (1990) and we confuse the derivative d/dt with the material derivative D/Dt, this equation in a non-rotating system simply reduces to the equation for Lagrangian particles with the addition of a damping perturbation term, depending on γ. A correct approach to the problem, however, cannot confuse these two derivatives, which are formally different.

If one performs a linear stability analysis of equation of motion (7.1) in the neighborhood of a Gaussian vortex centre, the result is that the centre is a neutrally stable point (the real parts of eigenvalues are zero). This means that tracers with finite size which have the same initial velocity as the fluid, are perfectly Lagrangian. Babiano et al. (2000), however, have shown in a simple cellular flow that, also for very small initial relative velocity with respect to the fluid, tracers trajectories diverge from fluid trajectories during a transient time whose duration is related to the value of the Stokes parameter. This difference is enhanced in the areas of the flow where the Okubo-Weiss function is strongly positive (hyperbolic points); areas where the Q-value is small or negative (elliptic points) are, on the contrary, attractors for particles with $\delta = 1$, whose trajectories can there converge to fluid trajectories.

Usually, tracers are seeded into a fluid with zero initial velocity, both in laboratory and in-situ experiments; it is very difficult to release tracers with the same velocity as the flow. Therefore, an initial transient, whose duration depends on the value of the Stokes parameter, is always present. During this transient, tracers can be attracted towards the centre of a vortex and be captured by the coherent structure, unlike Lagrangian particles.

This effect is clear in figure 7.1, which shows the trajectories (in the Cartesian plane) of a tracer seeded at rest in a Gaussian vortex in the position $(R, \Theta) = (1, 0)$, corresponding to the circulation cell (high positive Q-value). Different panels are for the case without Coriolis force or for a cyclonic and an anticyclonic vortex in a rotating reference frame. In figure 7.2, then, I plot the corresponding projections on the plane $(R, dR/dt)$ of the trajectories in phase space. In all the figures, it is evident that an attractor is present in the system, since all the trajectories in phase space converge in a point, which corresponds to a limit cycle in the Cartesian plane. The transient during which the tracer falls towards the attractor depends on the value of γ (see the different lengths of the spirals in phase space in figure 7.2a). Furthermore, the Coriolis term introduces a cyclone-anticyclone asymmetry also in the case of finite-size tracers, but only when rotation is strong ($Ro = 0.02$): in this case, the cyclone is attractive whereas the anticyclone is slightly repulsive (note also the waving trajectories in the Cartesian plane in figure 7.1b-c).

It is easy to explain this asymmetry. The radial component of the equation of

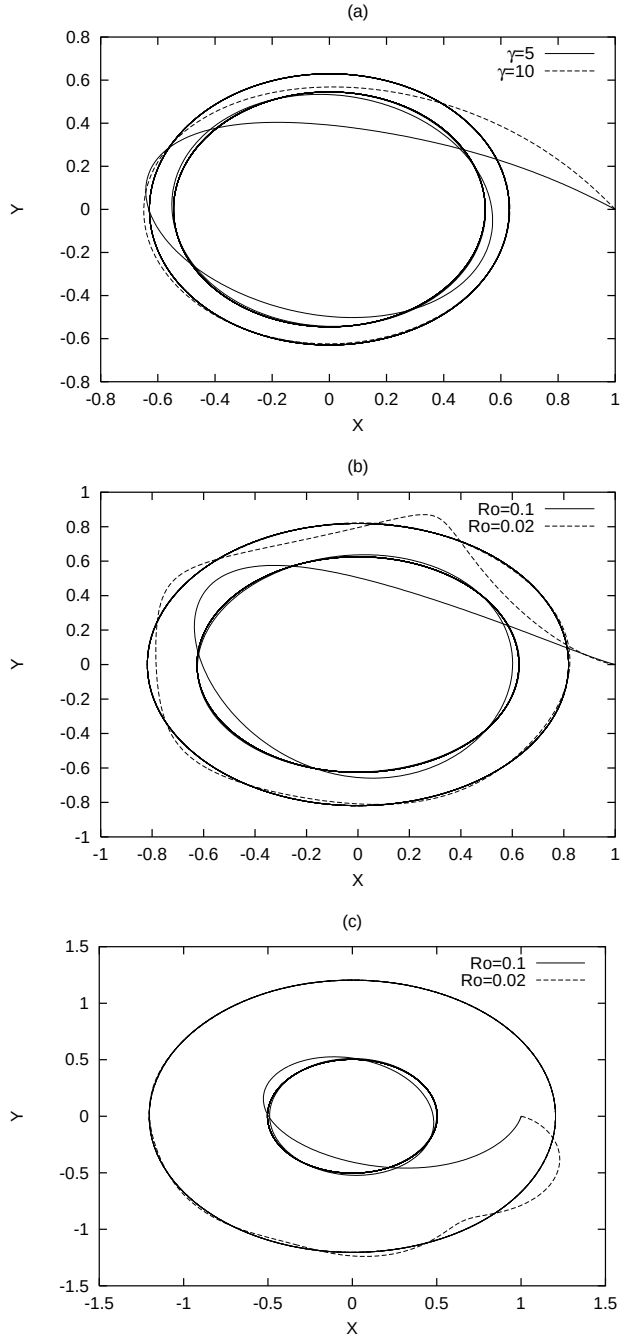

Figure 7.1: Trajectories in Cartesian plane for neutrally buoyant tracers in a non-rotating reference frame (panel a), in a cyclonic vortex (panel b) and in an anticyclonic vortex (panel c). Different lines are for different Stokes parameters in the non-rotating case, and for different Rossby number in the rotating case (where $\gamma = 5$). The initial position is in the circulation cell, at $R = 1$, and the initial velocity is zero.

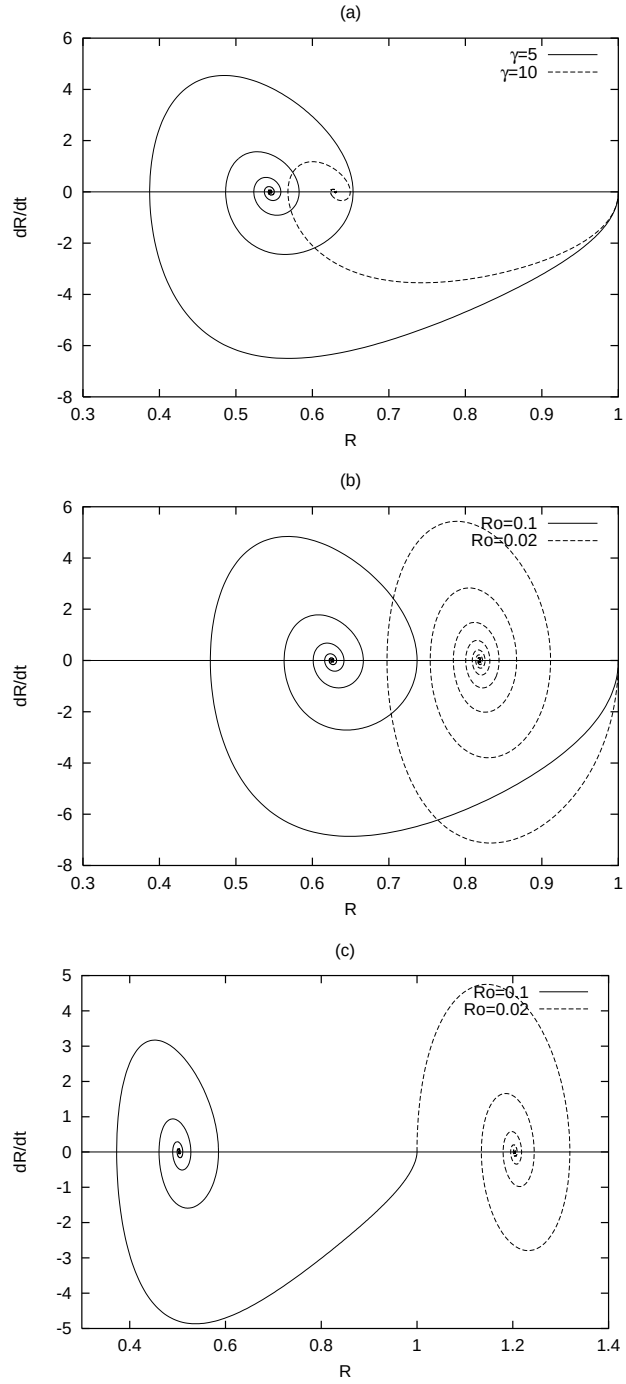

Figure 7.2: Same as in figure 7.1, but for trajectories in the plane $(R, dR/dt)$. Panel (a) is for the non-rotating case, panel (b) for a cyclone and panel (c) for an anticyclone.

motion (7.1) for a Gaussian vortex, simply reads:

$$\frac{d^2R}{dt^2} = \frac{1}{R}\left[\left(R\frac{d\Theta}{dt}\right)^2 - u_\theta^2\right] - \gamma\frac{dR}{dt} + \frac{2}{3}Ro^{-1}\left(R\frac{d\Theta}{dt} - u_\theta\right) + \frac{1}{3}\left(R\frac{d\Theta}{dt} - u_\theta\right)\zeta, \tag{7.2}$$

If the tracer is seeded at rest, the radial acceleration at initial time is given by:

$$\frac{d^2R}{dt^2}(t=0) = -\frac{u_\theta^2}{R} - \frac{2}{3}Ro^{-1}u_\theta - \frac{1}{3}u_\theta\zeta, \tag{7.3}$$

which is always centripetal for a cyclonic vortex, but may be centrifugal for an anticyclone ($u_\theta < 0$) if the Rossby number is enough small. The initial distance R_{stable} at which the contribution is neither centripetal nor centrifugal, for a given vortex and a given Rossby number, may be easily calculated from equation (7.3), by comparing to zero the r.h.s. and considering the expressions for the Gaussian vortex azimuthal velocity and vorticity. Without the lift term, it is possible to get out an analytical expression:

$$R_{stable} = \sqrt{-\ln\left(-\frac{Ro^{-1}}{3\psi_0}\right)}, \tag{7.4}$$

which is valid only for anticyclones when $Ro > 1/3|\psi_0|$. For a given Rossby number, initial positions at distances further than R_{stable} lead to expulsion, otherwise the tracer is captured. For $Ro \to 1/3|\psi_0|$, $R_{stable} \to 0$, then anticyclones eject tracers from any initial position.

7.3 Finite-size tracers in two-dimensional turbulence

Also for the case of finite-size, neutrally buoyant tracers, the results obtained by using an analytical vortex model lead to explanation of their dynamics in a complex flow such as the two-dimensional turbulent flow.

I have performed numerical simulations by using an uniform distribution of 4096 particles with $\delta = 1$ in the same way as described in the previous chapters. Tracers with initial velocity equal to the flow velocity do not display any remarkable difference with respect to Lagrangian particles, whereas differences are evident when tracers are seeded at rest. In this latter case, vortex cores attract tracers during a transient whose duration depend on the value of the Stokes parameter; tracers which start close to vortex cores (i.e., in the surrounding circulation cells), disregard the barrier constituted by the strong vorticity gradient at the edge of vortices and enter the cores, unlike Lagrangian particles. This happens both in a non-rotating system and in the case of cyclonic vortices in a rotating reference frame. For anticyclonic vortices, attraction or removal depends on the Rossby number: strong rotation ($Ro = 0.02$) favours the removal of tracers from circulation cells. All these results are perfectly in accordance with the ones found by using the Gaussian vortex model.

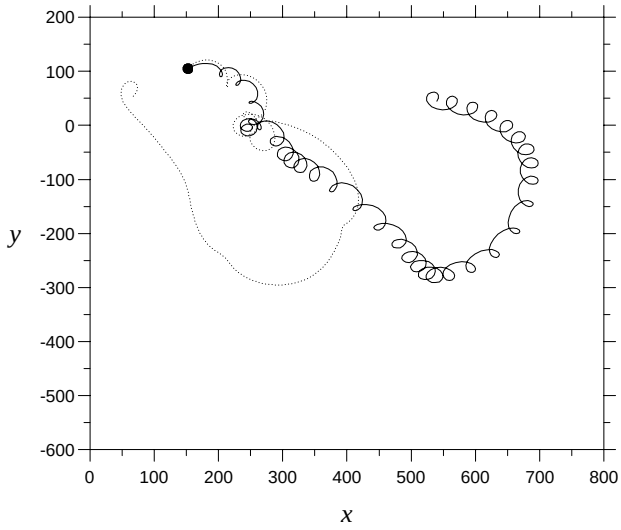

Figure 7.3: Trajectories of a finite-size tracer (solid line) and a Lagrangian particle (dotted line) starting at the same initial position in the circulation cell of an anticyclonic vortex, for the case without Coriolis force. In figure, units are grid points (in order to have radiants, one has to multiply by $2\pi/512$).

Figures 7.3 show the trajectories of a finite-size tracer (solid line) and a Lagrangian particle (dotted line) starting at the same initial position in the circulation cell of an anticyclonic vortex for the case without Coriolis force. The divergence of the two trajectories is evident: the Lagrangian particle spreads into the turbulent background, whereas the tracer is captured by the vortex.

After the transient during which tracers may enter vortex cores, the distribution of these tracers in the turbulent field is inhomogeneous and does not reflect the one of Lagrangian particles. Tracers accumulate in vortices, and this fact may be quantified by looking at the time series of the fractional density inside the vortex cores and the circulation cells (see figure 7.4 for the non-rotating case and figure 7.5 for the rotating one). The accumulation is concentrated at early times, then the density keeps roughly constant. The rotating case is particular significant, since it reflects the result found by using the analytical model of the Gaussian vortex. Cyclones are always attractive, whereas anticyclones are attractive when the Rossby number is large, repulsive when it is small.

These results confirm that an initial uniform distribution of neutrally buoyant tracers evolves towards a non-uniform asymptotic state in a time scale determined by the value of the Stokes parameter. After this asymptotic state has been reached, tracer dynamics is merely represented by the Lagrangian particles dynamics. If the transient may be considered short in comparison with the duration of an experiment employing neutrally buoyant tracers, nevertheless two important consequences are evident: the first is that data provided by tracers cannot be assimilated to Lagrangian data starting from their seeding, and the second is that after the tran-

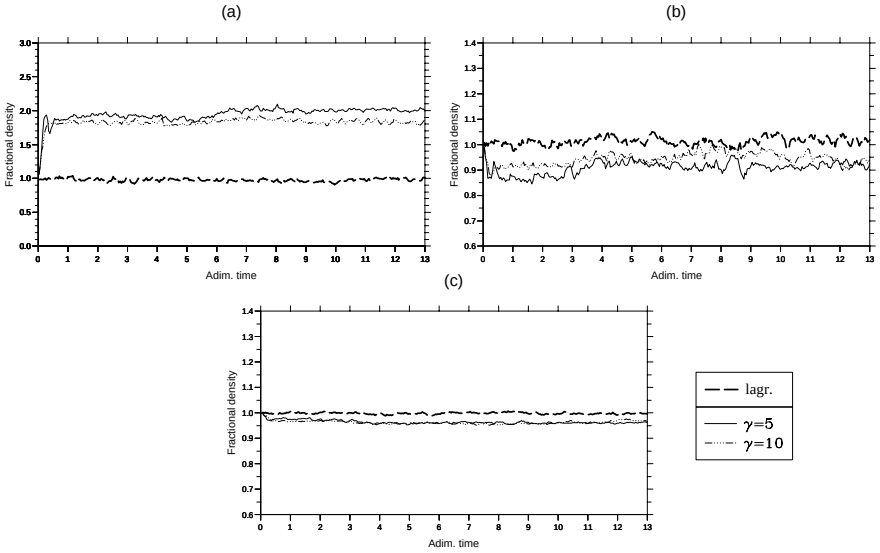

Figure 7.4: Time evolution of the fractional density of 4096 neutrally buoyant tracers ($\gamma = 5, 10$) and Lagrangian particles in areas occupied by: (a) vortex cores, (b) circulation cells, (c) turbulent background. The procedure used to distinguish the different topological areas is the same as the one used in the previous chapter.

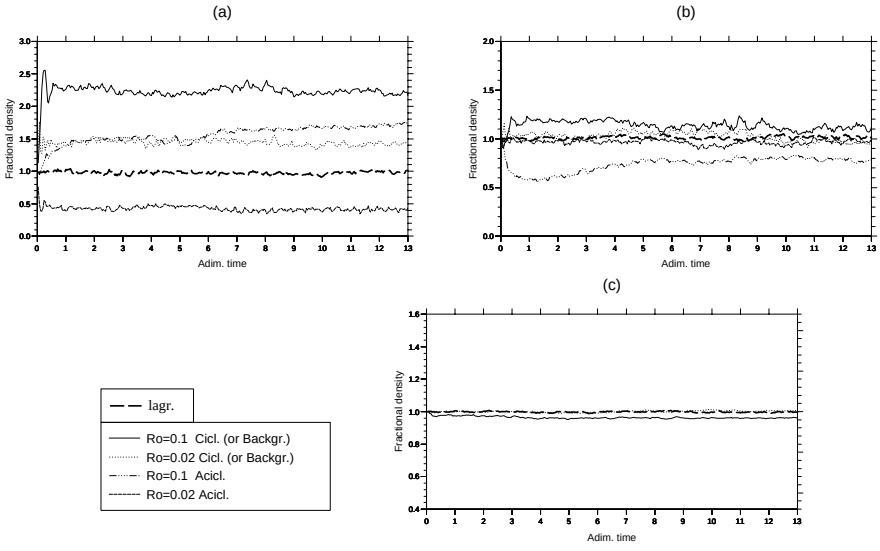

Figure 7.5: Same as in figure 7.4, but for the rotating case with different Rossby numbers. The Stokes parameter is here $\gamma = 5$

sient, the tracer distribution is inhomogeneous in the turbulent field. These two factors can introduce some biasses in the statistics of real tracers with respect to ideal fluid elements.

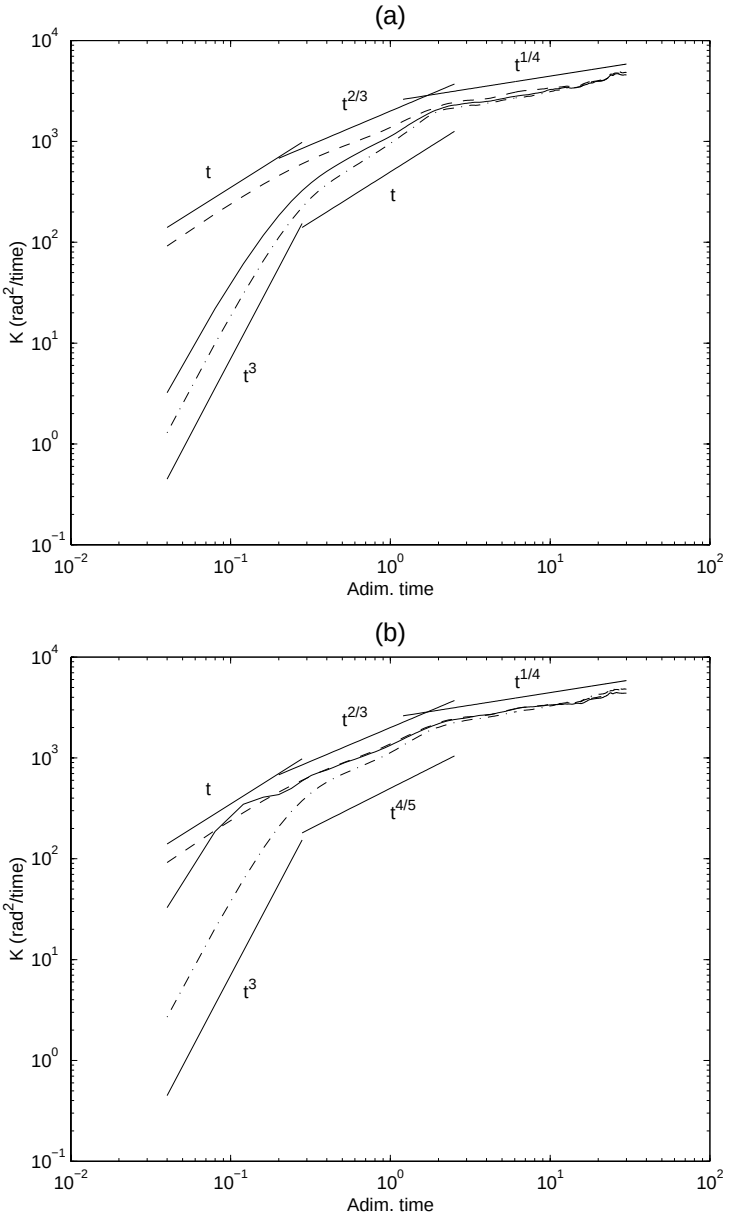

Figure 7.6: Time evolution of the dispersion coefficient $K(t) = A^2(t)/2t$, where $A^2(t)$ is the absolute dispersion as defined in the text, plotted for Lagrangian particles (dashed line) and neutrally buoyant tracers seeded at rest. Panel (a) represents the non-rotating case and solid and dash-dot line are, respectively, for tracers with $\gamma = 10$ and $\gamma = 1$; panel (b) is for the rotating case and solid and dash-dot lines are respectively for the case with $Ro = 0.02$ and $Ro = 0.1$. Straight lines are proportional to t^α, with different α.

An example of this fact is given in figure 7.6a-b (for the non-rotating and the rotating case, respectively), where I plot the dispersion coefficient $K(t) = A^2(t)/2t$, where $A^2(t)$ is the absolute dispersion, defined as:

$$A^2(t) = \frac{1}{N}\sum_{i=1}^{N} |\mathbf{x}_i(t) - \mathbf{x}_i(t_0)|^2 \,. \tag{7.5}$$

Lagrangian particles (dashed line in figure 7.6a-b) show a behaviour proportional to t at small time, and an anomalous diffusion with a behaviour proportional to $t^{2/3}$ and $t^{1/4}$ at intermediate time. On the contrary, tracers are initially accelerated from rest, therefore the dispersion coefficient is proportional to t^3. When Lagrangian particles show anomalous diffusion, neutrally buoyant tracers have a dispersion coefficient that is proportional to t, thus they do not show anomalous diffusion at the same time as for Lagrangian particles.

This is only one example of possible biasses in the statistics; other examples include spectra or velocity PDF, if the ensemble of tracers considered comes from areas in the flow where vortices are abundant, leading to inhomogeneous distribution of tracers at late times.

Conclusions

Turbulence in rapidly rotating flows is characterized by the spontaneous emergence of long-lived coherent vortices. Examples in geophysical flows are the tropical cyclones and the polar vortex in the atmosphere, meddies in the Atlantic ocean and rings in the Gulf stream, great spots in the atmospheres of outer planets (the Great Red Spot of Jupiter or the Great Dark Spot of Neptune).

In past years, this problem has been extensively explored by the use of numerical simulations. In particular, simulations have shown that the vortex cores are characterized by strong impermeability to inward and outward fluxes of passive tracers ("Lagrangian particles", whose dynamics is assimilated to the dynamics of fluid elements), and they are able to trap particles for long times.

In the first part of this thesis, I have discussed the results provided by some experiments on large-scale, quasi two-dimensional, homogeneous and rapidly rotating turbulent flows, performed in the rotating tank (diameter of 14 m) of the *Laboratoire des Ecoulements Géophysiques et Industriels* (LEGI) in Grenoble, France. With these experiments, we obtained a large, high quality data set on the dynamics of coherent vortices in a rapidly rotating barotropic fluid, which has been made possible by the use of a large-scale facility and the use of laser techniques for the flow visualization. The use of a mixed technique, experimental and numerical, has allowed to obtain Lagrangian data and trajectories of passive tracers, which are important to study the transport properties of tracers by coherent vortices.

The overall experimental results confirm many numerical results obtained by previous studies: trapping of tracers for long times in vortex cores, impermeability of vortices to inward fluxes, Lagrangian view of vortex merging etc. Differences have been found in the asymmetry cyclones-anticyclones, due to initial three-dimensional effects in laboratory experiments, and in the lack of strong strain areas around vortex cores.

A second part of my work has been devoted to the study of the dynamics of real particles in vortex-dominated barotropic turbulence. Lagrangian particles and fluid elements are considered as merely point-like and massless particles, but real particles have finite size and finite inertia ("impurities"). An early study of the impurity dynamics in a simple Gaussian vortex model has allowed to obtain analytical results which can explain most of the dynamical behaviours of such impurities in more complex flows, such as a barotropic turbulent flow.

In particular, the dynamics of impurities in rotating, vortex-dominated flows is

conditioned by the different influence of cyclonic and anticyclonic vortices: particles lighter or heavier than the fluid are captured or expelled by vortices according to the vortex sign, vorticity and to the Rossby number of the rotating system, disregarding the dynamical barriers at the edge of vortex cores, unlike Lagrangian particles.

The special case of passive neutrally buoyant tracers is also taken into account: floats and drifters in the oceans, balloons in the atmosphere and microscopic tracers used in laboratory experiments have the same density as the fluid but finite size. This differs their dynamics from the dynamics of Lagrangian particles and may introduce biasses in the statistics when the Lagrangian data provided by finite-size tracers are used and assimilated to data provided by fluid elements.

Acknowledgments

The list of people I have to thank for their direct or indirect help during my three years of Ph.D. could be as long as another Ph.D. thesis! Thus, I will only record here my gratitude to somebody, but all the others consider their support acknowledged!

First of all, I am grateful to my parents, to Alessandra and to my bosom friend Roberto for their unconditional support and encouragement.

Then, I wish to thank my advisors, Prof. Arnaldo Longhetto (*Università di Torino*) and Dr. Antonello Provenzale (*Istituto di Cosmogeofisica, CNR*), for their most valuable suggestions; thanks to them, I have learnt to be a researcher in Geophysical Fluid Dynamics, and to love this work.

I cannot finish without acknowledging help and support from all people at "Istituto di Cosmogeofisica" and at "Dipartimento di Fisica Generale, gruppo Geofit" of Turin University. In particular, I would like to mention Jost Graf von Hardenberg, Claudia Pasquero, Annalisa Bracco, Chiara Toniolo, Sara Riccardo, Cristiano Nicolello, Dr. Claudio Giraud and Dr. Guido Boffetta at ICG-CNR, and Davide Bertoni, Renato Forza, Silvia Ferrarese, Minwei Qian, Massimiliano Manfrin, Nicola Loglisci and Prof. Claudio Cassardo at DFG-Geofit; with them, I have shared work and, above all, friendship.

I am grateful to the Director of "Istituto di Cosmogeofisica, CNR", Prof. Pio Picchi, and to the Director of "Dipartimento di Fisica Generale dell'Università di Torino", Prof. Guido Piragino, for their kind hospitality. Furthermore, I am indebted to the Director of Equipe "Coriolis" of LEGI in Grenoble (France), Prof. Joël Sommeria, and to the whole laboratory staff (Henry Didelle, Jan-Bert Flor, Olivier Praud, Gauthier Delerce, Sylvain Sadoux and Emmanuelle Thivot-Cazat, in particular), for their precious help and support during my stay at their laboratory, and also afterwards during the analysis of PIV images.

Lastly, a special memory is devoted to my grandparents.

Bibliography

[1] L. Aanen, A. Telesca, and J. Westerweel. Measurement of turbulent mixing using PIV and LIF. *Machine vision and graphics*, 2000. Accepted paper.

[2] J. Adem. A series solution for the barotropic vorticity equation and its application in the study of atmospheric vortices. *Tellus*, 8:364, 1956.

[3] M. Arai and T. Yamagata. Asymmetric evolution of eddies in rotating shallow-water. *Chaos*, 4 (2):177, 1994.

[4] H. Aref. Stirring by chaotic advection. *J. Fluids Mech.*, 143:1, 1984.

[5] H. Aref and S. Balanchadar. Chaotic advection in a stokes flow. *Phys. Fluids*, 29:3515, 1986.

[6] L. Armi, D. Hebert, H. Oakey, J.F. Price, P.L. Richardson, and H.T. Rossby. Two years in the life of a mediterranean salt lens. *J. Phys. Oceanogr.*, 19:354, 1989.

[7] T.R. Auton. The lift force on a spherical body in a rotational flow. *J. Fluids Mech.*, 183:199, 1987.

[8] T.R. Auton, J.C.R. Hunt, and M. Prud'homme. The force exerted on a body in inviscid unsteady non uniform rotational flow. *J. Fluid Mech.*, 197:241, 1988.

[9] A. Babiano, C. Basdevant, B. Legras, and R. Sadourny. Vorticity and passive-scalar dynamics in two-dimensional turbulence. *J. Fluid Mech.*, 183:379, 1987a.

[10] A. Babiano, C. Basdevant, P. LeRoy, and R. Sadourny. Single-particle dispersion, lagrangian structure function and lagrangian energy spectrum in two-dimensional incompressible turbulence. *J. Mar. Res.*, 45:107, 1987b.

[11] A. Babiano, C. Basdevant, P. LeRoy, and R. Sadourny. Relative dispersion in two-dimensional turbulence. *J. Fluid Mech.*, 214:535, 1990.

[12] A. Babiano, G. Boffetta, A. Provenzale, and A. Vulpiani. Chaotic advection in point vortex models and two-dimensional turbulence. *Phys. Fluids*, 6 (7):2465, 1994.

[13] A. Babiano, J.H.E. Cartwright, O. Piro, and A. Provenzale. Dynamics of a small neutrally bouyant sphere in a fluid and targeting in Hamiltonian systems. *Phys. Rev. Lett.*, 84 (25):5764, 2000.

[14] A. Babiano, B. Dubrulle, and P. Frick. Scaling properties of two-dimensional turbulence. *Phys. Rev E*, 52:3719, 1995.

[15] C. Basdevant and T. Philipovitch. On the validity of the Weiss criterion in two-dimensional turbulence. *Physica D*, 73:17, 1994.

[16] A.B. Basset. *Treatise on hydrodynamics*. Deighton Bell, London, 1888a.

[17] A.B. Basset. On the motion of a sphere in a viscous liquid. *Phil. Trans. R. Soc. London*, 179:43, 1888b.

[18] G.K. Batchelor. Computation of the energy spectrum in homogeneous two-dimensional turbulence. *Phys. Fluids Suppl. II*, 12:233, 1969.

[19] V.V. Beloshapkin, A.A. Cernikov, M.Ya. Natenzon, B.A. Petrovichev, R.Z. Sagdeev, and G.M. Zalavsky. Chaotic streamlines in pre-turbulent states. *Nature*, 337:133, 1989.

[20] R. Benzi, S. Patarnello, and P. Santangelo. On the statistical properties of two-dimensional decaying turbulence. *Europhys. Lett.*, 3:811, 1987.

[21] G. Boffetta, G. Lacorata, G. Redaelli, and A. Vulpiani. Detecting barriers to transport: a review of different techniques. Preprint, 2001.

[22] Boussinesq. *Application à l'étude des potentiels*. Blanchard, 1969 reedition, 1885a.

[23] Boussinesq. Sur la résistance qu'oppose un liquid indéfini en repos. *Comptes Rendus, Acad. Sci. Paris*, 100:935, 1885b.

[24] A. Bracco, P.H. Chavanis, A. Provenzale, and E.A. Spiegel. particel aggregation in a turbulent Keplerian flow. *Phys. Fluids*, 11 (8):2280, 1999.

[25] A. Bracco, J.C. McWilliams, G. Murante, A. Provenzale, and J.B. Weiss. Revisiting freely decaying two-dimensional turbulence at millenium resolution. *Phys. Fluids*, 12 (11):2931, 2000.

[26] M.E. Brachet, M. Meneguzzi, H. Politano, and P.L. Sulem. The dynamics of freely decaying two-dimensional turbulence. *J. Fluid Mech.*, 194:333, 1988.

[27] M.E. Brachet, M Meneguzzi, and P.L. Sulem. Small-scale dynamics of high-Reynolds-number two-dimensional turbulence. *Phys. Rev. Lett.*, 57 (6):683, 1986.

[28] O. Cardoso, D. Marteau, and P. Tabeling. Quantitative experimental study of the free decay of quasi-two-dimensional turbulence. *Phys. Rev. E*, 49 (1):454, 1994.

[29] G.F. Carnevale, J.C. McWilliams, Y. Pomeau, J.B. Weiss, and W.R. Young. Evolution of vortex statistics in two-dimensional turbulence. *Phys. Rev. Lett.*, 66 (21):2735, 1991.

[30] G.F. Carnevale, J.C. McWilliams, Y. Pomeau, J.B. Weiss, and W.R. Young. Rates, pathways, and end states of nonlinear evolution in decaying two-dimensional turbulence: scaling theory versus selective decay. *Phys. Fluids A*, 4 (6):1314, 1992.

[31] X. Carton, C.R. Flier, and L. Polvani. The generation of tripoles from unstable axisymmetric isolated vortex structure. *Europhys. Lett.*, 9:339, 1989.

[32] J.C.L. Chan and R.T. Williams. Analytical and numerical studies of the beta-effect in tropical cyclone motion. Part I: zero mean flow. *J. Atmos. Sci.*, 44:1257, 1987.

[33] P.H. Chavanis. Trapping of dust by coherent vortices in the solar nebula. Preprint, 2000.

[34] Y. Couder. Two-dimensional grid turbulence in a thin liquid film. *J. Physique Lett.*, 45 (8):353, 1984.

[35] A. Crisanti, M. Falcioni, A. Provenzale, P. Tanga, and A. Vulpiani. Dynamics of passively advected impurities in simple two-dimensional models. *Phys. Fluids A*, 4 (8):1805, 1992.

[36] A. Crisanti, M. Falcioni, A. Provenzale, and A. Vulpiani. Passive advection of particles denser than the surrounding fluid. *Phys. Lett. A*, 150 (2):79, 1990.

[37] G. Chabert d'Hieres, P.A. Davies, and H. Didelle. Laboratory studies of pseudo-periodic forcing due to vortex shedding from an isolated solid obstacle in a homogeneous rotating fluid. In J.C.J. Nihoul and B.M. Jamart, editors, *Mesoscale/Synoptic coherent structures in geophysical turbulence*. Elsevier Science Publishers B.V., Amsterdam (The Netherlands), 1989.

[38] T.E. Dowling. Dynamics of Jovian atmospheres. *Annu. Rev. Fluid Mech.*, 27:293, 1995.

[39] D.G. Dritschel. Vortex properties of two-dimensional turbulence. *Phys. Fluids A*, 5 (4):984, 1993.

[40] O.A. Druzhinin and L.A. Ostrovsky. The influence of Basset force on particle dynamics in two-dimensional flows. *Physica D*, 76:34, 1994.

[41] D. Elhmaidi, A. Provenzale, and A. Babiano. Elementary topology of two-dimensional turbulence from a lagrangian viewpoint and single-particle dispersion. *J. Fluid Mech.*, 257:533, 1993.

[42] M. Falcioni, G. Paladin, and A. Vulpiani. Regular and chaotic motion of particles in a two-dimensional flow. *J. Phys. A: Math. Gen.*, 21:3451, 1988.

[43] M. Farge and R. Sadourny. Wave-vortex dynamics in rotating shallow-water. *J. Fluids Mech.*, 206:433, 1990.

[44] A.M. Fincham and G. Delerce. Advanced optimization of Correlation Imaging Velocimetry algorithms. *Exp. in Fluids*, 2000. Accepted paper.

[45] A.M. Fincham and G.R. Spedding. Low-cost, high-resolution DPIV for measurement in turbulent fluid flows. *Exp. in Fluids*, 23:449, 1997.

[46] A.M. Fincham, G.R. Spedding, and R.F. Blackwelder. Current contraints of digital particle tracking techniques in fluid flows. *Bull. Am. Phys. Soc.*, 36 (10):2692, 1991.

[47] G.R. Flier. Isolated eddy models in geophysics. *Annu. rev. Fluid Mech.*, 19:493, 1987.

[48] U. Frisch. *Turbulence. The legacy of A.N. Kolmogorov*. Cambridge University Press, 1995.

[49] U. Frisch and P.L. Sulem. Numerical simulation of the inverse cascade in two-dimensional turbulence. *Phys. Fluids*, 27 (8):1921, 1984.

[50] G.J. Goni, A.L. Garzoli, A.J. Roubicek, D.B. Olson, and O.B. Brown. Agulhas ring dynamics from TOPEX/POSEIDON satellite altimeter data. *J. Marine Res.*, 55:861, 1997.

[51] The Ring Group. Gulf Stream cold-core rings: their physics, chemistry and biology. *Science*, 212:1091, 1981.

[52] A.E. Haensen, D. Marteau, and P. Tabeling. Two-dimensional turbulence and dispersion in a freely decaying system. *Phys. Rev. E*, 58 (6):7261, 1998.

[53] D.P. Hart. The elimination of correlation errors in PIV processing. In 9^{th} *international symposium on application of laser techniques to fluid mechanics*, Lisbon, Portugal, July 13-16 1998.

[54] J.R. Holton. *An introduction to dynamic metereology*. Academic Press, 1979.

[55] E.J. Hopfinger and G.J.F. van Heijst. Vortices in rotating fluids. *Ann. Rev. Fluid Mech.*, 25:241, 1993.

[56] B.L. Hua and P. Klein. An exact criterion for the stirring property of nearly two-dimensional turbulence. *Physica D*, 1998.

[57] A.P. Ingersoll. Atmospheric dynamics of the outer planets. *Science*, 248:308, 1990.

[58] K. Jambunathan, X.Y. Yu, B.N. Dobbins, and S. Ashfort-Frost. An improuved cross-correlation technique for particle image velocimetry. *Meas. Sci. Technol.*, 6:507, 1997.

[59] A.N. Kolmogorov. Dissipation of energy in the locally isotropic turbulence. In *Turbulence and stochastic processes: Kolmogorov's ideas 50 years on*, volume 434, p. 15 of *Proc. R. Soc. Lond. A*. J. Hunt and O. Philips and D. Williams eds, 1991. Originally published in Russian in Dokl. Akad. Nauk. SSSR, vol. 32 (1), 1941b.

[60] A.N. Kolmogorov. The local structure of turbulence in incompressible viscous fluid for very large Reynolds number. In *Turbulence and stochastic processes: Kolmogorov's ideas 50 years on*, volume 434, p. 9 of *Proc. R. Soc. Lond. A*. J. Hunt, O. Philips, D. Williams eds, 1991. Originally published in Russian in Dokl. Akad. Nauk. SSSR, vol. 30 (4), 1941a.

[61] R.H. Kraichnan. Inertial ranges in two-dimensional turbulence. *Phys. Fluids*, 10:1417, 1967.

[62] R.H. Kraichnan. Inertial range transfer in two- and three-dimensional turbulence. *J. Fluid Mech.*, 47:525, 1971.

[63] N. Kukharin, S.A. Orszag, and V. Yakhot. Quasicrystallization of vortices in driftwave turbulence. *Phys. Rev. Lett.*, 75:2486, 1995.

[64] P. K. Kundu. *Fluid Mechanics*. Academic Press, San Diego, 1990.

[65] V.D. Larichev and J.C. McWilliams. Weakly decaying turbulence in an equivalent-barotropic fluid. *Phys. Fluids A*, 3:938, 1991.

[66] B. Legras, P. Santangelo, and R. Benzi. High-resolution numerical experiments for forced two-dimensional turbulence. *Europhys. Lett.*, 5:37, 1988.

[67] M. Lesieur. *Turbulence in Fluids*. Kluwer, Dordrecht, 1993.

[68] G. Magnus. A note on the rotary motion of the liquid jet. *Annalen der Physik und Chemie*, 63:363, 1861.

[69] M.E. Maltrud and G.K. Vallis. Energy spectra and coherent structures in forced two-dimensional and beta-plane turbulence. *J. Fluid Mech.*, 228:321, 1991.

[70] M.E. Maltrud and G.K. Vallis. Energy and enstrophy transfer in numerical simulations of two-dimensional turbulence. *Phys. Fluids A*, 5:1760, 1993.

[71] W.H. Matthaeus, W.T. Stribling, D. Martinez, S. Oughton, and D. Montgomery. Decaying, two-dimensional, Navier-stokes turbulence at very long times. *Physica D*, 51:531, 1991.

[72] M.R. Maxey and J.J. Riley. Equation of motion for a small rigid sphere in nonuniform flow. *Phys. Fluids*, 23:883, 1983.

[73] M.E. McIntyre. On the Antartic ozone zone. *J. Atmos. Terr. Phys.*, 51:29, 1989.

[74] M.E. McIntyre. The stratospheric polar vortex and sub-vortex: fluid dynamics and midlatitude ozone loss. *Philos. Trans. R. Soc. London Ser. A*, 352:227, 1995.

[75] J.C. McWilliams. The emergence of isolated coherent vortices in turbulent flow. *J. Fluid Mech*, 146:21, 1984.

[76] J.C. McWilliams. Submesoscale, coherent vortices in the ocean. *Rev. Geophys.*, 23:165, 1985.

[77] J.C. McWilliams. The vortices of two-dimensional turbulence. *J. Fluid Mech.*, 219:361, 1990.

[78] M.V. Melander, N.J.Zabusky, and J.C. McWilliams. Symmetric vortex merger in two dimensions. *J. Fluid Mech.*, 195:303, 1988.

[79] E. E. Michaelides. Review - The transient equation of motion for particles, bubbles, and droplets. *J. Fluids Eng.*, 119:233, 1997.

[80] P. Muller. Ertel's potential vorticity theorem in physical oceanography. *Rev. Geophys.*, 33:67, 1995.

[81] K. Ohkitani. Wavenumber space dynamics of enstrophy cascade in a forced two-dimensional turbulence. *Phys. Fluids A*, 3:1598, 1991.

[82] A. Okubo. Horizontal dispersion of floatable particles in the vicinity of velocity singularities such as convergence. *Deep-Sea Res.*, 17:445, 1970.

[83] F. Paparella, A. Babiano, C. Basdevant, A. Provenzale, and P. Tanga. A Lagrangian study of the antartic polar vortex. *J. Geophysical Research*, 102 (D6):6765, 1997.

[84] P. Paradisi and F. Tampieri. Stability analysis of solid particle motion in rotational flows. *Il nuovo cimento C*, 24 (3):407, 2001.

[85] J. Paret, M.C. Jullien, and P. Tabeling. Vorticity statistics in the two-dimensional enstrophy cascade. *Phys. rev. Lett.*, 83 (17):3418, 1999.

[86] J. Paret and P. Tabeling. Experimental observation of the two-dimensional inverse energy cascade. *Phys. Rev. Lett.*, 79 (21):4162, 1997.

[87] J. Paret and P. Tabeling. Intermittency in the two-dimensional inverse cascade of energy: experimental observations. *Phys. Fluids*, 10 (12):3126, 1998.

[88] J. Pedlosky. *Geophysical Fluid Dynamics*. Springer-Verlag, New York, second edition, 1987.

[89] L.M. Polvani, J.C. McWilliams, M.A. Spall, and R. Ford. The coherent structures of shallow-water turbulence: deformation-radius effects, cyclone-anticyclone asymmetry and gravity-wave generation. *Chaos*, 4 (2):177, 1994.

[90] L.M. Polvani, N.J. Zabusky, and G.R. Flier. Two-layer geostrophic vortex dynamics. Part 1: upper-layer V-states and merger. *J. Fluid Mech.*, 205:215, 1989.

[91] A. Provenzale. Transport by coherent vortices. *Annu. Rev. Fluid Mech.*, 31:55, 1999.

[92] A. Provenzale, A. Babiano, and B. Villone. Single-particle trajectories in two-dimensional turbulence. *Chaos, Solitons and Fractals*, 5, 10:2055, 1995.

[93] A. Provenzale, A. Babiano, and A. Zanella. Dynamics of Lagrangian tracers in barotropic turbulence. In E. Villermaux H. Chate, J.M. Chomaz, editor, *Mixing: Chaos and Turbulence*. Plenum, New York, 1998.

[94] M. Raffel, C.E. Willert, and J. Kompenhans. *Particle image velocimetry, a practical guide*. Springer-Verlag, Berlin Heidelberg, 1998.

[95] P.L. Richardson, M.S. McCartney, and C. Maillard. A search for meddies in historical data. *Dyn. Atmos. Oceans*, 15:241, 1991.

[96] P.L. Richardson, D. Walsh, L. Armi, M. Schroder, and J.F. Price. Tracking three meddies with SOFAR floats. *J. Phys. Oceanogr.*, 19:371, 1989.

[97] P. Ripa. On the stability of elliptical vortex solutions of the shallow-water equations. *J. Fluids Mech.*, 183:343, 1987.

[98] C.G. Rossby. On a mechanism for the release of potential energy in the atmosphere. *J. Met.*, 6:163, 1949.

[99] M.A. Rutgers. Forced 2D turbulence: experimental evidence of simultaneous inverse energy and forward enstrophy cascades. *Phys. Rev. Lett.*, 81:2244, 1998.

[100] P.G. Saffman. The lift on a small sphere in a slow shear flow. *J. Fluids Mech.*, 22:385, 1965.

[101] P. Santangelo, R. Benzi, and B. Legras. The generation of vortices in high-resolution, two-dimensional decaying turbulence and the influence of initial conditions on the breaking of the self-similarity. *Phys. Fluids A*, 1 (6):1027, 1989.

[102] F. Scarano and M.L. Riethmuller. Perfectionnement dans les techniques de traitement des données en vélocimétrie par images de particules. In *Actes* $6^{ème}$ *Congrès Francophone de Vélocimetrie Laser*, Saint-Louis, France, 1998.

[103] F. Scarano and M.L. Riethmuller. Iterative multigrid approach in PIV image processing. *Exp. in Fluids*, 26:513, 1999a.

[104] F. Scarano and M.L. Riethmuller. Advances in iterative multigrid PIV image processing. In 3^{rd} *International Workshop on Particle Image Velocimetry*, Santa Barbara, USA, September 16–18 1999b.

[105] B.A. Smith et al. The Jupiter system through the eyes of Voyager-1. *Science*, 204:951, 1979.

[106] A. Stegner and D.G. Dritschel. A numerical investigation of the stability of isolated shallow-water vortices. *J. Phys. Oceanogr.*, to appear.

[107] G.G. Stokes. On the theories of internal friction of the fluids in motion. *Trans. Cambrdige Phil. Soc.*, 8:287, 1845.

[108] P. Tabeling, S. Burkhart, O. Cardoso, and H. Willaime. Experimental study of freely decaying two-dimensional turbulence. *Phys. Rev. Lett.*, 67 (27):3772, 1991.

[109] P. Tanga, A. Babiano, B. Dubrulle, and A. Provenzale. Forming planetesimals in vortices. *Icarus*, 121:158, 1996.

[110] P. Tanga and A. Provenzale. Dynamics of advected tracers with varying buoyancy. *Physica D*, 76:202, 1994.

[111] G. I. Taylor. Experiments on the motion of solid bodies in rotating fluids. *Proc. Roy. Soc. A*, 104:213, 1923.

[112] P.J. Thomas. On the influence of the Basset history force on the motion of a particle through a fluid. *Phys. Fluids A*, 4 (9):2090, 1992.

[113] J.A. van de Konijnenberg. *Spin-up in non-axisymmetric containers*. PhD thesis, Eindhoven University of Technology, 1995.

[114] G.J.F. van Heijst. Spin-up phenomena in non axisymmetric containers. *J. Fluid Mech.*, 206:171, 1989.

[115] G.J.F. van Heijst, P.A. Davies, and R.G. Davis. Spin-up in a rectangular container. *Phys. Fluids A*, 2 (2):150, 1990.

[116] D.A. Walker. A fluorescence technique for measurement of concentration in mixing liquids. *J. Phys. E: Sci. Instrum.*, 20:217, 1987.

[117] D.W. Waugh. The efficiency of symmetric vortex merger. *Phys. Fluids A*, 4:1745, 1992.

[118] J.B. Weiss. The dynamics of enstrophy transfer in two-dimensional hydrodynamics. Technical report (LJ1-TN-81-121), La Jolla Inst., San Diego, 1981.

[119] J.B. Weiss and J.C. McWilliams. Temporal scaling behavior of decaying two-dimensional turbulence. *Phys. Fluids A*, 5 (3):608, 1993.

[120] J. Westeerwel. Efficient detection of spurious vectors in Particle Image Velocimetry data. *Exp. in Fluids*, 16:236, 1994.

[121] J. Westeerwel, D. Dabiri, and M. Gharib. The effect of a discrete window offset on the accuracy of cross-correlation analysis of digital PIV recordings. *Exp. in Fluids*, 10:181, 1997.